# THERMAL TRANSPORT PHENOMENA AT CONTACTS AND KINKS OF NANOWIRES

By

Yang Zhao

Dissertation

Submitted to the Faculty of the

Graduate School of Vanderbilt University

in partial fulfillment of the requirements

for the degree of

DOCTOR OF PHILOSOPHY

in

Mechanical Engineering

January 31, 2021

Nashville, Tennessee

Approved:

Deyu Li, Ph.D.

D. Greg Walker, Ph.D.

Joshua Caldwell, Ph, D.

Leon Bellan, Ph.D.

Yaqiong Xu, Ph.D.

Copyright © 2021 by Yang Zhao
All Rights Reserved

*To my beloved mom and dad*

## ACKNOWLEDGEMENTS

My Ph.D. journey has been a life-changing and invaluable experience, and it would not have been possible without the support and encouragement that I received from my advisor, my Ph.D. dissertation committee, collaborators, group members, friends, and my family.

First and foremost, I would like to thank my advisor, Dr. Deyu Li, whose expertise, critical thinking, and insightful advice not only guided me throughout my entire doctorate study but also will benefit my future career. He has inspired me to become an independent researcher and helped me realize the power of critical reasoning. Dr. Li is also kind and warm in both my work and life; he and his wife always invite us to their house and provide delicious BBQ on holidays. His kindness and continuous encouragement make this dissertation possible. I also want to express my sincere gratitude to my Ph.D. dissertation committee: Dr. D. Greg Walker, Dr. Joshua Caldwell, Dr. Leon Bellan, and Dr. Yaqiong Xu for their patience, encouragement, and perceptive suggestions on my research and career path.

Next, I want to express my appreciation for the help and support from my collaborators, who are excellent researchers at the Chinese University of Hong Kong, Southeast University in China, and the University of North Carolina at Charlotte. I also want to thank the cleanroom staff at Vanderbilt Institute of Nanoscale Science and Engineering and Cornell Nanoscale Science and Technology Facility. They were extremely helpful with my research. I enjoy working with them and learned a lot from them.

I am grateful to all group members in the Micro/Nanoscale Thermal Fluids Lab and I am lucky to meet them during my Ph.D. Their encouragement and support make my path toward Ph.D. fruitful and enjoyable. We have established a deep friendship together and will support each other in the future. My thanks also go to my lovely friends who unconditionally encourage me to

overcome challenges and keep my company in difficult times. They make me believe in myself and support me to be better and stronger.

Last but not least, I want to express my special thanks and love to my family. My mom and dad build the safest and warmest home for me and they are always there to believe in me. They provide me with infinite support and encourage me to pursue my dreams and career. They are my role model to pursue a simple lifestyle with contentment. I love you, mom and dad!

TABLE OF CONTENTS

Page

## LIST OF FIGURES

Figure Page

# Chapter 1

## Introduction

Nanoscale transport phenomena have attracted significant attention in the past two decades and remarkable progress has been made in terms of understanding electron and phonon transport properties in various nanowires (Li et al. 2003; Yang, Tao, et al. 2019; Zhang et al. 2018), nanotubes (Wingert et al. 2015; Yang et al. 2014), and nanoribbons (Guan et al. 2012; Yang et al. 2012, 2017). In comparison, relatively less efforts have been devoted to junctions of nanostructures, because of the tremendous challenges involved in experiments. However, transmission of charge and energy carriers through contacts and junctions could be critical for various applications. First, in nanocomposites with percolated nanofillers, the contact electrical and thermal resistance could dominate the overall transport properties of the nanocomposites (Fuhrer et al. 2000; Yanagi et al. 2010; Yang et al. 2010). As a result, even though highly conductive nanofillers are used, the enhancement in transport properties could still be very limited. Second, thermoelectrics, an all-solid-state energy conversion mechanism that can directly convert heat to electricity, requires materials with high electrical conductivity and low thermal conductivity to achieve a desirable thermoelectric figure of merit ($ZT$), which is expressed as $ZT = S^2\sigma T/\kappa$. Here $S$, $\sigma$ and $\kappa$ are the Seebeck coefficient, the electrical conductivity and the thermal conductivity, respectively. Nanostructuring offers new opportunities of enhancing $ZT$ through tuning the electrical and thermal properties separately and it has been shown that nanoscale junctions can provide unique opportunities to enhance $ZT$ (Hewitt et al. 2012; Yao et al. 2010; Zhang et al. 2017). In addition, nanoscale junctions are also abundant in nanoelectronic devices and understanding electrical and thermal transmission at these contacts are of great interest for proper device operation and thermal management.

This dissertation pursues new understandings of thermal transport through nanoscale junctions including contacts between individual nanowires and kinks inside individual nanowires. The introduction will review the relevant research efforts and state-of-the-art understandings on transport through nanoscale junctions, which will lay a foundation for the performed research in this dissertation.

### 1.1 Phonon Transport in Individual Nanostructures

Thermal transport in dielectric materials and non-degenerated semiconductors is dominated by phonons or lattice vibrations. Phonons can be treated as both waves and particles. Based on the kinetic theory of particle transport, the lattice thermal conductivity $\kappa_l$ can be expressed as

$$\kappa_l = \frac{1}{3} C v l, \tag{1.1}$$

where *C*, *v*, and *l* are the heat capacity, speed of sound, and phonon mean free path (MFP), respectively. When the phonon MFP is larger than at least one characteristic size of nanostructures, the classical size effect becomes important and based on the Matthiessen's rule, the effective phonon MFP in nanostructures can be obtained through combining independent scattering processes as

$$l^{-1} = l_b^{-1} + l_i^{-1}. \tag{1.2}$$

Here, the subscript *b* denotes boundary scattering and *i* represents all intrinsic scattering processes in bulk materials including Umklapp scattering, defects scattering, and electron-phonon (e-ph) scattering. As the characteristic size of nanostructures (i.e., Casimir length) is smaller than the intrinsic phonon MFP, boundary scattering could significantly alter the effective phonon MFP, which is called the classical size effect.

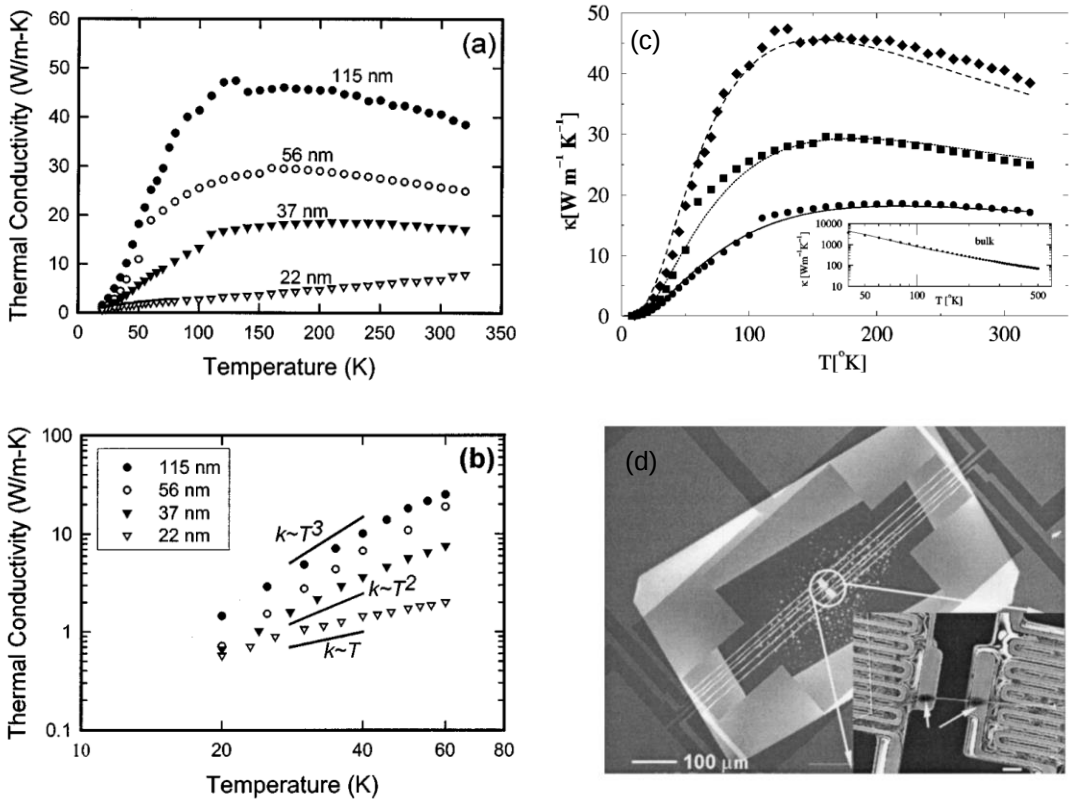


**Figure 1.1** (a) Measured thermal conductivity of silicon nanowires (Li et al. 2003). The number besides each curve denotes the corresponding wire diameter. (b) Low temperature experimental data on a logarithmic scale. Also shown are $T^3$, $T^2$, and $T^1$ curves for comparison (Li et al. 2003). (c) Thermal conductivities vs temperature calculated using transmission functions calculated based on complete phonon dispersions, for silicon nanowires with the diameters of 37 nm (solid), 56 nm (dotted) and 115 nm (dashed) (Mingo 2003). (d) SEM image of a suspended microdevice. The lower inset shows a 100 nm silicon nanowire bridging the two heater pads, with wire-pad junctions wrapped with amorphous carbon deposits (shown by arrows) (Li et al. 2003). The scale bar in the inset represents 2 μm.

The classical size effect on thermal transport in silicon nanowires was first predicted by Volz and Chen using molecular dynamics (MD) and the modeled thermal conductivity reduction was fitted well with the Boltzmann equation taking boundary scattering into account (Volz and Chen 1999). The first experimental measurement on individual silicon nanowires with diameters of 22, 37, 56 and 115 nm was conducted by Li et al. with a suspended micro-thermal bridge device (Li et al. 2003). The measured thermal conductivities of silicon nanowires in **Figure 1.1(a)** are up to

two orders of magnitude lower than the bulk value and present a strong size dependence, which suggests that phonon boundary scattering could play a significant role for thermal transport in silicon nanowires. As shown in **Figure 1.1(c)**, except for the 22 nm wire, the thermal conductivities of the other three wires can be fitted very well with reduced phonon MFP under the influence of boundary scattering (Mingo 2003). Compared to the peak temperature of 25 K for bulk silicon, the peak of thermal conductivity in nanowires shifts to higher temperatures, which suggests that phonon boundary scattering dominated over the Umklapp scattering at low temperatures. In addition, the temperature dependence at low temperatures on a log-log scale in **Figure 1.1(b)** shows that the nanowires exhibit a transition from the Debye $T^3$ law to an approximately linear temperature dependence as the diameter decreases, which has been reconfirmed with silicon nanowires with diameters below 30 nm (Chen et al. 2008) and Ge nanowires with diameters of 15 nm (Wingert et al. 2011). In view that boundary scattering is independent of temperature and phonon frequency, the deviation of temperature dependence from the Debye $T^3$ law indicates that other size-induced effects occur in the smallest nanowire.

The theoretical analysis on phonon transport in thin Ge nanowires proposes that the group velocity could be drastically reduced compared to the bulk value due to phonon confinement (Wingert et al. 2011). The angle-resolved Brillouin light scattering measurements on thin silicon films observed a significant reduction in velocities of the fundamental flexural mode in proportion to the reducing thickness (Cuffe et al. 2012). Later, Wingert et al. showed that crystalline silicon nanotubes with shell thickness as thin as ~5 nm exhibited a thermal conductivity of ~1.1 W/m-K, which is below the limit predicted based on the classical size effect and even lower than the measured value for amorphous silicon nanotubes of similar geometries (Wingert et al. 2015). Considering that speed of sound is proportional to the square root of Young's modulus, the

observed reduction in the Young's modulus of silicon nanotubes is regarded as the underlying mechanism for the drastic thermal conductivity reduction in these tubes, which is called the elastic/acoustic softening effect. However, it has also been suggested in several reports that structure defects can lead to lower Young's modulus in relatively large silicon structures (Sadeghian et al. 2010, 2011). To verify whether the reduced Young's modulus and thermal conductivity of silicon nanotubes are due to size or defects, recently, Yang et al. conducted systematic measurements on two groups of silicon nanoribbons with the thickness of ~20 nm and ~30 nm (Yang et al. 2016). The silicon nanoribbons were prepared from the device layer of silicon-on-insulator (SOI) wafers and gone through the same fabrication process; and therefore, the defect concentration in the two thickness groups should be the same. As shown in **Figure 1.2(a)** and **(b)**, the thermal conductivities for the ~30 nm thick silicon nanoribbons can be fitted well by taking the classic size effect into account, while the data for ribbons with ~20 nm thickness are remarkably lower than those predicted. **Figure 1.2(c)** plots the measured Young's modulus as a function of the surface-area-to-volume (S/V) ratio of these ribbons, which shows that elastic softening occurs in the 20 nm-thick silicon nanoribbons. The deviation from the fitting based on the classical size effect, as shown in **Figure 1.2(d)**, occurs at approximately the same S/V value where the Young's modulus drops, indicating that the altered Young's modulus induces size effects beyond phonon boundary scattering. The room-temperature (300 K) thermal conductivities *versus* nanostructures' S/V ratio clearly delineates two regions where size effects beyond phonon boundary scattering are important or not.

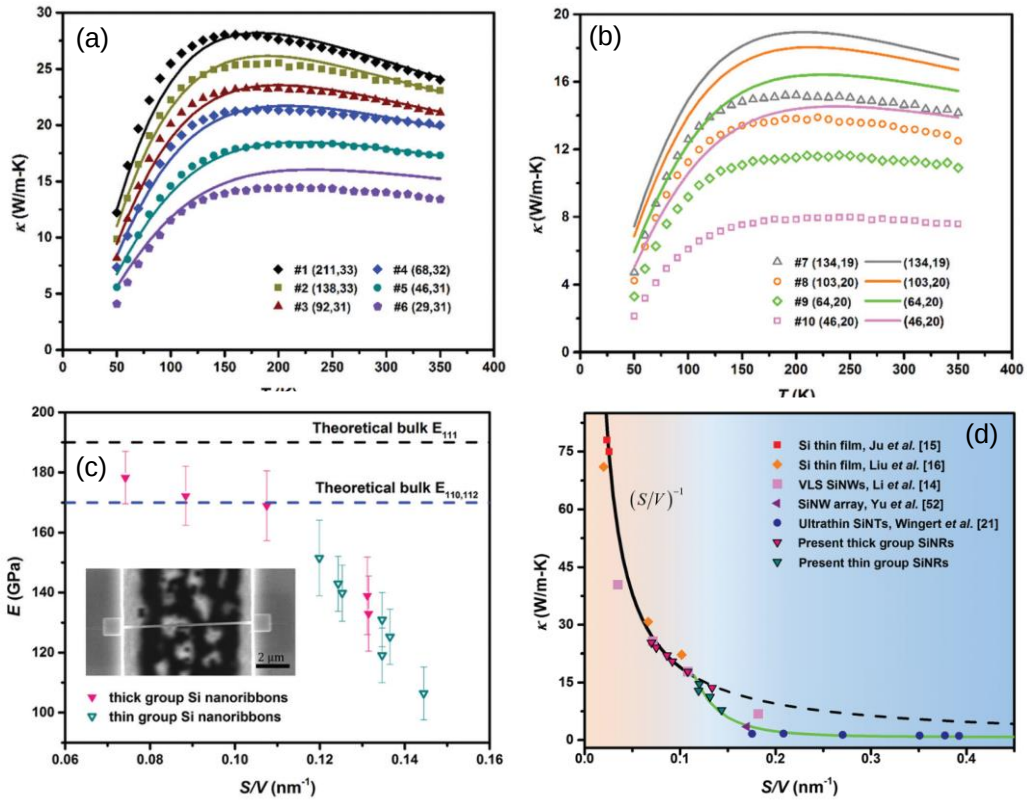


**Figure 1.2** (Yang et al. 2016) (a) For thick silicon nanoribbons, the modeled thermal conductivities (solid lines) agree well with the experimental data except for the sample of the smallest dimension. (b) For thin silicon nanoribbons, the calculated thermal conductivities are significantly higher than the measured values and the overestimation increases as the ribbon width reduces. (c) Measured Young's modulus of the silicon nanoribbons as a function of the S/V ratio. The colored dashed lines correspond to bulk values. The Young's modulus deviates from the bulk value at 0.11 $nm^{-1}$. The inset shows a silicon nanoribbon suspended across a trench of 7 μm wide with EBID Pt deposited at the two ends to anchor the ribbon for the Young's modulus measurement. (d) Room temperature thermal conductivities of various silicon nanostructures versus their S/V ratios, which clearly shows two regimes where size effects beyond phonon boundary scattering are important or not.

Surface roughness is another important factor that can reduce thermal conductivity to the amorphous limit and augment *ZT* value by up to two orders of magnitude from the bulk value. As shown in **Figure 1.3**, compared to silicon nanowires with a smooth surface grown by the vapor–liquid–solid (VLS) method, the silicon nanowires with rough surfaces achieved by the aqueous electroless etching (EE) method exhibit drastic thermal conductivity reduction (Hochbaum et al.

2008). Further, through systematic measurements on controllably roughened VLS silicon nanowires, the significantly reduced thermal conductivity is attributed to the frequency-dependent phonon scattering from rough surfaces (Lim et al. 2012). The surface roughness can interact with a broadband spectrum of phonons in silicon nanowires to restrict phonon transport below the Casimir limit. Besides diameter, three other independent parameters, including root-mean-square roughness, correlation length and power spectrum, can significantly affect thermal transport in rough silicon nanowires.

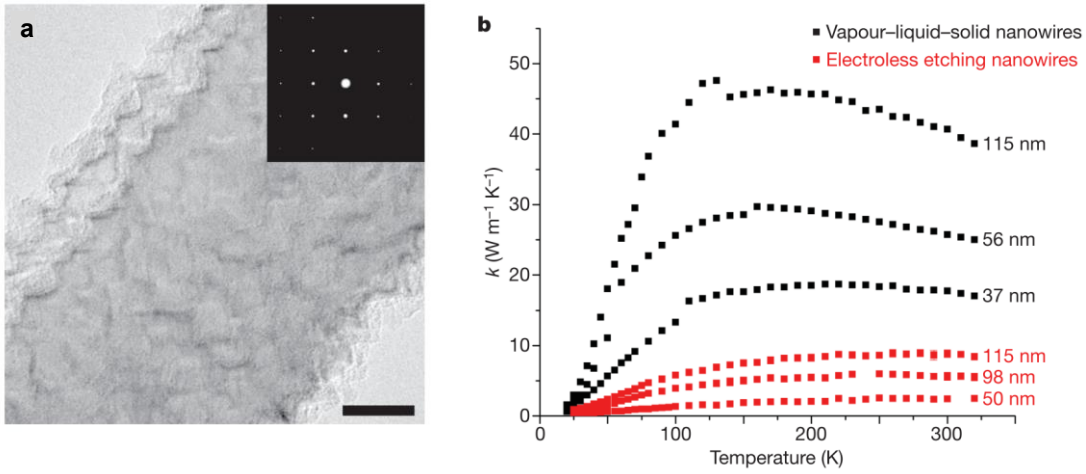


**Figure 1.3** (Hochbaum et al. 2008) (a) Bright-field TEM image of a segment of an EE silicon nanowire. The roughness can be clearly seen at the surface of the wire. The selected area electron diffraction pattern (inset) indicates that the wire is single crystalline all along its length. (b) The temperature-dependent thermal conductivity of VLS (black squares) and EE nanowires (red squares).

Except for simple straight structures, the thermal transport properties of nanowires with complex morphologies has been characterized recently. As shown in **Figure 1.4(a)**, the silicon nanomesh films fabricated by electron beam lithography possess a low thermal conductivity of ~2 W/m-K, which is two times lower than that of an array of silicon nanowires with relatively larger S/V ratios (Yu et al. 2010). The observed thermal conductivity reduction was first attributed to a coherence effect in which holes played the role of Bragg reflector. It was suggested that as the

periodicity of nanomeshes was on the order of the thermal phonon MFP, phonon coherence occurred to flatten the band structure by reducing the Brillouin zone and thus significantly lowered the phonon group velocity. The phonon coherence effect was also claimed by Hopkins et al. from the low thermal conductivity along the cross-plane direction of nanomeshes and the resulting thermal conductivity reduction could not be predicted by only considering boundary scattering at the interfaces (Hopkins et al. 2011). Later, Dechaumphai and Chen numerically predicted the low thermal conductivity of silicon nanomeshes with a partial coherent model by treating the phonons with MFP smaller than the characteristic size of phononic crystals as particles and the other phonons with MFP larger than the characteristic size as waves (Dechaumphai and Chen 2012). They concluded that the critical sizes of phononic crystals, such as neck and pitch sizes of the nanomesh structure, led to the phonon group velocity reduction in the wave regime and strong boundary scattering in the particle regime. Later, the phonon coherence mechanism was reinforced with the experimental and theoretical studies of nanomeshes with circular holes (Alaie et al. 2015; Anufriev and Nomura 2015). However, the theoretical study conducted by Jain et al. suggests that the occurrence of phonon coherence is based on (a) specular scattering between phonons and pore sidewalls and (b) no phonon-phonon scattering between consecutive pore collisions which keep the phase and frequency unchanged (Jain et al. 2013). Jain et al. applied Monte Carlo (MC) model to predict in-plane thermal conductivity of silicon nanomeshes by treating phonons as particles with bulk properties and the results agree well with the experimental data of Yu et al, which indicates that coherent phonon transport is not important as the feature size is larger than 100 nm. The incoherent boundary scattering in nanomeshes has also numerically demonstrated by Ravichandran and Minnich by adding the effect of amorphous layer of 3.5 nm into the calculations (Ravichandran and Minnich 2014). However, the thickness of native oxide layer on the silicon

surface is widely believed to be of only ~2 nm, which is significantly thinner than the assumed oxidized thickness of 3.5 nm. In view of the large S/V ratio of the nanomeshes studied by Yu et al., acoustic softening effect could occur to cause additional thermal conductivity reduction by reducing phonon group velocity (Chen et al. 2019). The less importance of phonon coherence has also been demonstrated in graphene nanomeshes (Feng and Ruan 2016).

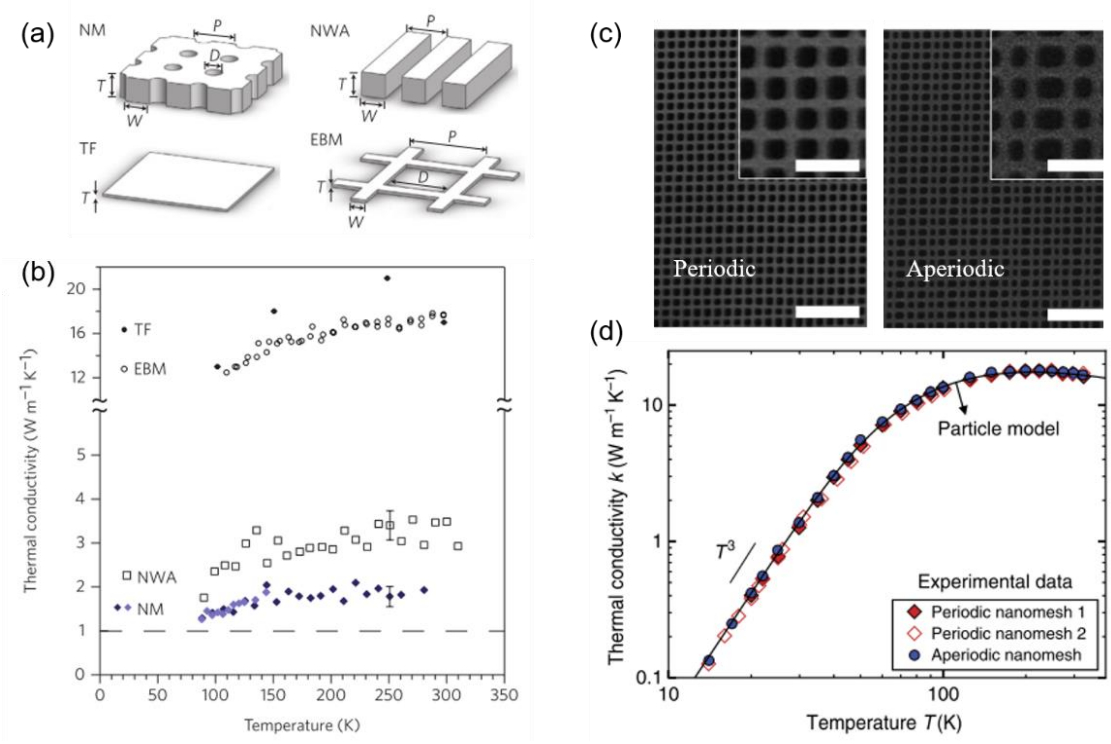


**Figure 1.4** (a) Geometry of two nanomesh films (NM1 and NM2) and three reference systems including thin film (TF), mesh that was defined by electron-beam lithography (EBM) and array of silicon nanowires (NWA) (Yu et al. 2010). (b) Thermal conductivity versus temperature for two nanomesh devices (diamonds) and the three reference devices. The TF (solid circles) and EBM devices (open circles) have similar thermal conductivities as a result of their similar film thicknesses. The NWA nanowires (open squares) have lower thermal conductivities, as a result of their larger S/V ratios compared to the TF and EBM devices. The nanomesh devices, although having significantly lower S/V ratios compared to the NWA device, exhibit a thermal conductivity that is factor of 2 lower (Yu et al. 2010). (c) SEM image of a periodic silicon nanomesh with a controlled periodicity of 100 nm (Lee et al. 2017). (d) Experimental data (points) and the BTE particle model with diffuse surfaces (line) show excellent agreement for $\kappa(T)$ of two periodic and one aperiodic nanomeshes. The very similar $\kappa$ between the three samples at all $T$ indicate negligible coherence effects for thermal transport in silicon nanomeshes for periodic lengths larger than 100 nm and temperatures above 14 K (Lee et al. 2017).

More recently, Lee et al. isolated the phonon coherence effect by performing thermal conductivity measurements on periodic and aperiodic silicon nanomeshes with the same S/V ratio (Lee et al. 2017). As shown in **Figure 1.4(d)**, the thermal conductivities of periodic and aperiodic nanmomeshes are almost identical (within 6% uncertainty), which also match the prediction based on MC ray-tracing simulations combined with Boltzmann transport equation. The results indicate that phonon coherence is unimportant for thermal transport in silicon nanomeshes with periodicities larger than 100 nm and at the temperatures above 14 K; and phonon backscattering is the underlying mechanism for thermal conductivity reduction of nanomeshes. The phonon boundary scattering mechanism has also been confirmed in silicon nanomeshes with staggered holes (Lim et al. 2016).

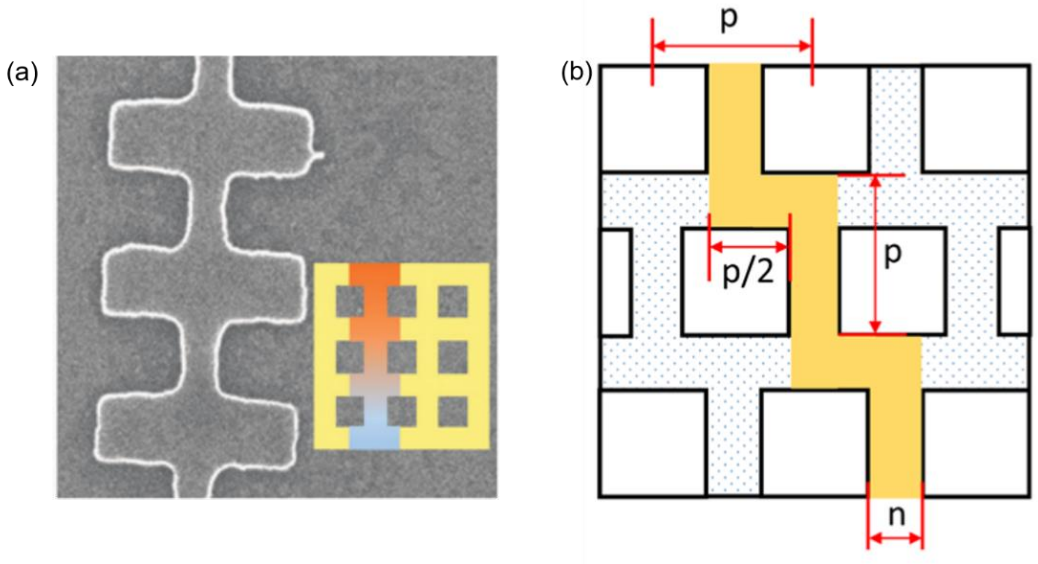


**Figure 1.5** Fishbone and kinked silicon nanoribbons could be regarded as the building blocks for nanomeshes with aligned and staggered hole arrangements, respectively (Yang et al. 2019).

As the building blocks for nanomeshes, fishbone (**Figure 1.5(a)**) and kinked (**Figure 1.5(b)**) nanoribbons have been investigated for the underlying physics of phonon transport properties. The reduced thermal conductivity of silicon fishbone nanoribbons as compared to the corresponding

straight ones has been reported and the geometry effect on thermal transport in fishbone nanoribbon has been discussed (Maire et al. 2018; Maire and Nomura 2014; Nomura and Maire 2015). Nomura and Maire attibuted the mechanism of thermal conductivity reduction to the dual wave and particle nature of phonons when phonon transport is ballistic in fishbone (Nomura and Maire 2015). However, phonon coherence only occurs under very strict conditions. Later, Maire et al. used numecial simulations to explain the experimetnal data through consideration of the phonon boundary scattering effect and suggested that the difference probably stemmed from the phonon trapping effect (Maire et al. 2018). Recently, Yang et al. investigated thermal transport through silicon fishbone nanoribbons and disclosed an unexpected effective thermal conductivity (Yang et al. 2019). As shown in **Figure 1.6(a)**, the theraml codnuctivity becomes smaller for fishbone nanoribbons with wider fins. However, the S/V ratio of the fishbone nanoribbons reduces as the fin width expands. If only considering the classical size effect, the size dependence of the theraml codncutivity cannot be well explained, as the fishbone nannoribbons with wider fins would experience weaker phonon boundary scattering effect. Through extracting the room-temperature thermal resistance of the constriction, backbone and fin, they found that the constriction resistance induced by the cross-section difference between backbone and fin increases significantly as the fin width increases (**Figure 1.6(b)**), which contributes to the thermal conductivity reduction. The constriction effect was also manifested by the temperature distribution discontinuity near the constriction area in MD simulations as shown in **Figure 1.6(c)**. As described in **Figure 1.6(d)**, the effective phonon MFP of the ribbons with a larger fin width is longer for phonons arriving at the constriction, which boosts the ballistic constriction resistance and leads to a lower thermal conductivity.

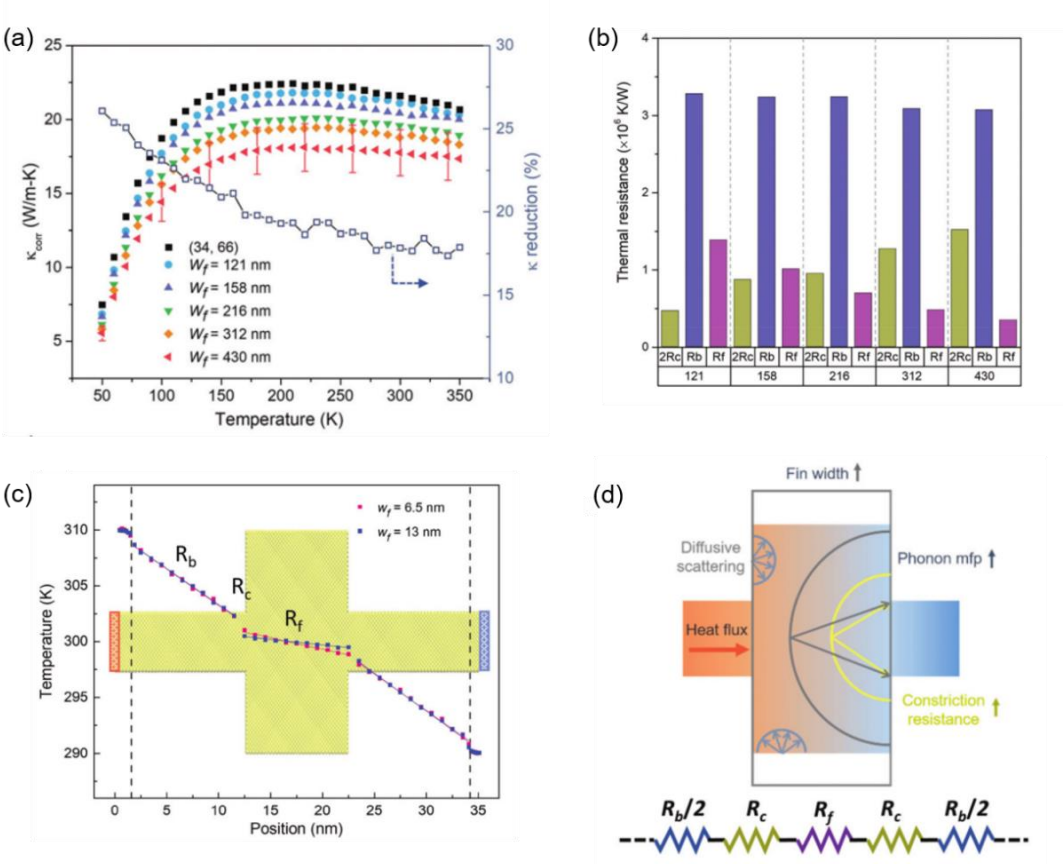


**Figure 1.6** (Yang et al. 2019) (a) Temperature dependent corrected thermal conductivity for five different Si fishbone nanoribbons. (b) Extracted thermal resistance of the constriction (*Rc*), backbone (*Rb*) and fin section (*Rf* ) for five Si fishbone nanoribbons at 300 K. (c) Simulated temperature distribution along the axial direction of the fishbone nanoribbons with fin widths of 6.5 nm and 13 nm. (d) Schematic diagram showing the ballistic thermal constriction resistance. Within the hemisphere of the ballistic phonon mean free path, only phonons pointing to the small constriction can pass through. The bottom panel is an illustration of the thermal resistive network.

For kinked nanostructures, Jiang et al. predicted the thermal conductivity of silicon nanowires with periodic kinks by using MD simulations. Compared with the corresponding straight silicon nanowires of equivalent length, at room temperature the kink structure was able to induce as high as 70% thermal conductivity reduction as the number of kinks increases to 11. Two mechanisms are claimed to be responsible for the kink effect on thermal conductivity reduction: (a) the interchanging between the longitudinal and transverse phonon modes, and (b) the pinching effect for the twisting and transverse phonon modes in the kinked silicon nanowires (Jiang et al. 2013).

In another MD simulations, Xiong et al. reported that the thermal conductivity of a set of silicon phononic metamaterial nanowires of a zigzag configuration with a turning angle of 109.4 ° could be reduced by 65% from the straight wire and a purely geometry-induced minimal thermal conductivity is observed at a specific period depending on the nanowire diameter (Xiong et al. 2014). The analysis shows that the minimal thermal conductivity arises from the disappearance of favored atom polarization directions. Recently two experimental studies on kinked nanowires have been reported. Through systematic measurements of straight and kinked boron carbide nanowires with different sizes and carbon concentrations, Zhang et al. disclosed that a single kink could cause up to 36% thermal conductivity reduction, which is equal to a ~30 times thermal resistance of a straight wire segment of equivalent length (Zhang et al. 2017). The numerical results from an MC simulation showed that the remarkable kink resistance arose from backscattering of highly focused phonons at the kink region. The mechanism is strongly supported by the enhanced thermal conductivity of kinked nanowires with defects in the kink region as shown in **Figure 1.7(a)** and **(b)**. The counter-intuitive results suggest that the defects in the kink, instead of posing thermal resistance, facilitate phonon transport through the kink via scattering phonons to the opposite side. The other experimental work conducted by Yang et al. presents the thermal conductivity of straight and kinked silicon nanoribbons that are prepared with microfabrication. For kinked silicon nanoribbons that are 34 nm thick and 141 nm wide, the measured thermal conductivity first decreases and then exhibits a steep increasing trend as the period length drops to a level at which a straight heat transfer channel opens between the heat source and the sink (**Figure 1. 7(c)** and **(d)**) (Yang et al. 2019). Detailed MC ray-tracing studies through treating phonons as particles reveal that the minimum thermal conductivity could be attributed purely to the geometrical effect, as a result of two competing factors of phonon backscattering at the kink boundaries and leaking

through the open view channels. The kinked silicon ribbons along the ⟨100⟩ crystalline direction have a more significant thermal conductivity reduction than that along the ⟨110⟩ direction, confirming that phonon focusing due to elastic anisotropy could lead to different levels of kink effect. The kink effect on the thermal conductivity of silicon nanoribbons is much weaker than that in boron carbide nanowires, which is attributed to the much weaker elastic anisotropy in silicon than in boron carbide.

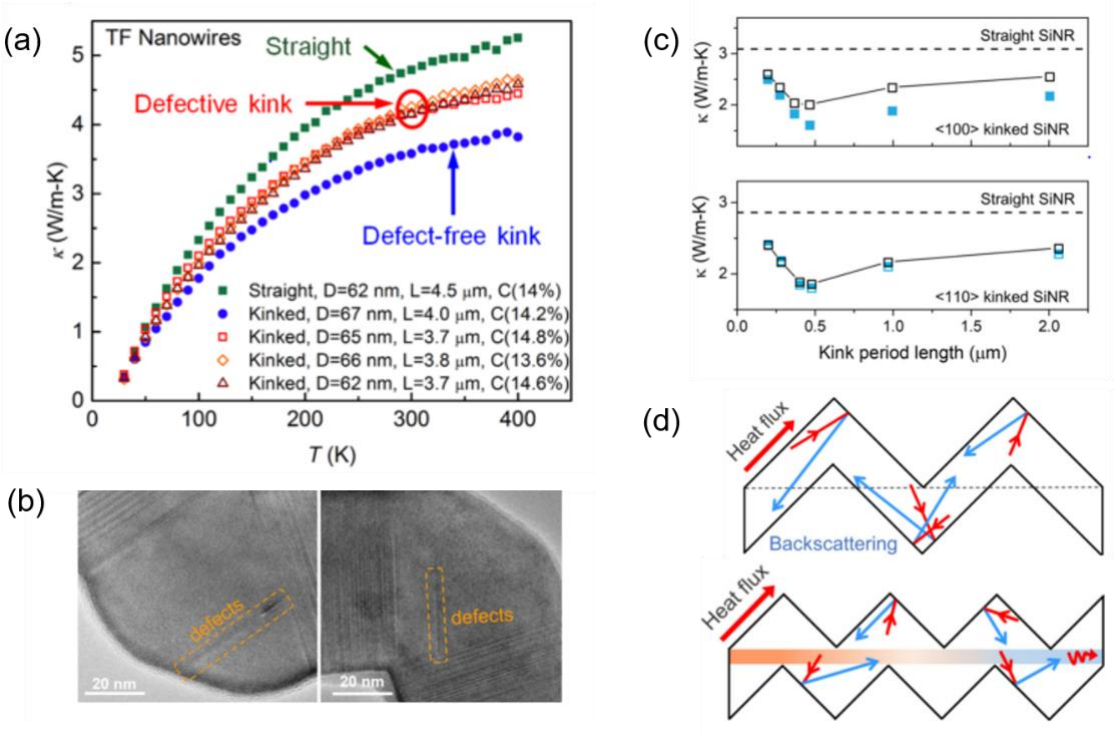


**Figure 1. 7** (a) Thermal conductivity of boron carbide nanowires that are straight, with defect-free kinks, and with defective kinks, respectively (Zhang et al. 2017). (b) TEM images show the defects in the kinks of kinked boron carbide nanowires (Zhang et al. 2017). (c) Measured thermal conductivity of ⟨100⟩ and ⟨110⟩ kinked silicon nanoribbons (34 nm wide, 141 nm thick) plotted as a function of kink period length at 30 K, where the dashed lines represent the thermal conductivity of the corresponding straight ribbon and the empty symbols are the fitted results based on MC ray-tracing simulation (Yang et al. 2019). (d) Schematic illustrations of phonon transport through kinked ribbons with different period lengths (Yang et al. 2019).

### 1.2 Contact Resistance between Individual Nanostructures

Carbon nanotubes (CNTs) and graphene, owing to their excellent mechanical, electrical, thermal and chemical properties as well as the large S/V ratio, have been extensively investigated as nanofillers to improve thermal and electrical performance of lightweight polymeric composites. However, carbon nanofillers-based composites have not reached their potential as predicted based on the particle mixing theory. Apart from the filler purity, size and structural variations, it has been projected that numerous contacts between fillers and interfaces between the medium and fillers could play a critical role in the resulting properties.

For thermal transport in CNT-based composites, the upper and lower bounds of the effective thermal conductivity are essentially generated in two scenarios where the fillers are arranged in a parallel and a serial configuration, respectively (Wang et al. 2008). The parallel model assumes no contact resistance existing between fillers and overestimates the effective thermal conductivity of the composite, which is expressed as $\kappa_c = \kappa_f \phi_f + \kappa_m \phi_m$, where $\kappa_c$, $\kappa_f$ and $\kappa_m$ are the thermal conductivity of the composite, the filler, and the polymer matrix, respectively, and $\phi_f$ and $\phi_m$ are the volume fraction of the filler and the polymer matrix. The minimum effective thermal conductivity is predicted by a series model which assumes no direct contact between fillers and is calculated as $\frac{1}{\kappa_c} = \frac{\phi_f}{\kappa_f} + \frac{\phi_m}{\kappa_m}$. Experimentally, the measured thermal conductivity of the composites with the addition of highly conductive fillers is lower than the expected value, which is generally believed to be a result of non-negligible contact resistance. Through using picosecond transient absorption measurement, Huxtable et al. reported an interface thermal resistance of ~$8.3 \times 10^{-8}$ $m^2$-K/W between single-wall CNT (SWCNT) and sodium dodecyl sulphate surfactant, which is much lower than the value estimated from the intrinsic thermal conductivity of fillers and their volume fraction (Huxtable et al. 2003). Later, Prasher et al. suggested that the contact thermal conductance

at tube-tube junctions in the CNT mats could be as small as 3 pW/K (Prasher et al. 2009), which is one order of magnitude lower than the numerically predicted value of 50 pW/K for SWCNTs (Estrada and Pop 2011; Prasher et al. 2009). To provide experimental data of contact thermal resistance between CNTs, Yang et al. measured the total thermal resistance of two individual MWCNTs with a cross or aligned contact using suspended microdevices (Yang et al. 2010). The results show that the contact conductance for aligned MWCNTs is on the order of $10^{-6}$ W/K, while the contact conductance reduces to be on the order of $10^{-8}$ W/K as the contact area decreases from the aligned contact to a cross contact. The normalization with respect to the contact area leads to a contact thermal resistance on the order of $10^{-9}$ $m^2$-K/W, one order of magnitude lower than that from MD simulations. Later on, Yang et al. derived the thermal conductance per unit area at the tube-tube contact through measuring single and contacted CNTs with the same diameter (Yang et al. 2014). As shown in **Figure 1.8**, the contact thermal conductance per unit area, which is conventionally regarded as approximately the same for CNTs with different diameters, increases as the diameter increases. Further normalization with respect to the diameter, interestingly, renders the contact thermal conductance per unit area for different tubes overlap with each other. The unexpected size dependence of contact thermal conductance per unit area reveals the unexpectedly long phonon MFP along the *c*-axis direction of graphite, which has been experimentally demonstrated to be ~200 nm (Fu et al. 2015). With the long MFP along the cross-plane direction, phonons can ballistically transport through the contact and be reflected by the innermost layer of the receiving tube back into the emitting tube, which effectively reduces the contact thermal conductance. Only phonons that get scattered and thermalized in the receiving tube could contribute to thermal transport at the tube contact.

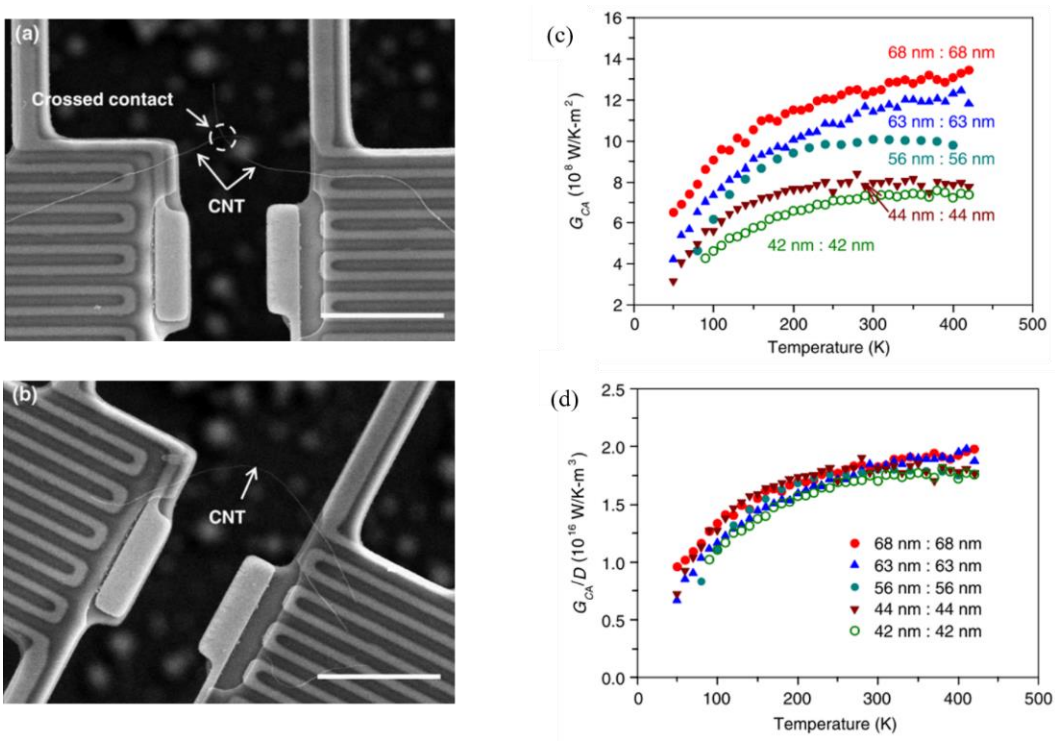


**Figure 1.8** Thermal conductance of point contact between two carbon nanotubes (Yang et al. 2014). (a) SEM micrographs of one measured sample composed of two MWCNT segments forming a cross contact between the heat source and sink and (b) one of the two segments is realigned on the microdevice to evaluate the thermal resistance of the MWCNT segments in the cross-contact sample. Scale bar: 7.5 μm. The diameter of this tube is 63 nm. (c) The contact thermal conductance per unit area versus temperature. (d) The contact thermal conductance per unit area normalized with the tube diameter, which approximately collapses into one line. Analyses show that contact thermal conductance is proportional to $D^{2.4}$ and the contact area is proportional to $D^{1.4}$. The labels in the figure denote the diameters of the two segments forming a crossed contact.

For electron transport, the determining factor in carbon material-based composites is the formation of the conductive percolation network among fillers. The possibility of creating an effective percolation path lies on the filler concentration ($p$). The transition from an insulating to a conductive phase occurs at a critical concentration ($p_c$) (Kirkpatrick 1973). Above $p_c$, the electrical conductivity ($\sigma$) follows a power law as $\sigma \sim (p - p_c)^a$, where the exponent $a$ is related to the dimensionality of the percolating network. Along the conductive percolation path the intersection of two CNTs forms a barrier for electron transport, which could significantly modify

the overall electrical performance of CNT-based materials and composites (Blackburn et al. 2008; Li et al. 2007). Fuhrer et al. suggested that the junction between metallic and semiconducting SWCNTs led to a rectifying Schottky barrier (Fuhrer et al. 2000), while the electrical conduction of two contacted metallic SWCNTs displayed the power-law behavior as a function of temperature and voltage, which could be fitted well by a Luttinger Liquid model for electron tunneling transport through the contact (Postma et al. 2000). In carbon material-based networks or composites, the electrical transport behavior can generally be described by variable range hopping (VRH) mechanism or thermal fluctuation induced tunneling (FIT) mechanism, which are schematically illustrated in **Figure 1.9** (Jouni et al. 2017). The VRH model was first pointed out by Mott and Davis, describing the thermally activated electron jumping between localized electronic sites in non-crystalline materials at low temperatures (Mott and Davis 1979). The temperature dependence of the electrical conductivity is expressed as

$$\sigma = \sigma_0 \exp\left[-\left(\frac{T_0}{T}\right)\right]^{\frac{1}{1+d}}, \tag{1.3}$$

where $\sigma_0$ is a constant, $T_0$ is the characteristic temperature, and $d$ is the dimension (2 or 3). With consideration of the quadratic reduction of the density of states (DOS) at the Fermi level, Efros and Shklovskii proposed a temperature dependence of electrical conductivity following a $d$=1 law (ES-VRH) (Efros and Shklovskii 1975). On the other hand, as most of the conduction electrons are delocalized and free to move over a larger distance, the electrical conduction is dominated by electron tunneling across the large insulating barriers in the conducting pathways rather than by hopping between localized sites. The tunneling transport is described by the FIT model as (Logakis et al. 2009)

$$\sigma = A\exp\left[-\left(\frac{T_b}{T+T_1}\right)\right], \tag{1.4}$$

where $A$ is a constant, $T_b$ is a constant related to the energy required for a charge carrier to cross the potential gap, and $T_1$ is the thermally activated conduction temperature.

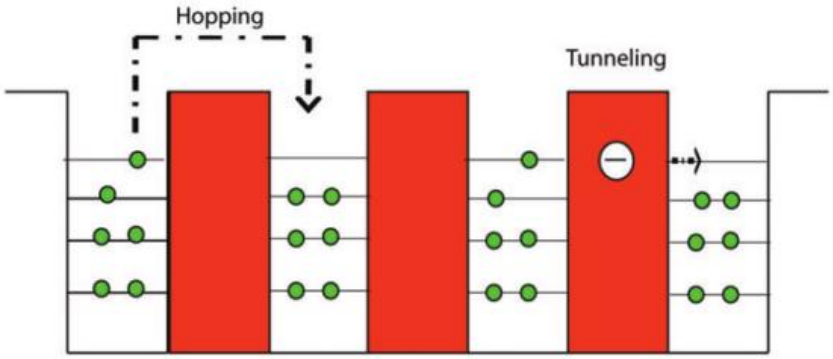


**Figure 1.9** Hopping and tunneling transport of charge carriers (Jouni et al. 2017).

To date, most understandings on transport through CNT-CNT contacts are inferred from measurements of CNT bundles, thin films, or bulk materials (bulky papers) involving a large amount of CNT contacts. It is challenging to draw solid conclusions on the transport phenomena at the contacts because complications from the intrinsic properties of CNTs, variations of contact morphologies, and changes in the temperature jump at the contacts could all lead to similar observations. In SWCNT networks, electron hopping transport has been observed (Fuhrer et al. 1999; Gaál et al. 2000; Yosida and Oguro 1999) and the transport mechanism is found to be dependent on the relative content of the tube type (Yanagi et al. 2010). As shown in **Figure 1.10**, as the concentration of semiconducting SWCNTs increases, the conduction mechanism changes from weak localization (WL) to VRH and finally becomes ES-VRH for semiconducting SWCNT networks. However, some studies show that the temperature dependence of the electrical resistance of semiconducting SWCNT-enriched and metallic SWCNT-enriched films follows FIT model (Blackburn et al. 2008). In addition, Skákalová et al. found that the network thickness was a factor to affect the electrical transport behavior; electron tunneling transport occurred in thick SWCNT

networks, while as the thickness was reduced hopping conduction appeared due to the difficulty to obtain good metallic percolation paths in the thin networks (Skákalová et al. 2006). For multiwall carbon nanotube (MWCNT) networks, the electrical conduction basically follows VRH model (Aggarwal et al. 2007; Bandow et al. 2007; Yosida 1999). In CNT-based polymeric composites where the nanotubes are coated with insulating polymer, tunneling transport dominates (Kilbride et al. 2002; Li et al. 2007; Logakis et al. 2009; Sundaray, Choi, and Park 2010). However, in some other studies the temperature dependence of electrical conductance of CNT composites agrees well with the VRH model (Benoit et al. 2002; Menon and Pillai 2012).

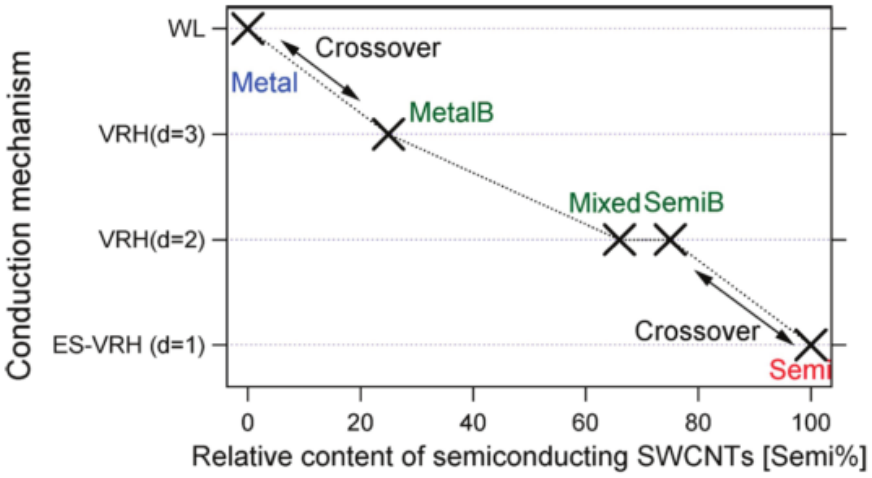


**Figure 1.10** Phase diagram of conduction mechanisms in SWCNT networks as a function of relative content of semiconducting SWCNTs. Weak localization: WL. Variable range hopping: VRH. Coulomb gap VRH by Efros & Shklovskii: ES-VRH (Yanagi et al. 2010).

For thermoelectric properties, Tian et al. measured the thermoelectric power (TEP) of graphitic nanotube bundles and attributed the positive value to the contribution of metallic and semiconducting tubes (Tian et al. 1997). However, opposite experimental results have been reported later. As shown in **Figure 1. 11**, Baxendale et al. found that the TEP of tube mats and pellets with numerous random contacts is positive, while graphite flake and MWCNT bundle with aligned arrangement exhibit negative TEP (Baxendale et al. 2000). They believe that the positive

TEP for randomly arranged CNT networks is not an intrinsic property of tube fillers but a consequence of electron hopping conduction that induces significant positive components at inter-tube junctions. Assuming each percolating pathway contains a randomly oriented set of contact barriers, the TEP of CNT-based materials or composites is the sum of a linear metallic term and a variable range hopping term weighted with $T^{1/2}$ that reflects the "freezing-out" of semiconducting contributions at low temperature (Kaiser et al. 1999), which is expressed as

$$S(T) = bT + cT^{\frac{1}{2}} \exp\left[-\left(\frac{T_0}{T}\right)^{\frac{1}{1+d}}\right], \tag{1.5}$$

Here, *b* and *c* are the constants for the metallic and semiconducting contributions, respectively. By introducing multiple parameters, the heterogeneous model gives a good fit for MWCNT mats (Choi et al. 2003a) and CNT-based composites (Hewitt et al. 2012). However, no research has been done to directly unveil the thermoelectric properties at an individual contact between CNTs.

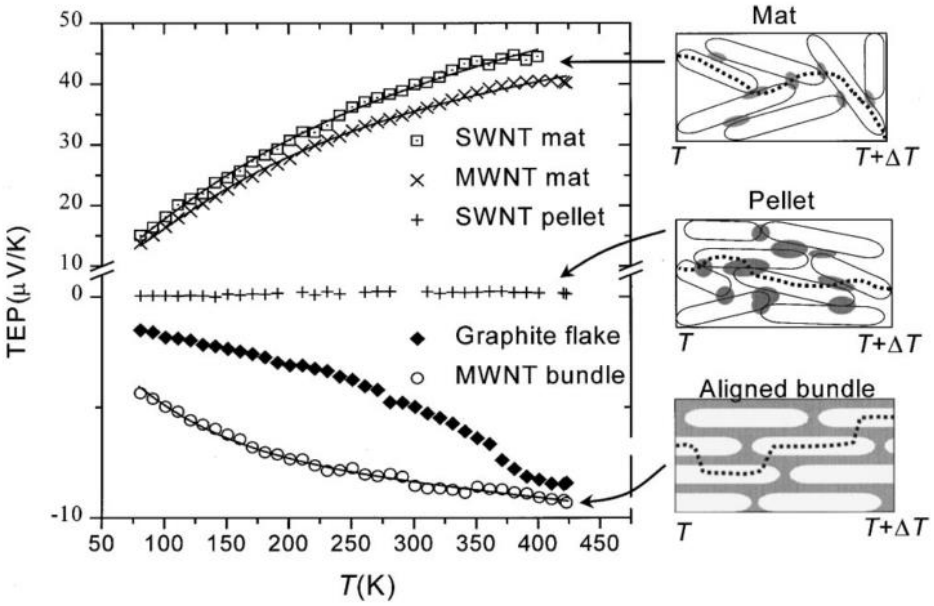


**Figure 1.11** Thermoelectric power versus temperature (Baxendale et al. 2000). The schematic diagrams to the right of the plot are 2D representations of the nature of the thermal current paths (dotted lines) for the aligned nanotube bundle, mat, and pellet samples. The spatial extent of inter-tube barriers is schematically indicated by the gray areas.

Except for CNTs, metal nanowires are regarded as promising nanofillers to improve thermal and electrical performance of composites that can be applied in various electronic and thermal applications. However, no research regarding contact thermal and electrical properties have been carried out on metal nanowires. Previous studies have measured thermal resistance of metal interfaces (Gundrum et al. 2005; Wilson and Cahill 2012). With the thermal interface conductance of the Pd/Ir interface derived from the difference in the thermal conductivities for different thickness multilayers, Wilson and Cahill have demonstrated that the Wiedemann-Franz (W-F) law is applicable to relate the thermal interface conductance and the specific electrical resistance between Pd and Ir (Wilson and Cahill 2012). Recently, Cui et al. (Cui et al. 2017) and Mosso et al. (Mosso et al. 2017) respectively measured the thermal and electrical conductance of single-atom junctions of gold and demonstrated the validation of W-F law at an atomic contact level (**Figure 1.13**). Inspired by these experimental findings, numerical calculations have been performed. Klöckner et al. conducted density functional theory (DFT) calculations and MD simulations to study the role of phonons in thermal transport at atomic contacts. For gold and platinum, electrons are dominant energy carriers and thus the W-F law gives a good estimation for thermal conductance, while the non-negligible phonon contribution (up to 40%) to contact thermal conductance in aluminum leads to a deviation of the effective Lorenz number from the Sommerfeld value (Klöckner et al. 2017). Other than the effects of phonon contribution, DFT calculations performed by Bürkle and Asai showed that other factors including temperature, gate voltage and atomic configuration could cause the effective Lorenz number to deviate from the Sommerfeld value, which could be up to 30% for gold and up to 350% for platinum (Bürkle and Asai 2018).

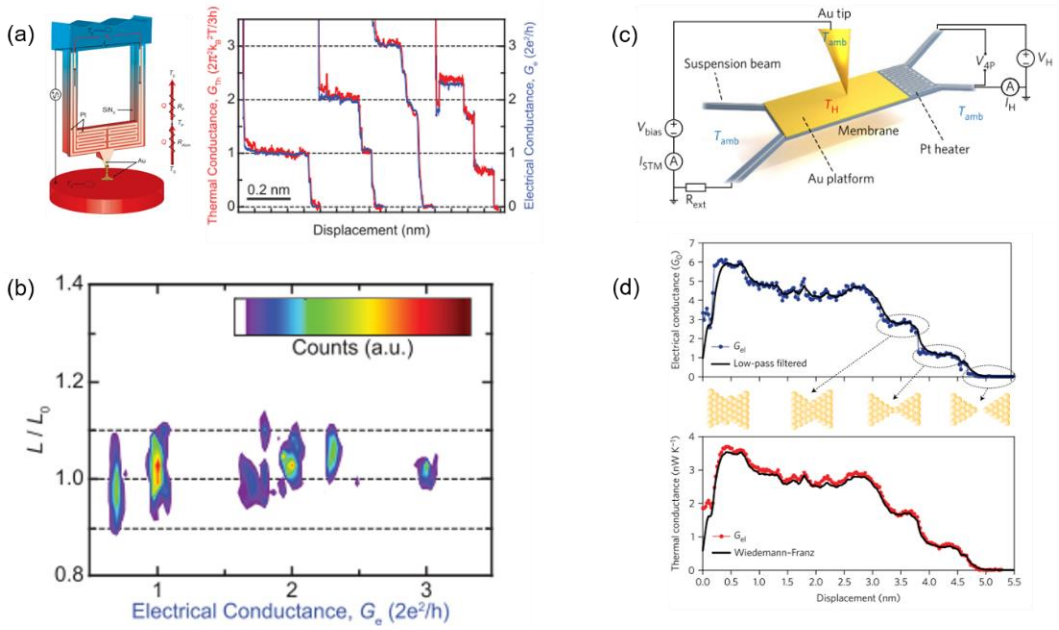


**Figure 1.12** Validation of the W-F law at atomic contact level. (a) Representative traces of thermal and electrical conductance measured while reducing the transverse constriction of gold atomic junctions by displacing the gold tip of the C-SThM probe away from the gold substrate (Cui et al. 2017). (b) Histogram of the ratio of the thermal conductance to the electrical conductance, showing good agreement with the Lorenz number (Cui et al. 2017). (c) Schematic diagram of the experiment (Klöckner et al. 2017). (d) Both the thermal and the electrical conductance show quantization steps, in agreement with the W-F law (Klöckner et al. 2017).

### 1.3 Summary

Various factors including classic size effect, acoustic softening, and surface roughness on phonon transport through nanowires have been investigated in the past two decades, which provides a much more comprehensive understanding for thermal transport mechanisms in nanostructures. However, while contacts and kinks between nanomaterials could play critical roles in various situations, much less efforts have been devoted to exploring energy transmission through these junctions. Moreover, novel observations such as diameter dependent contact thermal conductance per unit area between MWCNTs point to rich physics at these junctions and call for more investigations of thermal transport through contacts and kinks between nanostructures.

In the following chapters, we employ a well-established micro-thermal bridge method to study the thermal and electrical transport properties at point contacts between silver nanowires. We also use MD simulations to explore the kink effect on thermal transport in silicon nanowires. The dissertation is organized as follows.

Chapter 2 introduces the implementation of the micro-thermal bridge method with enhanced measurement sensitivity and the fabrication process of the suspended microdevice. To achieve more accurate measurement results, we design a three-membrane device to eliminate the effect of background thermal conductance and develop a wetting process that can make an intimate contact between nanowire and membranes to reduce wire-membrane contact resistance.

Chapter 3 presents systematic studies on silver nanowires and their contacts. We are the first to disclose the elastic stiffening effect on electrical and thermal transport through individual silver nanowires and show the enhanced effective Lorenz number of the point contact owing to the non-negligible phonon contribution. We also discover that the silver nanowires are better nanofillers to enhance thermal performance of nanocomposites.

Chapter 4 provides clear evidence for electron hopping conduction at contacts between CNTs and demonstrates that electron hopping at contacts can improve thermoelectric performance of CNT-based materials.

Chapter 5 discusses a simulation work on thermal transport in kinked silicon nanowires, which discloses that kinks pose thermal resistance by reflecting phonons back into the straight segment where they come from.

Chapter 6 summarizes the key findings in this dissertation.

# Chapter 2

## Experimental Setup and Device Fabrication

Since many interesting thermal properties could exist in various nanowires, several techniques have been developed to characterize their thermal properties, including the 3 omega method (3ω) (Hasegawa et al. 2013; Lee et al. 2013), Joule self-heating measurement (Pop et al. 2006), Raman thermometry (Doerk et al. 2010) and micro-thermal bridge method with suspended microdevice (Li et al. 2003; Shi et al. 2003). Among these measurement techniques, the micro-thermal bridge approach has produced the most experimental results over the past two decades in studying the thermal, electrical and thermoelectric properties of 1D nanostructures, such as quasi-1D nanowires (Yang, Tao, et al. 2019; Zhang et al. 2018), polymeric nanoribbons (Zhang et al. 2018), carbon and silicon nanotubes (Kim et al. 2001; Wingert et al. 2015; Yang et al. 2011), contacts and interfaces between individual nanostructures (Yang et al. 2012, 2014, 2017), and individual nanostructures with complex morphology (Yang, et al. 2019; Zhang et al. 2017).

The micro-thermal bridge method was first developed to measure thermal and thermoelectric properties of individual nanostructures, which involves the four-point I-V measurement scheme with a thermal measurement sensitivity of ~300 pW/K (Kim et al. 2001; Li et al. 2003; Shi et al. 2003). Two major noise sources in the four-point scheme limit the measurement sensitivity, which are the radiation dominated background conductance and temperature fluctuation of the sample holder in the cryostat (~100 mK). To achieve a higher measurement sensitivity, Wingert et al. further developed the measurement scheme by introducing a Wheatstone bridge circuit with a reference device at the sensing side (Wingert et al. 2012). As both the measurement and the reference devices experience the same temperature fluctuation, the error from the sample holder temperature fluctuation can be eliminated through common mode rejection, which gives rise to a

sensitivity as low as ~10 pW/K. Herein, this chapter mainly introduces the device fabrication and experimental measurement approach with the Wheatstone bridge scheme.

## 2.1 Measurement Device

As shown in **Figure 2.1**, the microdevice consists of two suspended low stress silicon nitride (SiNx) membranes of 22.5 μm × 27.3 μm which are supported by six 0.5 μm thick, 413.25 μm long and 2.3 μm wide SiNx beams on the silicon substrate. On top of each SiNx membrane, a thin layer of platinum resistance thermometer (PRT) made of 30 nm thick and 600 nm wide platinum (Pt) line is patterned, which can also serve as a microheater through Joule heating. Each PRT is connected to four 400 μm × 500 μm Pt bonding pads on the substrate through the 1.5 μm wide Pt leads on the corresponding long SiNx beams. Two 1.0 μm wide Pt electrodes are fabricated at the edge of the SiNx membranes which are connected to the Pt bonding pads through Pt leads on the other two beams. The electrodes on the microdevice can enable simultaneous four-point electrical resistance measurement and Seebeck coefficient measurements. To prevent electrical contacts between the sample and the PRT that could interfere thermal measurements, a layer of 250 nm thick low temperature silicon oxide (LTO) is deposited on top of the serpentine PRT. In addition, the entire silicon substrate underneath the SiNx membranes can also be etched away to allow for transmission electron microscopy (TEM) examination of the measured sample.

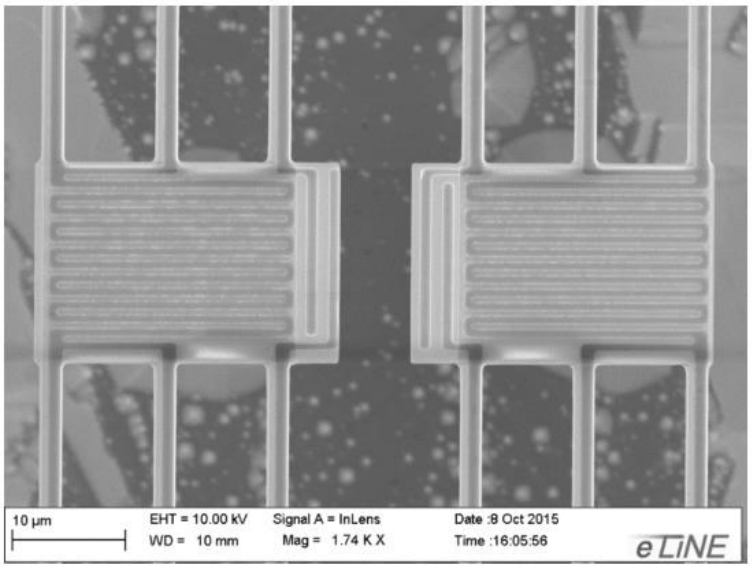


**Figure 2.1** SEM micrograph of the suspended microdevice with electrodes and integrated microheaters/thermometers made from serpentine Pt lines.

## 2.2 Device Fabrication

The suspended devices are batch-fabricated on 4-inch (100 mm) silicon wafers and the fabrication process is shown in **Figure 2.2**. First, 0.5 µm thick low stress SiNx films are grown on both sides of a silicon wafer using low pressure chemical vapor deposition (LPCVD) (**Figure 2.2(b)**). Then 5 nm thick Chromium (Cr) and 30 nm thick Pt films are coated on one side of the silicon wafer by sputtering deposition (**Figure 2.2(c)**). The Cr film works as an intermediate layer to enhance the adhesion between the SiNx and Pt films. The Pt film is patterned to the designed feature using an Autostep i-line stepper and the unprotected part is etched away by ion milling (**Figure 2.2(d)**). After stripping the photoresist, a 250 nm thick LTO film is coated on top of the Pt film by plasma enhanced chemical vapor deposition (PECVD), and etched to cover the serpentine Pt by reactive ion etching (RIE) (**Figure 2.2(e)**). The SiNx layer is patterned and RIE etched to expose the silicon (**Figure 2.2(f)**). Without the SiNx protection, the exposed silicon

substrate is etched away by 10% tetramethylammonium hydroxide (TMAH) to make the two SiNx membranes suspended (**Figure 2.2(g)**).

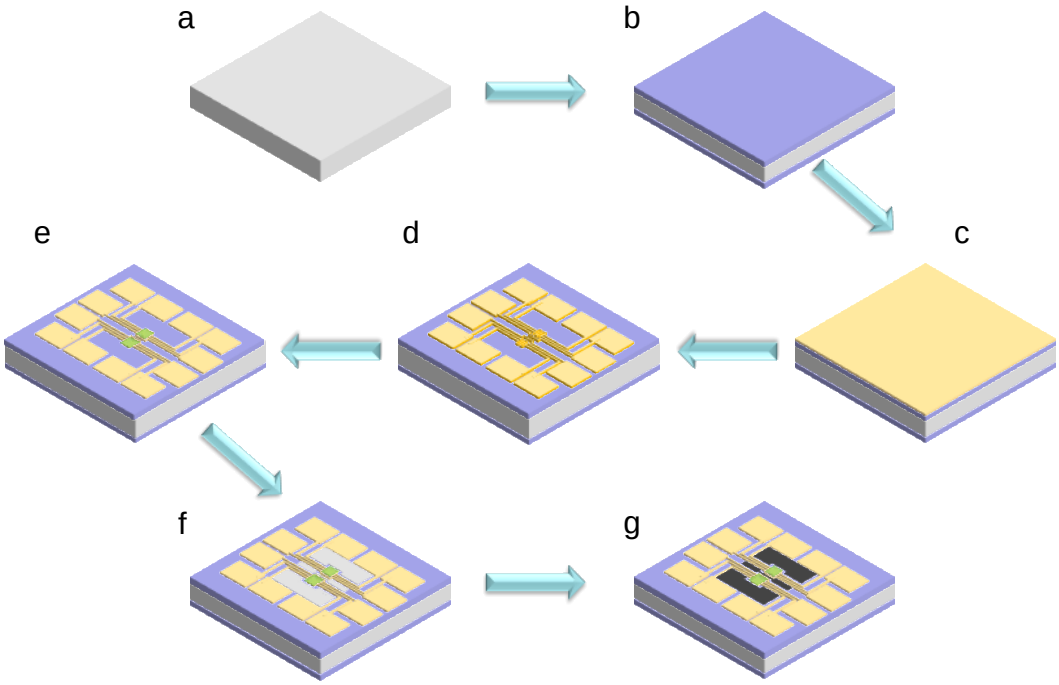


**Figure 2.2** Schematic diagram of the fabrication process. (a) Bare silicon wafer. (b) LPCVD deposition of 0.5 μm SiNx films on both sides of the silicon wafer. (c) Sputtering deposition of a 5 nm Cr and 30 nm Pt layers on one side of SiNx film. (d) Patterning and ion milling Pt layer to the design feature. (e) Patterning and RIE etching a 250 nm thick LTO film which is deposited by PECVD. (f) Patterning and RIE etching the SiNx layer to expose the silicon substrate. (g) Wet etching the exposed silicon substrate by TMAH to suspend the SiNx membranes and beams.

## 2.3 Sample Preparation

Other than integrating nanostructure across the two suspended membranes during fabricating the microdevice (Lee et al. 2017; Lim et al. 2016), two ways have been developed to deliver a nanowire sample to bridge the two membranes. One way is to drop cast sample suspension solution onto several microdevices. After drying the solvent, an individual nanowire can be found by chance to bridge the two suspended membranes of a microdevice. However, this method requires highly concentrated sample suspension and plenty of devices for drop casting, as well as time-consuming efforts to examine multiple devices to find an individual wire across the two suspended

membranes. To save time and devices, an in-house assembled micromanipulator mounted with a sharp tungsten probe with a tip radius of ~0.1 μm (The Micromanipulator Co. model 7X), as shown in **Figure 2.3**, is applied to pick up individual nanowires and place them to desired locations. In doing so, we first drop cast a small amount of samples on a substrate. Polydimethylsiloxane (PDMS) is often chosen as the substrate because it is soft and flexible that reduces the risk of damaging the sharp tip and sample. After the alcohol solvent is evaporated, individual samples can be easily found on the PDMS. In addition to the ultrasonic sonication, stamping is another way to transfer the samples from the substrate (usually silicon wafer) to the PDMS surface. For some quasi-1D samples, mechanical exfoliation with two pieces of PDMS can also be used to achieve individual nanowires.

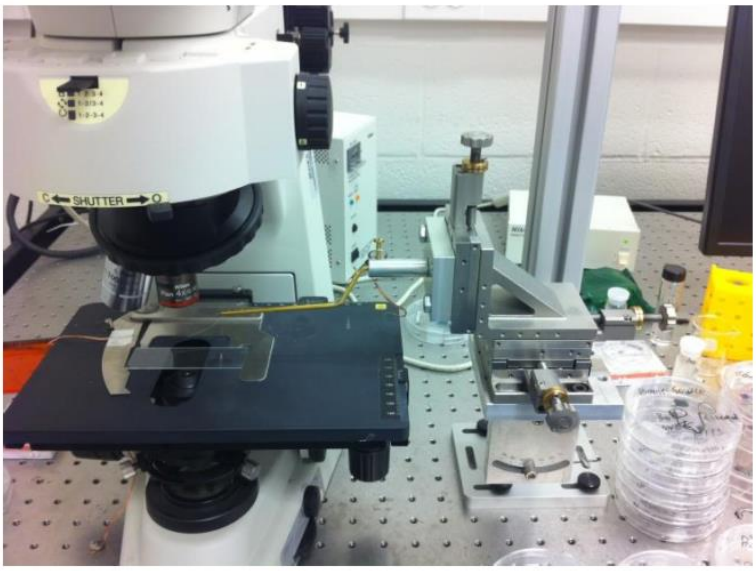


**Figure 2.3** A photograph of an in-house assembled micromanipulator mounted with a sharp tungsten probe (The Micromanipulator Co. model 7X) underneath an optical microscope (Nikon ECLIPSE 50 i) applied for individual sample placement

After samples are transferred onto the PDMS substrate, an individual sample can be picked up and placed onto the suspended microdevice through manipulating the tungsten tip under an optical microscope (Nikon ECLIPSE 50 i) with a 100×, long working distance (6.5 mm) objective

lens. **Figure 2.4** shows a silver nanowire located across the two suspended membranes with a 36 μm gap distance.

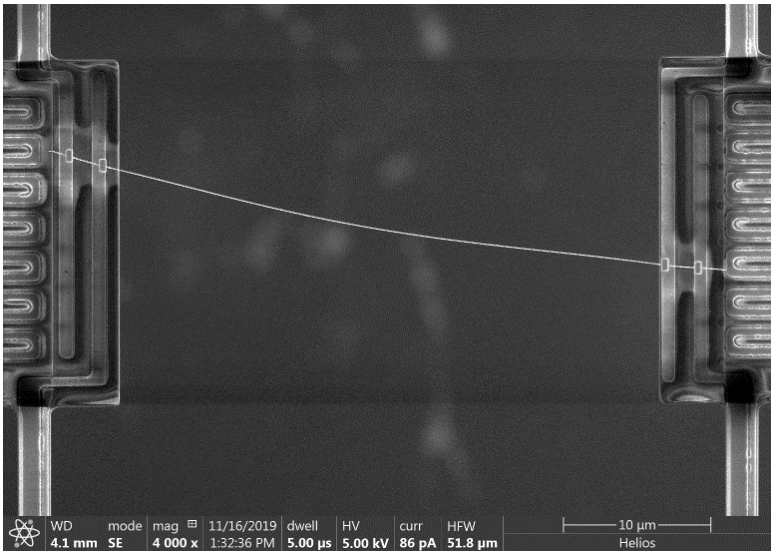


**Figure 2.4** SEM micrograph of an individual silver nanowire bridging two suspended membranes with a 36 μm gap distance. Pt/C depositions are used to enhance thermal and electrical contact between the nanowire and electrodes.

To achieve good electrical and thermal contact between the nanowire and the Pt electrodes, electron beam induced deposition (EBID) is often used to locally deposit Pt/C at the nanowire-suspended membrane contact. For nanowires with a thin native amorphous layer on the surface, focused electron/ion beam induced etching can be used to remove the electrically insulating amorphous layer before EBID deposition of Pt/C. Alternatively, $BCl_3$ plasma etching can be applied to etch away the native oxide layer for ohmic electrical contact (Weathers and Shi 2013).

Unlike the four-point method which enables to achieve the intrinsic electrical resistance of the measured sample, the thermal contact resistance between the sample and the membranes can significantly affect the measured thermal conductance if it is not negligible as compared to the intrinsic thermal resistance of the sample. Thus, it is crucial to reduce the wire-membrane contact thermal resistance. Yang et al. has demonstrated that the thermal conductivity of a bundle of boron

nanoribbons can be enhanced by wetting the van Der Waals (vdW) interface between the nanoribbons (Yang et al. 2012). The theoretical calculation yields a value of 320 mJ/m$^2$ for the adhesion energy between two boron nanoribbons after the wetting process, which is much higher than typical adhesion energy of vdW interactions (<100 mJ/m$^2$) and comparable to that between multiple layer graphene and silicon oxide (310 mJ/m$^2$). The wetting method has also been proven to work to enhance the thermal conductivity of double silicon nanoribbons (Yang et al. 2017). Motivated by the above studies, prior to EBID, a small amount of reagent alcohol is dropped onto the membranes to cover the part of the sample on the membrane. As shown in **Figure 2.5**, the alcohol can spread into the interface between the nanowire and the membrane. The alcohol evaporation process helps to make an intimate contact and thus reduces the contact thermal resistance between the sample and the membranes.

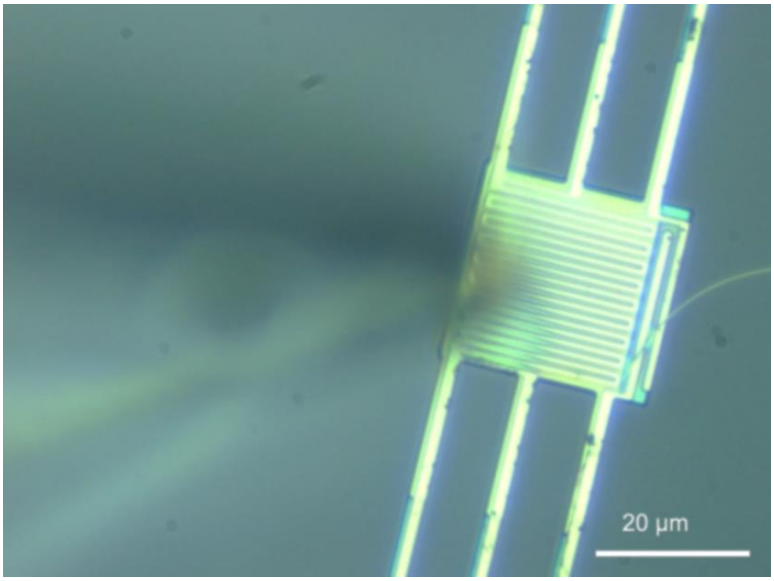


**Figure 2.5** Wetting process. A small amount of alcohol is dropped onto the membrane and spreads to the interface between the nanowire and the membrane.

## 2.4 Measurement Setup

**Figure 2.6** shows a schematic diagram of the experimental setup for thermal conductance measurement. The suspended measurement device with a nanowire sample and the corresponding reference device are mounted within a ceramic dual in-line package (DIP) and placed in a cryostat (Janis CCS-450). The vacuum level of the chamber is lowered to less than $10^{-6}$ Torr using a turbomolecular pump (Edwards E2M1.5) and the local temperature of the DIP is controlled by a temperature controller (Lakeshore 335). A data acquisition (DAQ) board (National Instruments PCI-6052e) is used to collect the measurement data and provide a direct current (DC) for Joule heat generation on the heating membrane. At the heating side, a sinusoidal alternating current (AC) signal from the lock-in amplifier is coupled with the DC heating current by an integrated differential amplifier (Analog Devices SSM2141). A resistor of 505 kΩ, which is much larger than the electrical resistance of the PRT, is connected to the heating side circuit to achieve a constant current heating source under each designated DC heating voltage. The Joule heat can pass through sample to increase the temperature on the sensing side. The temperature rises at both heating and sensing sides lead to the changes of AC output voltage, which can be monitored using lock-in amplifiers (Stanford Research SR850). The DC current at the heating side is measured by a high accuracy current preamplifier (DL Instruments Model 1121). A reference device situates aside the measurement device within ~5 mm distance, which minimizes the effects of temperature variation over the area of the DIP. At the sensing side, the sensing and reference PRTs are respectively connected to a precision resistor (Extech 380400) sitting in ambient condition to form a Wheatstone bridge.

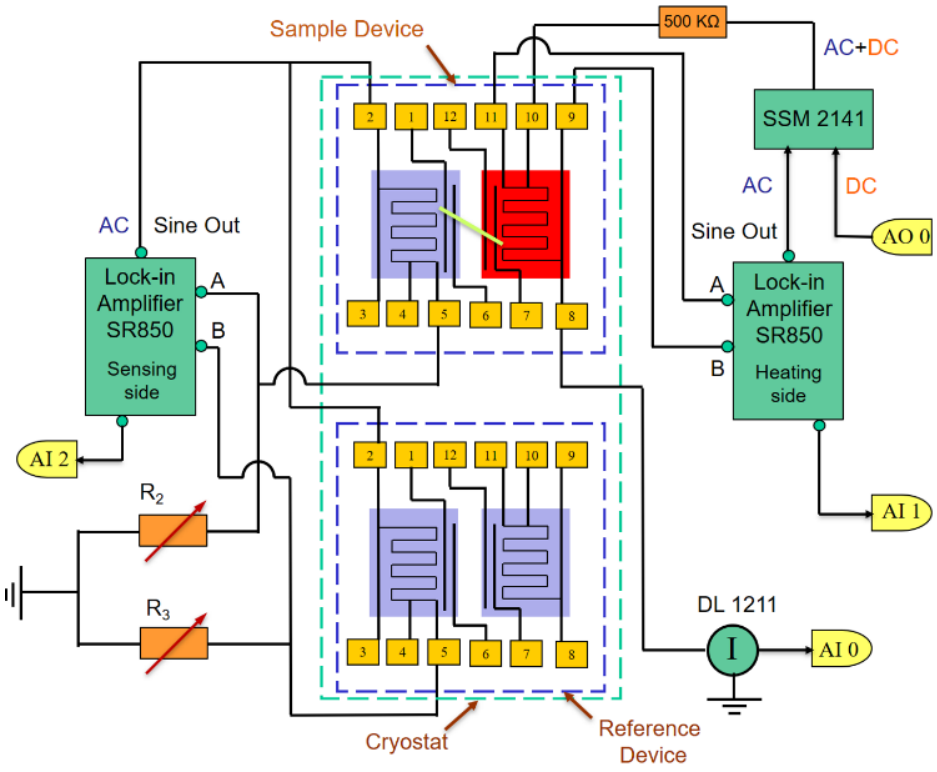


**Figure 2.6** Schematic diagram of the measurement setup.

The thermal circuit of the common mode rejection scheme is shown in **Figure 2.7**. As the DC current ($I$) pass through the heating circuit, a certain amount of Joule heat is generated at the serpentine Pt coil ($Q_h = I^2R_h$) and the two Pt leads that carry the DC current to the heating PRT ($2Q_L = 2I^2R_L$), where $R_h$ and $R_L$ are the electrical resistance of the PRT and each Pt lead. A certain amount of heat on the heating membranes ($Q_h$) is transferred to the sensing side through the sample between the heating and sensing membranes ($Q_2$), which is further transferred to the silicon substrate through the supporting beams. As the internal thermal resistance of each membrane is much smaller than that of its six long narrow supporting beams that thermally connect the membrane to the silicon substrate at the environment temperature $T_0$, it is reasonable to assume that the temperature of the suspended membrane is uniform, which is $T_h$ for the heating side and $T_s$ for the sensing side (Moore and Shi 2011). In high vacuum and with a small $\Delta T_h$ ($\Delta T_h = T_h - T_0$

< 5 K), the background heat transfer between the heating and sensing membranes by residual air conduction/convection is negligible compared to $Q_2$. The heat conducted to the silicon substrate through the six supporting beams at the heating side is calculated as $Q_1 = Q_h + 2Q_L - Q_2$.

The supporting beams are designed to be identical and fabricated under the same condition, so it is reasonable to assume that they have the same dimension and thermal conductivity ($\kappa_b$). If the heat loss through radiation and air conduction/convection is negligible as compared to the heat conduction through the beams, the total thermal conductance of the six beams at the sensing side can be described as $G_b = 6\kappa_b A/L$, where $A$ and $L$ are the cross-sectional area and length of each beam, respectively. Following the thermal circuit in **Figure 2.7**,

$$Q_2 = G_b \Delta T_s = G_s(T_h - T_s), \tag{2.1}$$

where $\Delta T_s = T_s - T_0$ is the temperature rise of the sensing membrane and $G_s$ is the thermal conductance of the sample. The inverse of $G_s$, that is, $R_{sample}$, consists of both the intrinsic thermal resistance of the sample ($R_i$) and the contact thermal resistance between the sample and the membranes ($R_c$), which is

$$R_{sample} = R_i + R_c. \tag{2.2}$$

Here $R_i = \frac{L_n}{\kappa_n A_n}$, where $\kappa_n$, $A_n$ and $L_n$ are the intrinsic thermal conductivity, cross-sectional area, and suspended length of the sample between the two membranes, respectively. Since the temperature rise at the heating side ($\Delta T_h$) is controlled to be small (~5 K), the thermal conductance $G_s$, $G_b$ and $G_c$ (1/ $R_c$) are expected to be approximately constant during the Joule heating process.

Based on the thermal circuit, $G_b$ and $G_s$ can be further expressed as a function of the temperature rises at both the heating and sensing sides and the total Joule heat generated at the heating Pt coil and current-carrying beams, as

$$G_b = \frac{Q_h + Q_L}{\Delta T_h + \Delta T_s}, \tag{2.3}$$

and

$$G_s = G_b \frac{\Delta T_s}{\Delta T_h - \Delta T_s}. \tag{2.4}$$

$Q_h$ and $Q_L$ can be calculated from the current and the voltage drops across the heating PRT and two Pt leads. $\Delta T_h$ and $\Delta T_s$ are derived from the measured resistance change of the heating and sensing PRTs and the temperature coefficient of the Pt resistance (TCR=(d$R$/d$T$)/$R$), respectively.

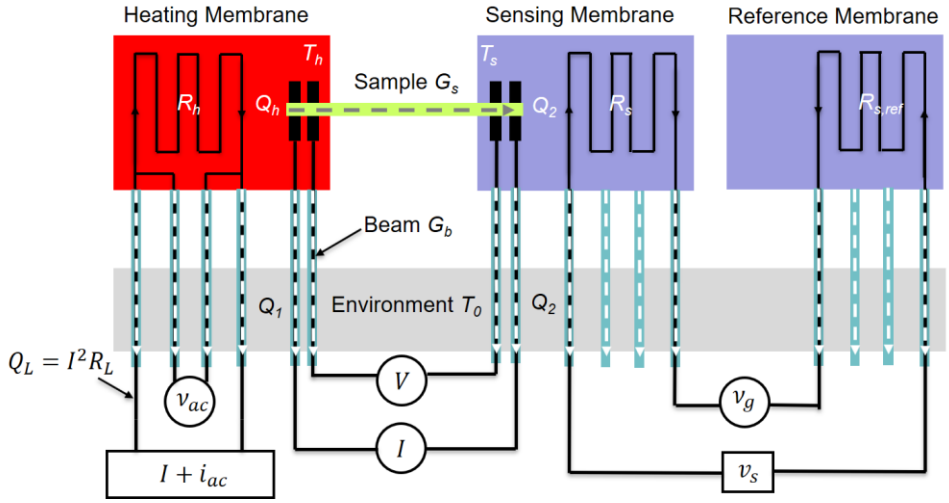


**Figure 2.7** Thermal circuit of the measurement scheme.

**Figure 2.8** shows the simplified electrical measurement circuit for both the heating and sensing sides. The electrical resistance of the heating PRT ($R_h$) is measured through four-point method using a sinusoidal current of ~300 nA and 1400 Hz. The first harmonic component of the voltage drop across the heating PRT ($v_{ac}$) is monitored by a lock-in amplifier, yielding $R_h = \frac{v_{ac}}{i_{ac}}$. Then the temperature rise of the heating membrane can be detected by measuring the resistance change of the heating PRT with the sweeping DC heating current, which is calculated as

$$\Delta T_h(I) = \frac{R_h(I) - R(0)}{\frac{dR_h}{dT}}. \tag{2.5}$$

The temperature rise of the sensing membrane is obtained from the output voltage of the Wheatstone bridge circuit. The bridge circuit consists of the resistor at the sensing side $R_s$, the reference resistor $R_{s,ref}$, and two additional precision resistors $R_2$ and $R_3$, which are connected in parallel as shown in **Figure 2.8**. A lock-in amplifier is applied to supply the source voltage ($v_s$) and simultaneously monitor the bridge output voltage ($v_g$). The relationship between $v_s$ and $v_g$ is

$$\mathrm{v}_g = \mathrm{v}_A - \mathrm{v}_B = \left(\frac{R_2}{R_s+R_2} - \frac{R_3}{R_{s,ref}+R_3}\right)\mathrm{v}_s. \tag{2.6}$$

By rearranging Eq. (2.6), the electrical resistance of the sensing side is expressed as

$$R_s = \frac{R_2}{\left(\frac{R_3}{R_{s,ref}+R_3}+\frac{v_g}{\mathrm{v}_s}\right)} - R_2. \tag{2.7}$$

Different from $R_h$ which is directly measured using the four-point method, the electrical resistance at the sensing side includes the resistance of the sensing PRT ($R_c$) and the resistance of two Pt leads ($2R_L$). As the temperature is uniform over the sensing membranes but varies linearly from $T_s$ to $T_0$ along the two supporting beams, the total resistance of the sensing side is

$$R_s + \Delta R_s = 2\left[R_L + \frac{dR_L}{dT}\left(\frac{T_s-T_0}{2}\right)\right] + R_c + \frac{dR_c}{dT}(T_s - T_0), \tag{2.8}$$

where $\Delta R_s$ is the temperature-induced resistance change of the sensing side and can be expressed as

$$\Delta R_s = \left(\frac{dR_L}{dT} + \frac{dR_c}{dT}\right)(T_s - T_0). \tag{2.9}$$

From Eq. (2.9), the resistance change of the sensing side is regarded as the result of a uniform temperature rise over the membrane and one single supporting beam. Thus, an effective resistance change per temperature difference can be defined as

$$\frac{dR_{s,eff}}{dT} = \left(\frac{R_L+R_c}{2R_L+R_c}\right)\frac{dR_s}{dT}. \tag{2.10}$$

The temperature rise of the sensing side is achieved as $\Delta T_s = \frac{\Delta R_s}{\frac{dR_{s,eff}}{dT}}$.

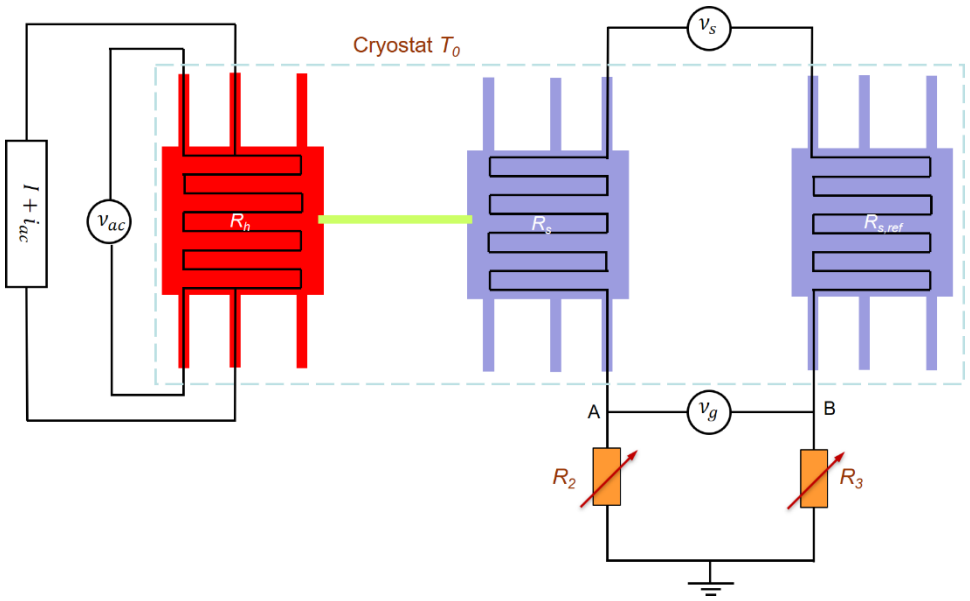


**Figure 2.8** Simplified electrical measurement circuit for both the heating and sensing sides.

**Figure 2.9** shows the schematic diagram of the measurement circuit for thermoelectric properties (electrical conductivity and Seebeck coefficient). The four electrodes on the SiNx membranes enable four-point electrical measurement, which essentially eliminates the contact electrical resistance between the sample and the Pt electrodes (Long et al. 2010). For samples of very large electrical resistance (>1 MΩ), as the input impedance of the voltage amplifier (SR560) is around 100 MΩ, the current passing through the voltage amplifier is non-negligible, which leads to a lower measured resistance than its actual value. To avoid the inaccurate measurement, an instrumentation amplifier (Texas Instruments INA110) with an extremely large input impedance (>1 GΩ) is connected into the circuit (Werheit et al. 2009). Using the two inner Pt electrodes, the Seebeck coefficient can be achieved from the measured temperature-induced voltage difference as a function of temperature gradient between two SiNx membranes, i.e., $V_{TE} = (S_S - S_{pt})(T_h - T_s)$ (Mavrokefalos et al. 2007; Werheit et al. 2009).

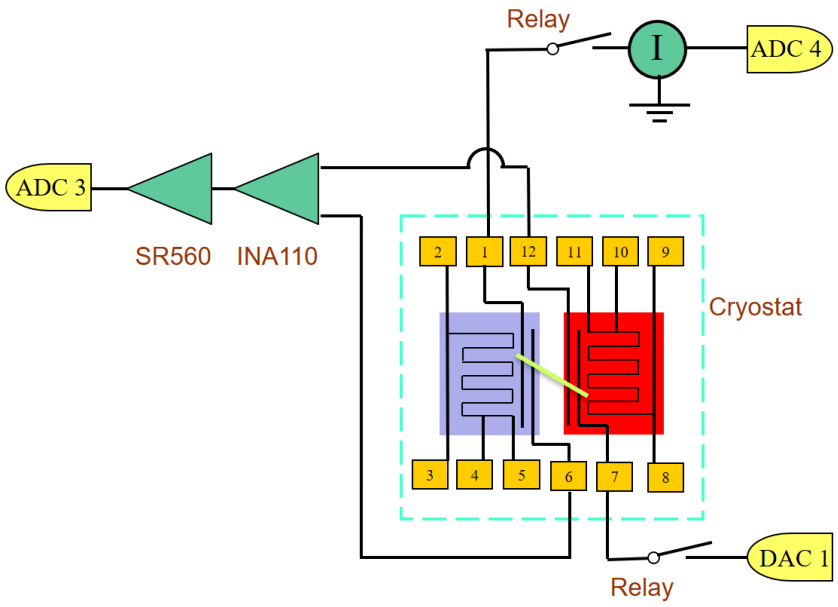


**Figure 2.9** Schematic diagram of Seebeck coefficient and four-point electrical resistance measurement setup.

### 2.5 Effects of Radiation Shields

An assumption adopted in the heat transfer model of the experimental setup is that all dissipated Joule heat is transferred to the environment through the supporting beams without radiation heat transfer. This assumption has been examined through modeling the temperature distribution while considering the non-negligible radiation heat loss using finite element analysis. The results reveal that the non-negligible radiation heat transfer from the membranes and long supporting beams to the surroundings can lead to a temperature difference up to tens of Kelvin at 800 K (Moore and Shi 2011). According to the model, the temperature profiles along the long supporting beams become non-linear when the stage temperature is significantly higher or lower than the room temperature. Although the non-linear temperature distribution does not necessarily cause incorrect measurements, it will result in errors in the measured TCR of the Pt thermometers, which further affects the derived thermal conductance of the beam and sample. To fix this issue, they suggest that the significant radiation heat loss can be essentially eliminated by adding an extra

radiation shield onto the sample holder that ideally shares the same temperature with the sample holder. This method is also discussed in other work (Lee et al. 2016; Zheng et al. 2013).

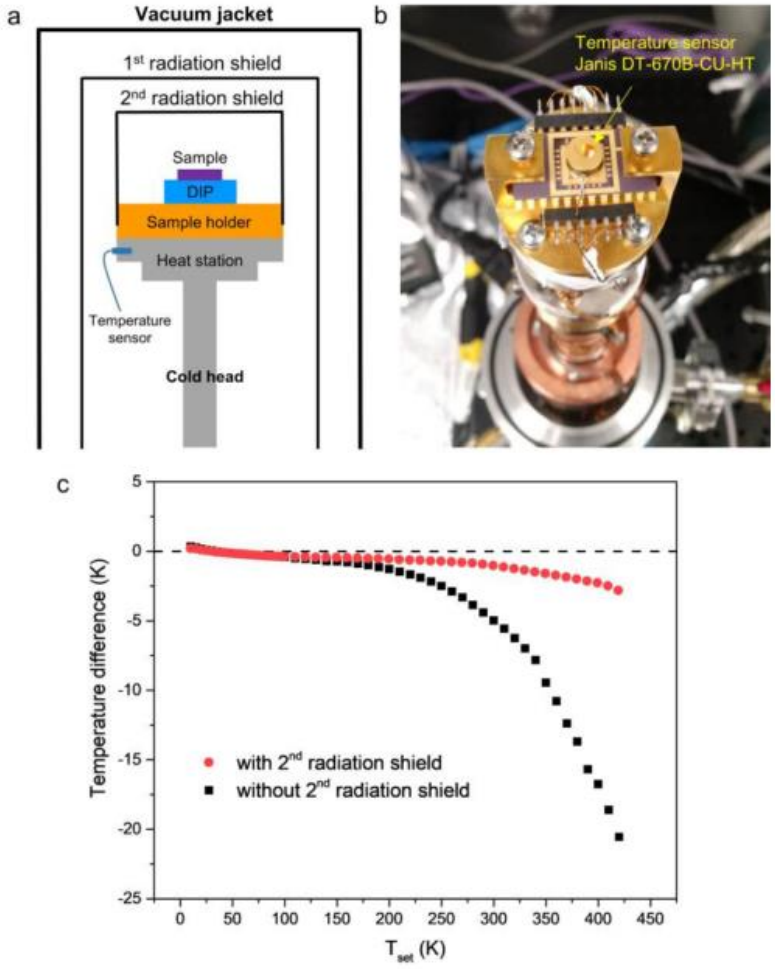


**Figure 2.10** Effects of the inner radiation shield (Yang 2019). (a) Schematic drawing showing the inside of the cryostat. (b) A picture showing the approach of mounting an additional thermal sensor on the DIP. (c) Temperature difference between the measured local temperature and the setting temperature with and without the inner radiation shield mounted on the sample holder.

**Figure 2.10(a)** shows the locations of the sample and shields used in the measurement setup. To check the effectiveness of the additional shield, a calibrated silicon diode sensor (Janis DT-670B-CU-HT with accuracy of ± 0.1 K) is mounted onto the DIP to measure the local temperature of the DIP with and without the second radiation shield, as shown in **Figure 2.10(b).** The

temperature difference between the measured temperature ($T_{DIP}$) and the setting temperature ($T_{set}$) is plotted in **Figure 2.10(c)**. The temperature difference measured with the second radiation shield is much smaller than that only with the one shield, which confirms that the second radiation shield helps to maintain the local temperature of the DIP closely to the set temperature.

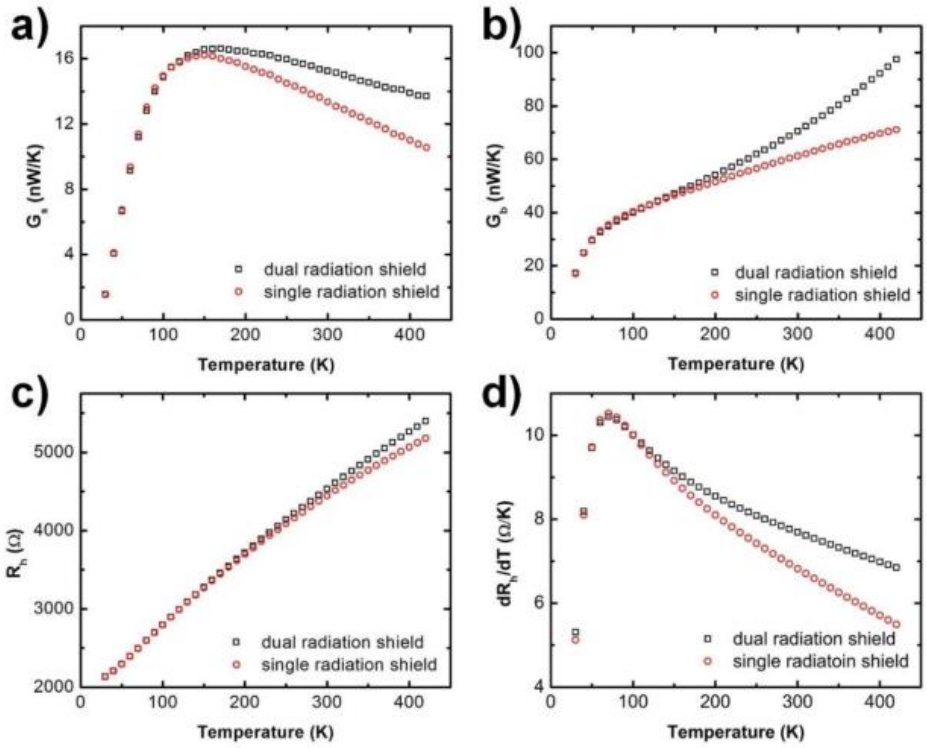


**Figure 2.11** Comparison of measured quantities using single and dual radiation shield set-ups (Yang et al. 2016; Zhang 2017). (a) Thermal conductance of the silicon nanoribbon, (b) Thermal conductance of the supporting beams, (c) Resistance of PRT at the heating side, and (d) $dR_h/dT$

Then the thermal measurement on the same silicon nanoribbon with and without the second radiation shield has been conducted to examine the effect of the second radiation shield on the thermal conductance. Without the second radiation shield, the measured electrical resistance of the heating PRT at 420 K is 4.2% lower than that measured with the inner radiation shield. However, as discussed above, the errors in measured resistance can propagate into the derived thermal conductance of the beam and sample. The measured thermal conductance with and without the

second radiation shield is shown in **Figure 2.11**. The difference ramps up as the temperature increases and reaches to 23% at 420 K. Since the TCR of Pt thermometers is affected by the radiation shield, the derived temperature changes are quite significant at high temperatures, which leads to large errors in the extracted thermal conductance.

## 2.6 Background Thermal Conductance

The background thermal transport inevitably exists in the thermal bridge measurement, including the residual air conduction/convection and radiation heat transfer. Zheng et al. have demonstrated that the background thermal conductance only increases marginally as the vacuum level increases from $10^{-6}$ mbar to $10^{-4}$ mbar (Zheng et al. 2013), which indicates that the residual air conduction/convection can be negligible. Generally, as the temperature difference between heating and sensing membranes is controlled to be small ($\Delta T_h$-$\Delta T_s$ < 5 K), the background thermal conductance can be neglected for samples with relatively large thermal conductance ($G_s$). However, as the sample thermal conductance is on the same order of magnitude as the background thermal conductance ($G_{bg}$), the background heat transfer should be considered.

### 2.6.1 Effects of Background Thermal Conductance

To examine the effects of background thermal conductance between heating and sensing membranes, we measured the thermal conductance of a blank device with and without a sample bridging the heating and sensing membranes and obtained the intrinsic thermal conductance of the sample ($G_{NW}$) by subtracting the background thermal conductance ($G_{bg}$) from the total measured thermal conductance ($G_{total}$). **Figure 2.12** shows the thermal conductance of a $Ta_2NiSe_5$ nanowire with a hydraulic diameter of 32 nm and a suspended length of 6 μm. At low temperatures (< ~100 K), as the background thermal conductance is extremely small compared to the thermal conductance of the nanowire, the measured total thermal conductance overlaps with the intrinsic

thermal conductance of the nanowire. However, as the temperature increases, the background thermal conductance ramps up quickly following the $T^4$ law and at 350 K the background thermal conductance (~470 pW/k) is almost half of the thermal conductance of the sample (~920 pW/K). In this case, the measured total thermal conductance at high temperatures cannot reflect the real temperature dependence and values of the thermal conductance of the nanowire.

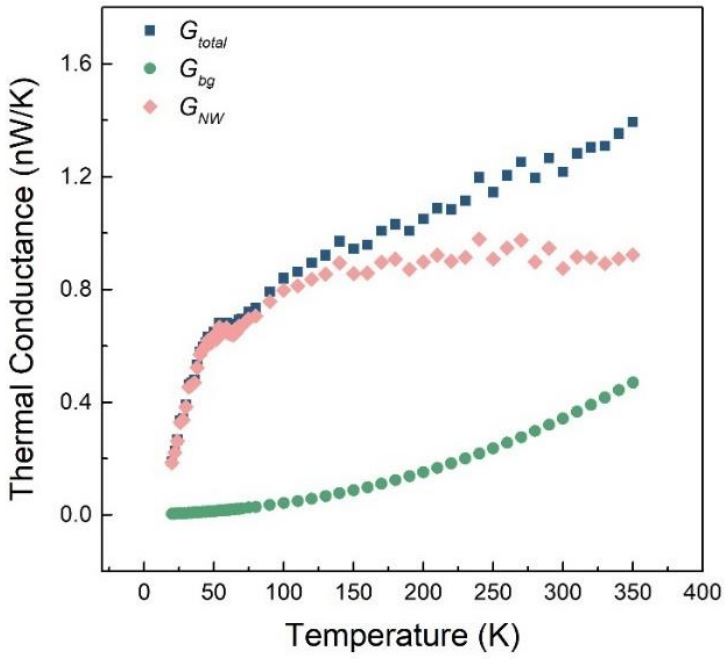


**Figure 2.12** Measured total thermal conductance ($G_{total}$), background thermal conductance ($G_{bg}$), and calculated thermal conductance of a $Ta_2NiSe_5$ nanowire ($G_{NW}$) by ruling out the $G_{bg}$.

Since the devices fabricated in a same batch generally share the same design and fabrication process, it is reasonable to assume that all devices with the same gap distance have approximately the same background thermal conductance. We fit the measured thermal conductance of a blank device with $4^{th}$ order polynomial function of temperature and regard it as the background thermal conductance for that batch of devices with the same gap distance.

### 2.6.2 Rejection Mode

Another way of rejecting the background heat signal is to apply the same heating current on the heating PRT of the reference device (Zheng et al. 2013). The schematic diagram of the rejection mode is shown in **Figure 2.13**. As the heating PRT of the reference device is coupled into the DC heating circuit at the heating side, the temperature difference between the heating and sensing membranes induced by the background heat transfer ($\Delta T_{bg}$) is almost same for both the sample and the reference devices, with the assumption that the design and fabrication of the devices are identical. The output voltage change of the Wheatstone bridge monitors the different temperature rises between the two sensing membranes that only reflects the change caused by the heat conduction through the sample in the sample device.

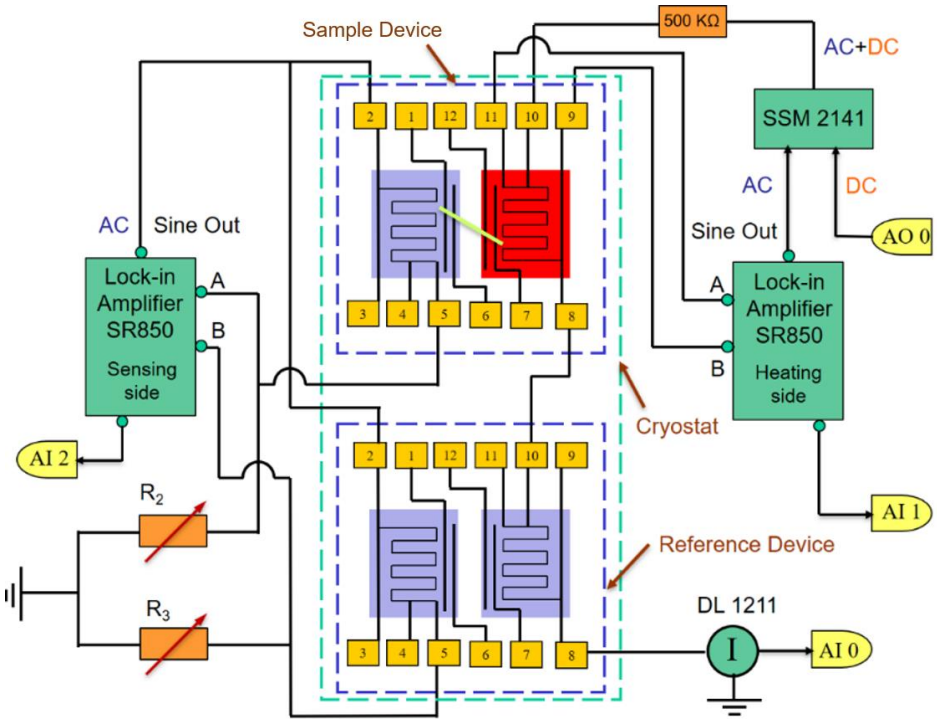


**Figure 2.13** Schematic diagram for the thermal measurement setup with the background signal rejection mode. The heating current passes through the heating PRT of the sample and reference devices simultaneously to create the basically same temperature rise, which ultimately are balanced out in the Wheatstone bridge method.

### 2.6.3 Three-Membrane Device

Although the methods of directly measuring the background thermal conductance and rejecting background heating signal can effectively help to achieve more accurate thermal conductance of samples, the background heat radiation can still affect the measured results for the samples with extremely small thermal conductance due to the variations in device fabrication process. To eliminate the background thermal conductance, we design a three-membrane device which contains a heating membrane in the middle and sensing/reference device at the side with the same gap distance. As shown in **Figure 2.14**, during the measurement, the sensing and reference membranes receive the same radiative heat from the heating membrane; with the Wheatstone bridge connected into the sensing and reference sides, the background thermal conductance can be effectively cancelled out.

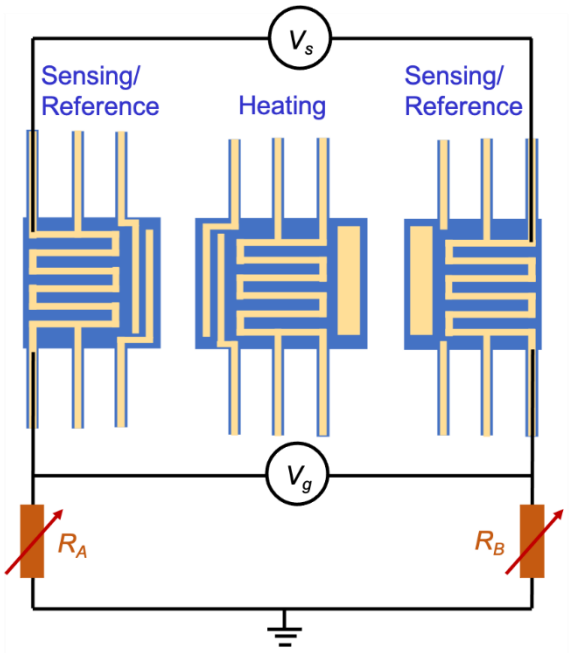


**Figure 2.14** Three-membrane device. The heating membrane is in the middle and the sensing and reference membranes are at the side with the same distance from the heating membrane. During the thermal measurement, the sensing and reference device can receive the same thermal radiation from the heating membrane and the radiative heat can be cancelled out with the common mode rejection.

## 2.7 Summary

In this chapter, we discussed in details the experimental measurement approach including the device fabrication, sample preparation, experimental setup and data analysis. To reduce the wire-membrane contact effect, we developed a wetting process in which the evaporation of alcohol can make an intimate contact between the nanowire sample and the membranes. For samples with extremely low thermal conductance, the background heat transfer can considerably affect the temperature dependence and values of the measured thermal conductance, especially at high temperatures. To eliminate the effect of background thermal conductance, we design a three-membrane device which contains a heating membrane in the middle and sensing/reference devices at the side with the same gap distance. With the common mode rejection scheme, the effect of background thermal conductance can be effectively neglected during the thermal measurement. The improved experimental setup has significantly enhanced measurement sensitivity, which allows for precise thermal measurements.

# Chapter 3

## Electrical and Thermal Transport through Silvers Nanowires and Their Contacts

Silver nanowires, owing to their excellent electrical, thermal and optoelectronic properties, are finding more and more applications as nanofillers for composites that are essential components in flexible electronic, optoelectronic, and energy conversion devices, as well as thermal interface materials (Cho et al. 2017; Hsu et al. 2015; Kang et al. 2015; Yu et al. 2011). So far, there have been several reports on the electrical and thermal transport properties of silver nanowires (Cheng et al. 2015; He et al. 2018; Kojda et al. 2015; Wang et al. 2018). However, the reported studies are often based on very limited samples and the results are not consistent with each other; and therefore, it is important to conduct systematic studies to obtain consistent trends of transport properties as a function of nanowire size. More interestingly, elastic stiffening is observed for the silver nanowires with diameters below ~100 nm (Chang et al. 2016; Cuenot et al. 2004; Jing et al. 2006). Recently, it has been shown that for silicon nanowires of diameters less than 30 nm, elastic/acoustic softening is responsible for the observed thermal conductivity reduction beyond the prediction based on the classical size effect (Wingert et al. 2015; Yang et al. 2016). It follows to ask whether and how elastic stiffening alters the electrical and thermal transport in thin silver nanowires of less than 100 nm in diameter.

One more consideration for silver nanowires is that as nanofillers, electrical and thermal contact resistance between wires are critically important for the overall properties of the resulting composites; however, no direct experimental data have been reported on the resistance at these nanoscale contacts so far. Moreover, the confinement effects at point contacts can significantly alter transport behaviors of charge and energy carriers. Previous studies have shown that the W-F law is applicable to metal interfaces (Wilson and Cahill 2012) and gold atomic junctions (Cui et

al. 2017; Mosso et al. 2017) with marginal phonon contribution at room temperature. Motivated by these remarkable experiments, theoretical studies were also performed to investigate the Lorenz number of various metal atomic contacts and suggested that phonons could contribute up to 40% of the thermal conductance for aluminum atomic contacts at room temperature because of its high Debye energy (Klöckner et al. 2017). Despite these great efforts, how confinement alters the effective Lorenz number at contacts with a characteristic size between these two extreme regimes has not been well explored. In this context, the point contact between metal nanowires, which has a typical characteristic size of a few nanometers, provides an ideal sample set for study.

In this chapter, we report on systematic measurements to explore electrical and thermal transport properties of silver nanowires with diameters ranging from 38 to 84 nm, which allows for examination of the effects of elastic stiffening on the transport properties. Importantly, we also extract previously unavailable data on the contact resistance between individual silver nanowires. We demonstrated that silver nanowires could be more effective nanofillers to enhance thermal performance of nanocomposites. Moreover, with the measured electrical and thermal resistance of the point contact between silver nanowires, we present much enhanced and non-monotonic effective contact Lorenz number that comes from the non-negligible phonon contribution. These results could provide much insight into understanding the transport properties of silver nanowire-based composite materials.

### 3.1 Sample Preparation and Characterization

Silver nanowires suspended in isopropyl alcohol (IPA) with a concentration of 5 mg/mL. A drop of silver nanowires with IPA was diluted with reagent alcohol and sonicated for 20 seconds to obtain a uniform dispersion. The nanowire suspension was then casted onto a piece of PDMS. After the solvent evaporated, an individual nanowire was picked up by a sharp probe mounted on

an in-house built micromanipulator, transferred to a measurement device, and placed between the two side-by-side suspended membranes. A small amount of reagent alcohol was dropped onto the membranes to cover the parts of the nanowire, and the alcohol evaporation process helped to make an intimate contact between the nanowire and membranes to reduce the contact thermal resistance (Yang et al. 2012, 2017). Then, electron beam induced deposition was employed to locally deposit Pt/C pads at the wire-suspended membrane contacts to further enhance the electrical and thermal contacts.

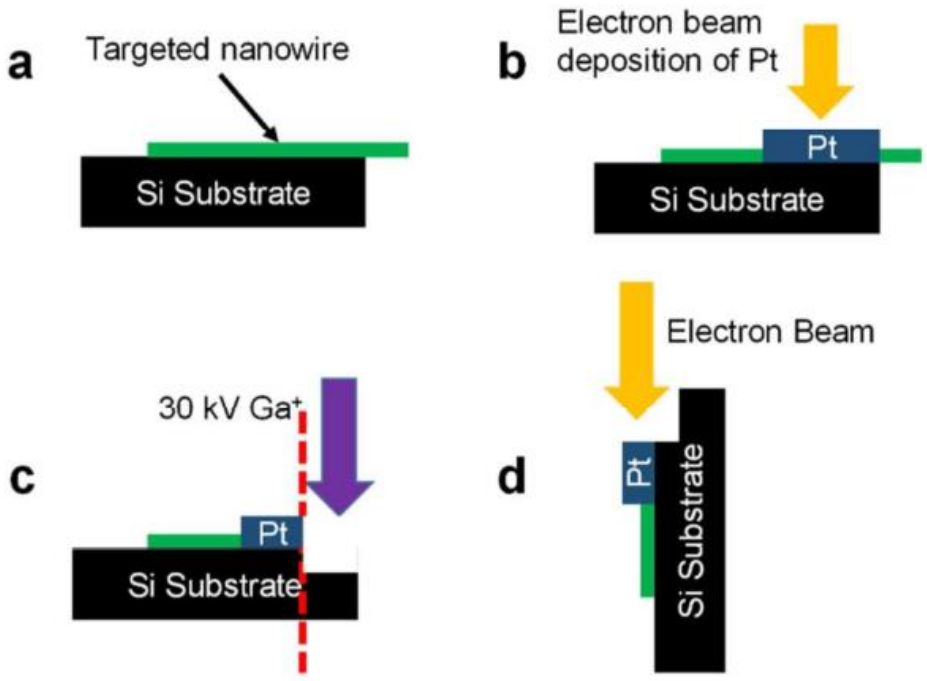


**Figure 3.1** Cross-section examination (Zhang et al. 2018). (a) An individual nanowire was placed on the edge of a silicon piece that has the edges well cut. (b) EBID of Pt/C was applied to cover the nanowire, preventing potential damage from the ion beam. (c) FIB was employed to remove part of the nanowire, exposing the cross section. (d) The silicon substrate was mounted vertically for direct SEM imaging of the cross section.

To characterize the cross section of silver nanowire, we follow the method used for $Ta_2Pd_3Se_8$ and $NbSe_3$ nanowires (Yang, Tao, et al. 2019; Zhang et al. 2018). As shown in **Figure 3.1**, after measurements the nanowire on the microdevice was picked up and placed on a piece of pre-cut

silicon substrate, which is perpendicular to the edge. Then the nanowire was covered and fixed with the Pt/C deposition. Focused ion beam (FIB) was applied to etch away part of the nanowire and expose the cross-section of the sample. At last, the silicon substrate with the etched nanowire was mounted vertically on a scanning electron microscopy (SEM) stub and loaded for direct visualization of the cross section.

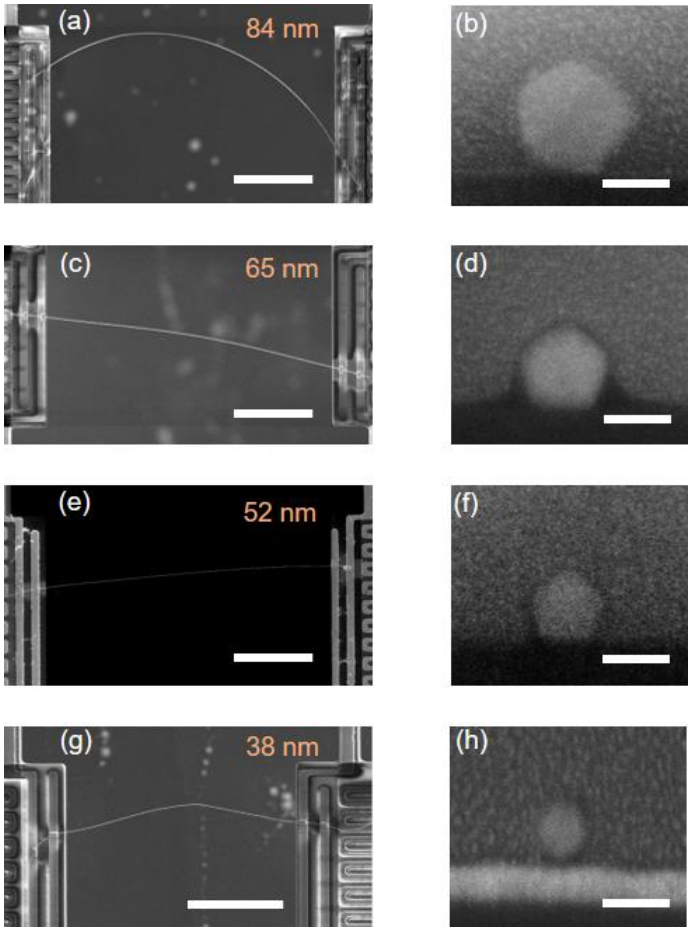


**Figure 3.2** SEM images of measured samples on the device and cross-sectional views of the samples. The cross section at the right side corresponds to the sample shown at the left side. The scale bar is 10 μm for the left side and 50 nm for the right side.

**Figure 3.2** shows the SEM micrographs (left panel) of the sample on the microdevice and cross-sectional images (right panel) for four silver nanowires. For nanowires with non-circular cross-sections, we have adopted the hydraulic diameter ($D_h = 4A/P$, where $A$ is the cross-sectional

area and *P* is the perimeter) to represent the wire characteristic size (Yang, Tao, et al. 2019; Zhang et al. 2018).

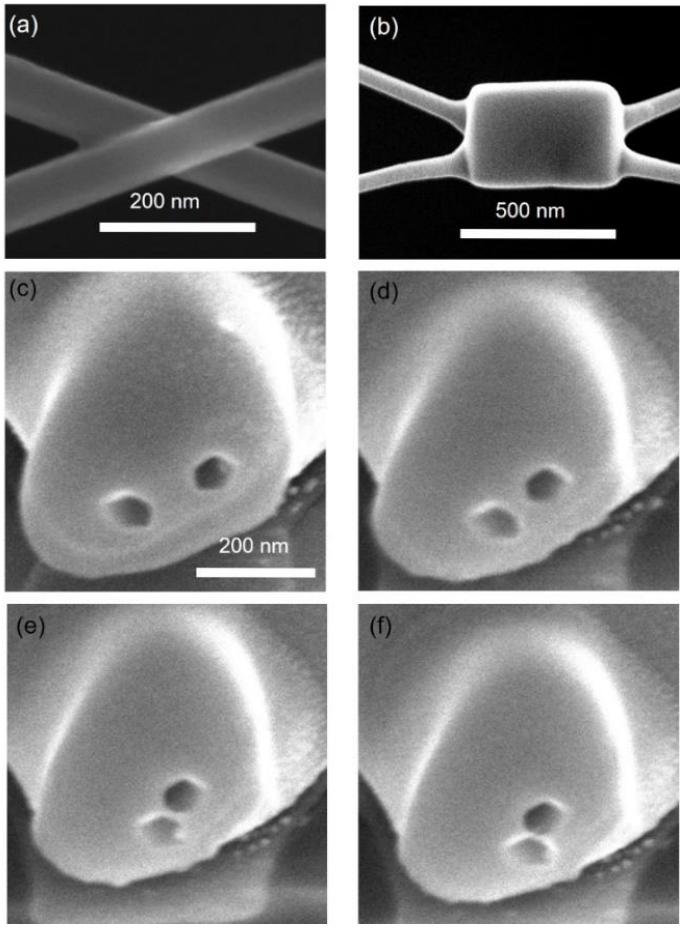


**Figure 3.3** Cross-sectional images of the contact between two silver nanowires (65 nm hydraulic diameter) that are etched away in air. The scale bar for (c)-(f) is the same.

The cross-section cutting method is also employed to examine the contact configuration between two silver nanowires. As for the contact silver nanowires in **Figure 3.3(a)**, we deposited Pt/C composite at the contact region as shown in **Figure 3.3(b)**. Then we transferred the contact to a piece of pre-cut silicon substrate for cross-section cutting with FIB. The process revealed the cross-sectional configuration, which was simultaneously examined by SEM with the tilted angle

of 52°. **Figure 3.3(c)-(f)** show the SEM images sequentially as the process proceeds to the junction of the two wires.

### 3.2 Wire-Membrane Contact Effect

For metal nanowires with high electrical and thermal conductivities, the measured conductance is very sensitive to the contact resistance between the nanowires and suspended membranes in our measurement devices. For electrical measurements we adopted the four-point method so the effects of contact electrical resistance could be effectively removed. However, for thermal measurements contact thermal resistance was still a concern even with EBID of Pt/C pads at the sample-suspended membrane contacts. Indeed, we found that even with Pt/C deposition, contact thermal resistance could still lead to lower effective thermal conductivity.

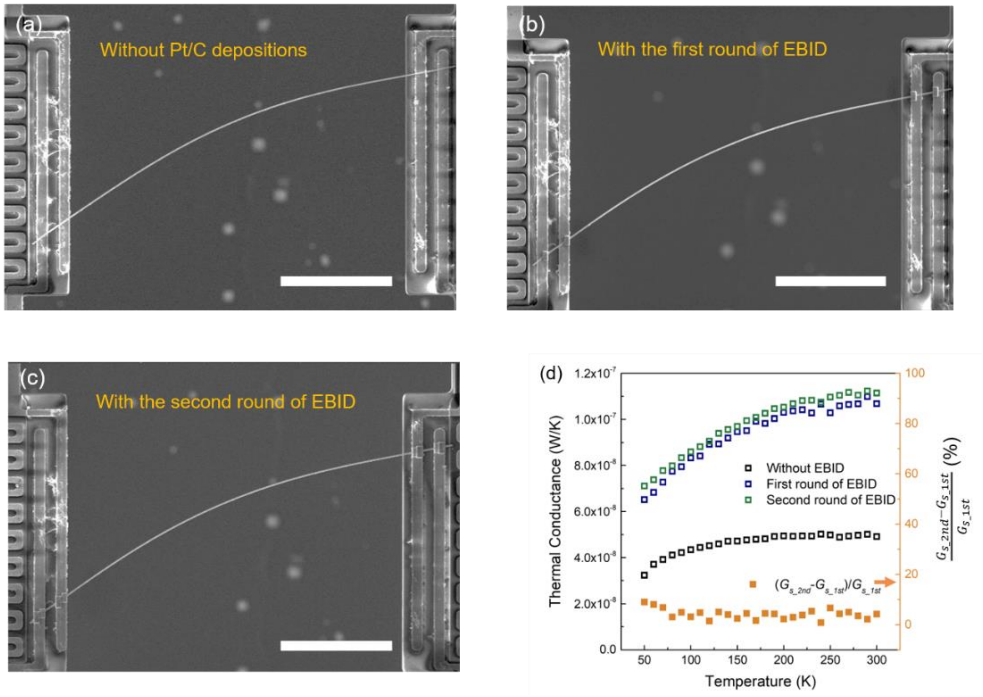


**Figure 3.4** Thermal conductance of a silver nanowire with an outer diameter of 125 nm and a suspended length of 33.7 μm. The SEM images of the sample (a) without Pt/C deposition, (b) with the first and (c) with the second round of EBID of Pt/C at the wire-membrane contacts. (d) The measured thermal conductance increases significantly after the first round of EBID, and still increases slightly after the second round of EBID. The enhancement after the second round of EBID is within 10%. The scale bar in (a), (b) and (c) is 10 μm.

We measured the thermal conductance of a silver nanowire with an outer diameter of 125 nm and a suspended length of 33.7 μm before and after depositing Pt/C pads. As show in **Figure 3.4(d)**, EBID can significantly reduce the contact thermal resistance between the nanowire and the suspended membranes; however, the thermal conductance still increases slightly (< 10%) after the second round of EBID, indicating that the contact thermal resistance does not drop to a negligible level. To minimize the effects of the contact thermal resistance, we wetted the contacts between the nanowire and suspended membranes with reagent alcohol, whose evaporation led to tight contacts at the wire-membrane junctions. In addition, we prepared wire samples with a long-suspended segment between the two suspended membranes to increase the weight of the intrinsic wire resistance in the total measured resistance. **Figure 3.5(a)** shows an SEM image of a silver nanowire which is taken after the second round of EBID. The wire has a suspended length ($L_s$) of 42 μm. The inset shows an SEM micrograph of the pentagonal cross-section. For the wire in **Figure 3.5(a)**, $D_h$ = 89 nm. **Figure 3.5(b)** plots the extracted thermal conductance *versus* temperature after the first and second round of EBID; and the overlapping values indicate that the contact thermal resistance becomes negligible as compared to the intrinsic thermal resistance of the nanowire (Hochbaum et al. 2008).

Based on a fin model (Bifano et al. 2012), the contact thermal resistance ($R_{CTR}$) with each membrane can be expressed as

$$R_{CTR} = \frac{1}{\sqrt{hP\kappa A}\tanh\left(L_{cm}\sqrt{\frac{hP}{\kappa A}}\right)}, \tag{3.1}$$

where $h$ is the heat transfer coefficient between the wire and membrane, $\kappa$ is the wire thermal conductivity, and $L_{cm}$ is the contact length which was kept approximately the same for each sample in our work. The fact that the second round of EBID does not alter the contact thermal resistance suggests that $R_{CTR}$ is independent of the contact length. In this case, $tanh\left(L_{cm}\sqrt{hP/\kappa A}\right) \approx 1$,

which also holds for smaller nanowires with lower $\kappa$ when $L_{cm}$ is unchanged. Thus, for nanowires with $D_h$ < 89 nm, $R_{CTR} = 1/\sqrt{hP\kappa A}$. The ratio of the contact thermal resistance to the intrinsic thermal resistance of the nanowire ($R_i = L_s/\kappa A$) is proportional to $(\kappa D_h)^{1/2}/L_s$, which is lower for smaller wires. Therefore, it is reasonable to assume that with EBID, the effects of contact thermal resistance become trivial for silver nanowires with $D_h$ < 90 nm and $L_s$ > 40 μm.

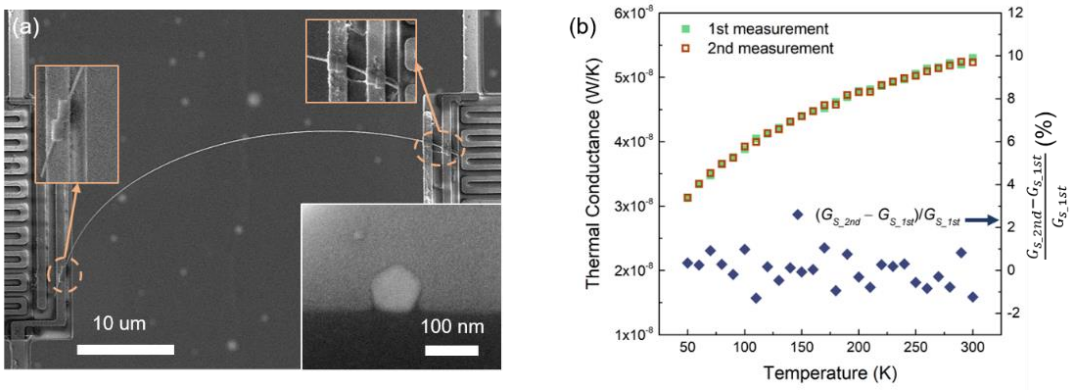


**Figure 3.5** Effects of contact thermal resistance. (a) SEM micrograph of a silver nanowire placed on a 36 μm-gap device with two rounds of EBID Pt/C at the wire-suspended membrane contacts. The inset shows the cross-section of the wire with $D_h$ = 89 nm. (b) Measured thermal conductance after the first and second round of EBID essentially overlaps (with < 2% difference).

### 3.3 Bending Effect

When manipulating the relatively long silver nanowires, we found that the wires could often be bent into an arc-shape or with a kink introduced between the two suspended membranes. To check whether the manipulation could significantly alter the transport properties, we performed thermal and electrical measurements on the same silver nanowire with and without an artificial kink created by a sharp probe, which is shown in **Figure 3.6**. The measured electrical and thermal resistance remain essentially the same after the kink is introduced, which suggests that probe manipulation should not affect the transport properties of the wire.

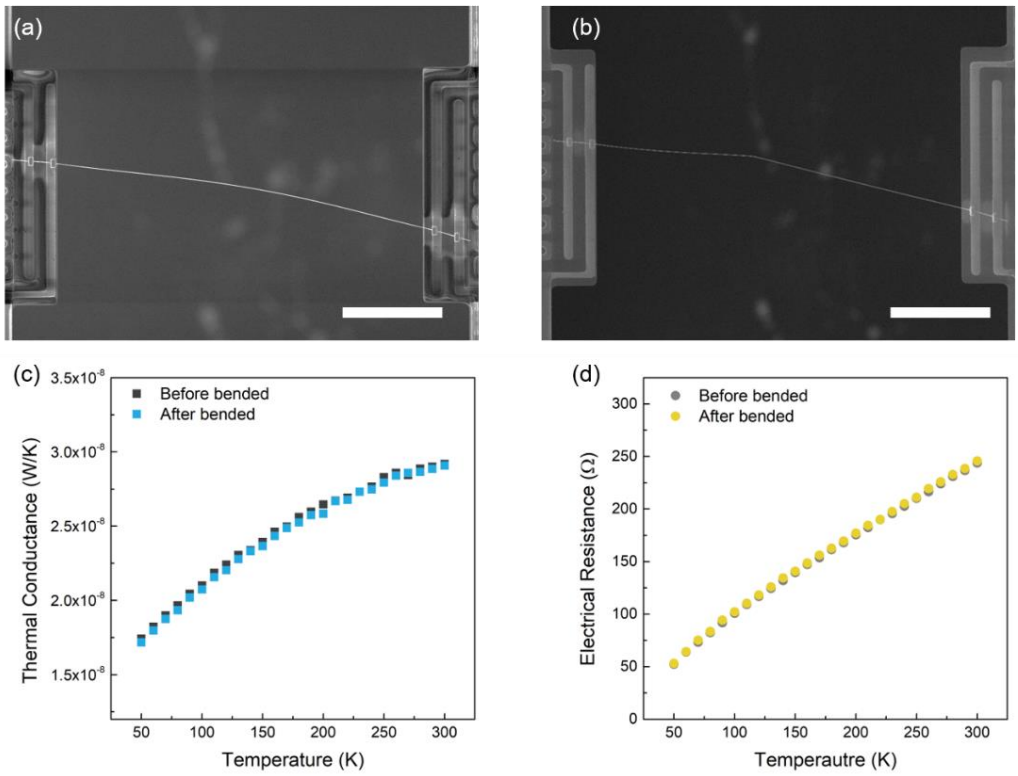


**Figure 3.6** Examination of the effect of probe manipulation. A silver nanowire of 65 nm diameter (a) without and (b) with an artificial kink defect between the two suspended membranes. (c, d) Measured thermal and electrical conductance resistance before and after the kink is introduced. The scale bar in (a) and (b) is 10 μm.

### 3.4 Temperature Dependence of Transport Properties

**Figure 3.7(a)** shows the thermal conductivity of a silver nanowire with $D_h$ = 84 nm and $L_s$ = 44 μm, which demonstrates an increasing trend as temperature increases. The room-temperature thermal conductivity is 332 W/m-K, ~22.6% lower than the bulk value of 429 W/m-K (Ho et al. 1972). Compared to the reported experimental data (Cheng et al. 2015; Kojda et al. 2015; Wang et al. 2018), which range from 200 to 300 W/m-K for silver wires of 90-230 nm in diameter and 7-28 μm long, our results present a higher thermal conductivity for a smaller wire. As mentioned before, for silver nanowires of larger diameters and shorter sample lengths, we found that the contact thermal resistance between the wire and suspended membranes might not be negligible,

which could lead to a lower effective thermal conductivity. Another factor that could contribute to the smaller thermal conductivity in the literature is the estimation of the wire diameter. Silver nanowires often have non-circular cross-sections and calculating their areas with an assumption of a circular shape would overestimate the heat transfer area and consequently lower the thermal conductivity values. For example, in our case, the pentagonal shape of the cross-section corresponding to a hydraulic diameter of 84 nm actually shows an outer-diameter of 96 nm if measured directly from top-view of the SEM micrograph.

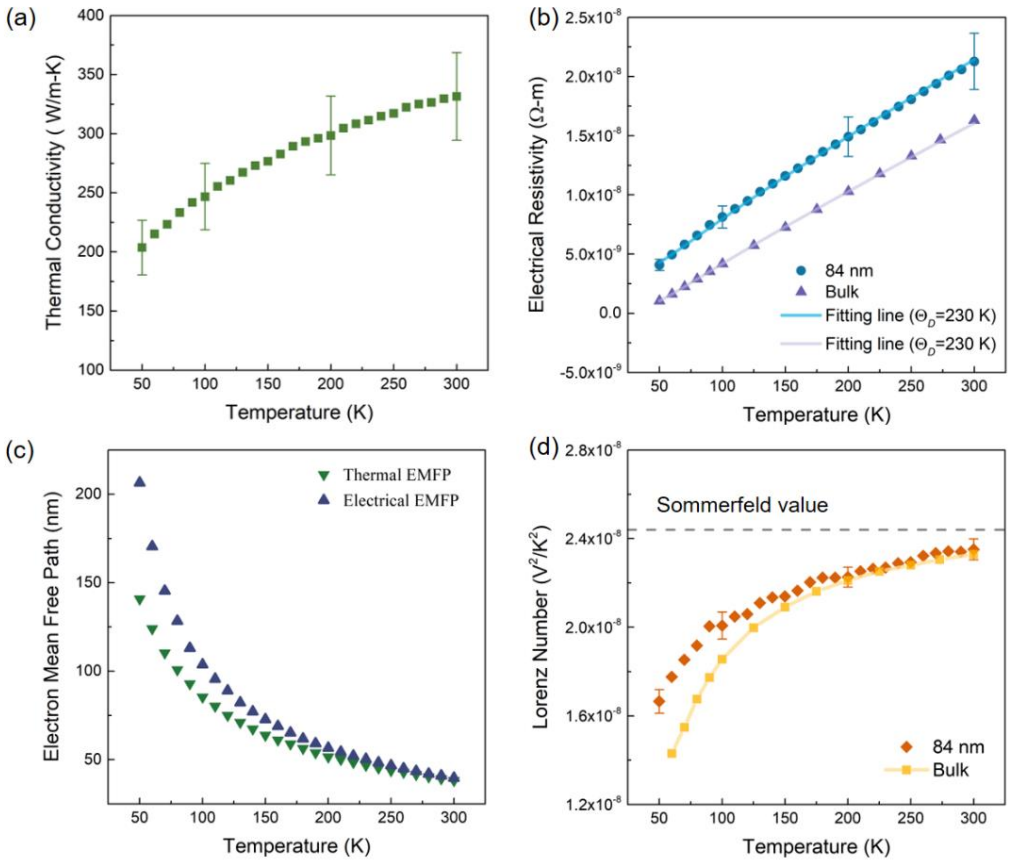


**Figure 3.7** Thermal and electrical properties of an individual silver nanowire with $D_h$ = 84 nm and $L_s$ = 44 μm. (a) Temperature dependence of thermal conductivity. (b) Electrical resistivity of the nanowire and bulk silver (Matula 1979). The solid fitting line for bulk is fitted with Eq. (3.2-3.3) and the fitting line for the nanowire is achieved from Eq. (3.2-3.5). (c) Thermal and electrical EMFP derived from the measured thermal and electrical conductivity. (d) Lorenz number of the nanowire and bulk silver. The bulk value is calculated from the experimental thermal conductivity (Ho et al. 1972) and electrical resistivity (Matula 1979).

The temperature dependence of the electrical resistivity of the same wire is plotted in **Figure 3.7(b)**. Compared to the bulk value of $1.63\times10^{-8}$ Ω-m (Matula 1979), the room-temperature electrical resistivity for the nanowire is 30.7% higher with a value of $2.13\times10^{-8}$ Ω-m. For a nonmagnetic crystalline metal, the temperature dependence of electrical resistivity mainly results from electron-phonon (e-ph) interactions and can be described by the Bloch-Grüneisen (BG) formula as

$$\rho(T) = \rho_0 + \rho_{e-ph}(T), \tag{3.2}$$

$$\rho_{e-ph}(T) = \alpha_{e-ph}\left(\frac{T}{\Theta_D}\right)^5 \int_0^{\frac{\Theta_D}{T}} \frac{x^5}{(e^x-1)(1-e^{-x})}\,dx, \tag{3.3}$$

where $\rho_0$ is the residual resistivity due to defect scattering that is temperature-independent, $\rho_{e\text{-}ph}$ is the resistivity arising from e-ph interactions, $\alpha_{e\text{-}ph}$ is a constant characterizing e-ph coupling, and $\Theta_D$ is the Debye temperature (Tritt 2004). In several reports (Cheng et al. 2015; Kojda et al. 2015), Eq. (3.2) and (3.3) have been used directly to fit the measured resistivity of silver nanowires, which yielded a very low $\Theta_D$ and a rather large $\rho_0$. For example, the best fitting shown in **Figure 3.8** for the 84 nm diameter nanowire gives a Debye temperature of 128 K, much smaller than the bulk value of 230 K. In addition, $\rho_0 = 1.67\times10^{-9}$ Ω-m, which is two orders of magnitude higher than the bulk value ($\sim1\times10^{-11}$ Ω-m). Considering the actually enhanced Young's modulus in silver nanowires, the resulting lower $\Theta_D$ cannot be justified. As such, the fitting in those reports can only be regarded as a BG-like model. More importantly, we found that the fitting gets worse for smaller nanowires, which clearly indicates that a more physical model is needed.

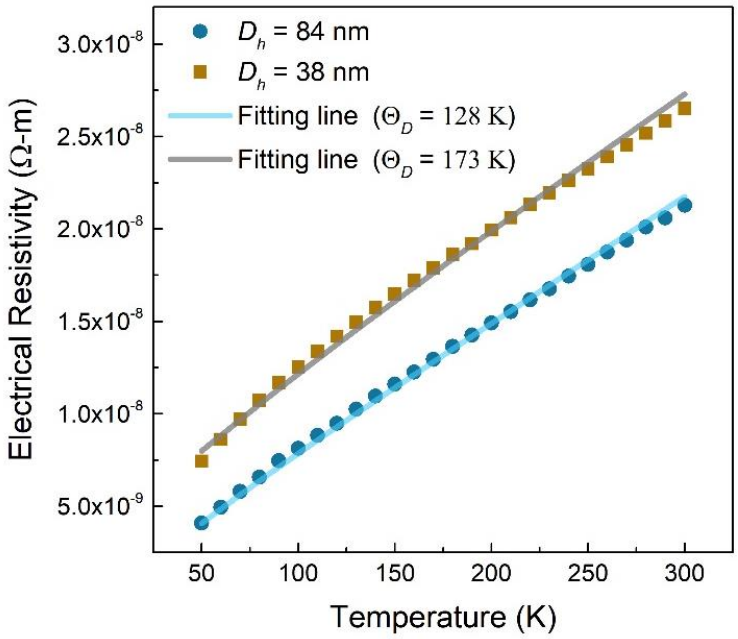


**Figure 3.8** Electrical resistivity of the nanowires with $D_h$ = 84 nm and 38 nm. The best BG fitting gives the Debye temperature that is much lower than the bulk value. Moreover, the BG fitting line gets worse for the 38 nm wire.

The BG-like model does not explicitly consider electron scattering at the nanowires surface, which intends to increase the residue resistance and its temperature dependence reduces $\Theta_D$. To explicitly reflect the surface contribution, we calculate a reduction function following the Fuchs-Sondheimer approach, which relates the nanowire resistivity with the bulk value as (Chambers 1950; Steinhögl et al. 2002)

$$\left(\frac{\rho_{bulk}}{\rho_{nw}}\right)_{p=0,l} = \frac{3}{2\pi {r_0}^2}\int_0^{r_0} r dr \int_0^{2\pi} d\varphi \int_0^{\pi} sin\theta cos^2\theta \left(1 - e^{-\frac{\sqrt{r^2cos^2\varphi + r_0^2 - r^2} - rcos\varphi}{lsin\theta}}\right) d\theta, \quad (3.4)$$

where $\rho_{bulk}$ is the electrical resistivity of bulk silver that can be modeled using Eq. (3.2) and (3.3), $\rho_{nw}$ is the measured electrical resistivity of the nanowire, $r_0$ is the radius of the wire, $\theta$ is the polar angle between the electron traveling direction and the wire axial direction, $\varphi$ is the azimuthal angle and $l$ is the electron mean free path (EMFP) in bulk silver. For simplicity, the above derivation is

based on a circular cross section; however, it has been shown that as long as the S/V ratio (or hydraulic diameter) is the same, the surface scattering effect is approximately the same (Yang et al. 2016). Eq. (3.4) also assumes that electron scattering at the surface is completely diffusive ($p$=0, where $p$ is the specularity parameter). This restriction can be relaxed by introducing specular electron-boundary scattering, and the electrical resistivity is determined by (Chambers 1950; Steinhögl et al. 2002)

$$\left(\frac{\rho_{bulk}}{\rho_{nw}}\right)_{p,l} = (1-p)^2 \sum_{m=1}^{\infty} \left\{ mp^{m-1} \left(\frac{\rho_{bulk}}{\rho_{nw}}\right)_{p=0,\frac{l}{m}} \right\}. \tag{3.5}$$

In this approach, we adopt the bulk $\Theta_D$ = 230 K and fit the nanowire resistivity through combining Eq. (3.2)-(3.5). As shown in **Figure 3.7(b)**, the fitting curve matches the measured data almost perfectly with the following parameters: $\rho_0$ = 8.15×10$^{-11}$ Ω-m, $\alpha_{e\text{-}ph}$ = 5.782×10$^{-8}$ Ω-m, and $p$ = 0.65, which provide minimum variance.

**Figure 3.7(c)** depicts the EMFP derived from the measured electrical and thermal conductivity. The electrical EMFP ($l_{e,nw}$) is calculated as $l_{e,nw} = \frac{\sigma m v_F}{ne^2}$, where $n$ is the free electron density, $m$ is the electron mass, and $v_F$ is the Fermi velocity (Kittel 2004). First principles calculations have suggested that at room temperature phonons in bulk silver only contribute ~1.07% to the total thermal conductivity (Jain and McGaughey 2016). Because phonon MFP is very small in silver (1-10 nm) (Jain and McGaughey 2016), the lattice thermal conductivity of the 84 nm diameter wire can be regarded approximately the same as that of the bulk ($\kappa_{ph,bulk}$ = ~4.6 W/m-K), which is ~1.4% of the measured nanowire thermal conductivity, still a small percentage compared to the electron contribution. As the electronic thermal conductivity is approximately equal to the total thermal conductivity, the thermal EMFP ($l_{th,nw}$) is calculated as $l_{th,nw} = \frac{3\kappa}{C_e v_F}$, where $C_e = \frac{\pi^2 n k_B^2 T}{2E_F}$ is the heat capacity per unit volume in which $k_B$ is the Boltzmann constant and $E_F$ is the

Fermi energy (Kojda et al. 2015; Tritt 2004). For silver, $n$ is $5.85\times10^{28}$ m$^{-3}$, $E_F$ is 5.48 eV and $v_F$ is $1.39\times10^{6}$ m/s (Kittel 2004). The calculated electrical and thermal EMFPs both decrease as the temperature increases due to enhanced e-ph scattering at higher temperatures. The electrical EMFP is larger than the thermal EMFP in the entire measurement temperature range but the difference is very small for $T > 250$ K. At higher temperatures, e-ph interactions mainly occur through large angle scattering, which poses resistance to both electrical and thermal transport (Ziman 2001). However, as the temperature drops, the dominant phonon wave vector decreases, which allows for more electron scattering through small angles either elastically or inelastically. The inelastic scattering only has a marginal effect on charge transport but effectively reduces the relaxation time for thermal transport (Ziman 2001). Thus, the electrical EMFP is always higher than the thermal EMFP and the difference becomes larger as temperature drops.

Based on the W-F law, the Lorenz number can be derived from the measured thermal and electrical conductivity, which is shown in **Figure 3.7(d)**. The resulting Lorenz number of the nanowire increases with temperature, displaying a similar trend as reported for silver (Cheng et al. 2015; Kojda et al. 2015), platinum (Völklein et al. 2009), and gold (Sawtelle and Reed 2019) nanowires or thin films. The Lorenz number of bulk silver is also plotted in **Figure 3.7(d)** for comparison, which is calculated from the experimental thermal conductivity (Ho et al. 1972) and electrical resistivity (Matula 1979). At room temperature, the nanowire has a comparable Lorenz number with the bulk silver. However, as the temperature decreases, the Lorenz number of the nanowire deviates from the bulk value with higher values for the nanowire. Based on the Matthiessen's rule, the size effect on the EMFP of the nanowire can be written as $1/l_{e,nw} = 1/l_{e,bulk} + 1/l_b$, and $1/l_{th,nw} = 1/l_{th,bulk} + 1/l_b$, where $l_{e,bulk}$ and $l_{th,bulk}$ are the electrical and thermal EMFP of bulk silver, respectively; and $l_b$ is the EMFP due to the electron-boundary

scattering with the nanowire surface. When the lattice thermal conductivity is neglected in the 84 nm nanowire, the Lorenz number of the nanowire, $L_{nw} \propto \frac{l_{th,nw}}{l_{e,nw}} = \frac{l_{th,bulk}}{l_{e,bulk}} \times \frac{l_{e,bulk}+l_b}{l_{th,bulk}+l_b} \propto L_{bulk} \times \frac{l_{e,bulk}+l_b}{l_{th,bulk}+l_b}$. The ratio $\left(l_{e,bulk} + l_b\right)/\left(l_{th,bulk} + l_b\right)$ is larger than unity and gets larger as temperature drops, which leads to the higher nanowire Lorenz number at lower temperature than the bulk value.

### 3.5 Size Dependence of Transport Properties

The Lorenz number *versus* temperature for four silver nanowires of different sizes is plotted in **Figure 3.9(a)**, which shows a clear size dependence of higher values for smaller wires. To further clarify the size dependence, we normalized the room-temperature thermal conductivity, electrical conductivity and Lorenz number for different size wires with respect to the corresponding values for the 84 nm wire, as shown in **Figure 3.9(b)**. Both the thermal and electrical conductivities decrease for smaller wires as a result of enhanced boundary scattering, and the electrical conductivity decreases to a greater level, giving rise to an escalating Lorenz number. **Figure 3.9(c)** and **(d)** plot the thermal conductivity and electrical resistivity of four different size wires and the corresponding thermal and electrical conductivity reduction between the 84 and 38 nm wires, respectively. In the entire temperature range, the electrical conductivity reduces to a larger extent as compared to thermal conductivity, giving rise to a higher Lorenz number for smaller wires. First principles calculations have suggested that at 300 K electrons are with MFPs of 10-100 nm and phonons are with MFPs of 1-10 nm in silver (Jain and McGaughey 2016). Therefore, for nanowires with a diameter range of 38-84 nm, boundary scattering could significantly suppress the electron contribution to the thermal conductivity, while the size effect on phonon transport is still marginal. As such, the phonon contribution to the thermal conductivity becomes more significant for smaller wires. This renders the observed more significant reduction

of electrical conductivity than thermal conductivity, and hence the enhanced Lorenz number for smaller wires.

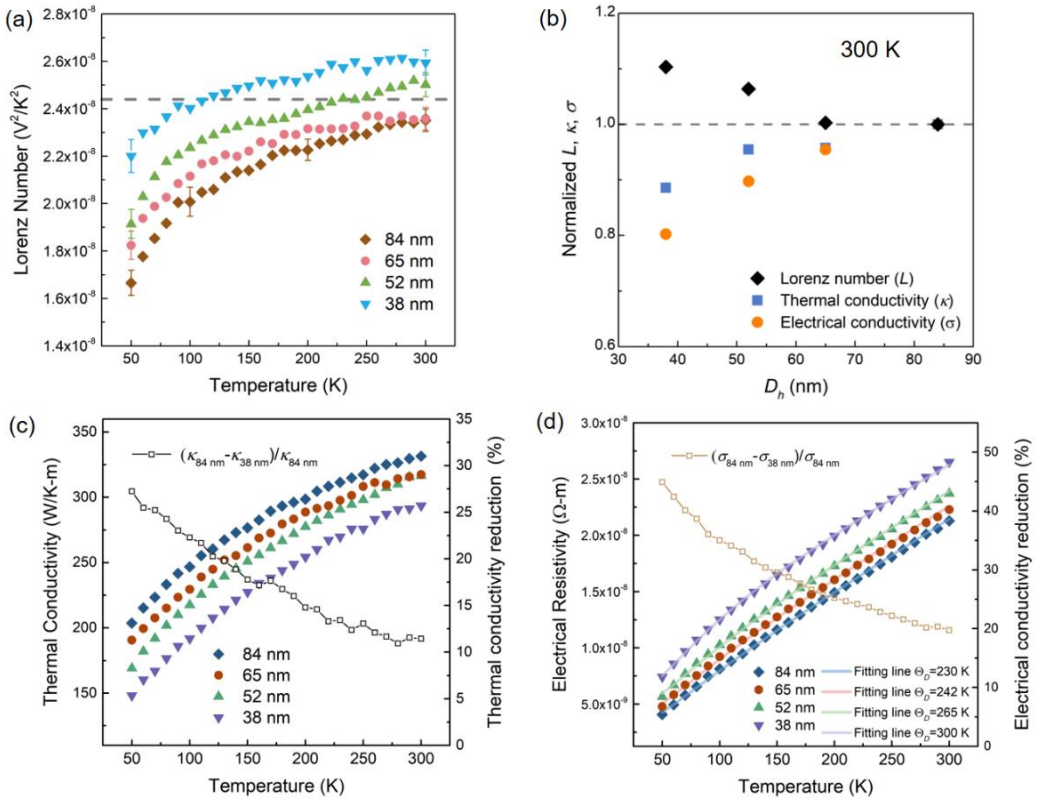


**Figure 3.9** Size dependence of transport properties. (a) Derived Lorenz number of four different diameter silver nanowires. The grey dash line labels the Sommerfeld number. (b) Normalized thermal conductivity, electrical conductivity and Lorenz number with respect to the respective values of the 84 nm diameter nanowire at 300 K. The grey dash line separates the enhanced Lorenz number and reduced thermal and electrical conductivity as size decreases. (c) Thermal conductivity of the four nanowires and the thermal conductivity reduction between 84 nm and 38 nm wires. (d) Electrical resistivity of the four nanowires and electrical conductivity reduction between 84 nm and 38 nm wires. The Debye temperature used for the fitting lines is respectively 230K, 242 K, 265K and 300 K.

While the above analysis is straightforward, the contribution of phonons to thermal transport in nanowires is still relatively small (< 2% for the smallest wire at room temperature with $\kappa_{ph}$ taken as the bulk value of 4.6 W/m-K), which is not sufficient to explain the observed enhancement of

the Lorenz number. In fact, as phonons still contribute a small portion to thermal transport in metals, the measured effective Lorenz number is expressed as

$$L = \frac{\kappa_{ph}+\kappa_e}{\sigma T}, \tag{3.6}$$

where $\kappa_{ph}$ and $\kappa_e$ are the lattice and electronic thermal conductivities, respectively; $\sigma$ is the electrical conductivity; and $T$ is temperature. By subtracting the lattice thermal conductivity from the total thermal conductivity, the Lorenz number purely due to electron transport ($L_e$) can be derived as $\kappa_e/\sigma T$. As shown in **Figure 3.10**, by assuming that the lattice thermal conductivity remains at 4.6 W/m-K for all nanowires, the calculated $L_e$, instead of being independent with size, increases as the wire diameter decreases and even is much larger than the Sommerfeld value for the smallest nanowire. As mentioned previously, it has been shown that elastic stiffening occurs in silver nanowires of less than 100 nm diameter with an increasing Young's modulus for smaller wires. Since the effects of elastic stiffening on transport properties of silver nanowires have not been examined, we analyze the size dependence of these properties.

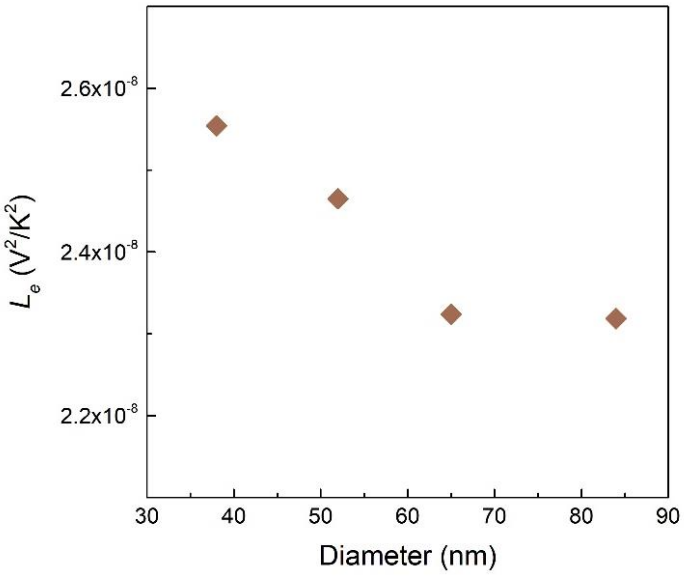


**Figure 3.10** Calculated electronic Lorenz number by assuming that the lattice thermal conductivity remains at 4.6 W/m-K for all nanowires.

To further dissect the effects of elastic stiffening on electrical and thermal transport in silver nanowires, we first model the electrical resistivity for different nanowires. From the measured Young's modulus ($E$) data for silver nanowires (Chang et al. 2016) shown in **Figure 3.11**, we performed a curve fitting to extract the values for the four nanowires with $D_h$ = 84 nm, 65 nm, 52 nm and 38 nm as 1, 1.11, 1.33 and 1.71 times the bulk value, respectively, and derived their corresponding $\Theta_D$. Then following the same procedure as we have done for the 84 nm diameter wire, we fit for the three smaller diameter wires. In the fitting, we also fixed $\rho_0$ to be the same value as that for the 84 nm wire, which is a reasonable assumption given the same nanowire synthesis procedure. Importantly, the fitting is not really sensitive to the value of $\rho_0$ as boundary scattering plays a much more important role at low temperatures. Then we use $p$ and $\alpha_{e\text{-}ph}$ as two fitting parameters to recapture the experimental data, as shown in **Figure 3.9(d)**. The best values for $p$ and $\alpha_{e\text{-}ph}$ are listed in **Table 1**.

**Table 1**. The parameters used for the fitting line for the bulk silver and nanowires.

| $D_h$ (nm) | Normalized $E$ | $\Theta_D$ (K) | $\rho_0$ ($10^{-11}$ Ω-m) | $\alpha_{e\text{-}ph}$ ($10^{-8}$ Ω-m) | $p$ |
|---|---|---|---|---|---|
| **bulk** | 1 | 230 | 1.0 | 5.08 | |
| **84** | 1 | 230 | 8.15 | 5.782 | 0.65 |
| **65** | 1.11 | 242 | 8.15 | 5.996 | 0.62 |
| **52** | 1.33 | 265 | 8.15 | 6.149 | 0.60 |
| **38** | 1.71 | 300 | 8.15 | 6.314 | 0.47 |

The resulting $p$ value is between 0.65 and 0.47, indicating a significant portion of surface scattering is specular reflection. Note that the measured thermal conductivity in our work is about twice of the predicted value based on the Boltzmann transport equation with fully diffuse boundary scattering (Stojanovic et al. 2010), which suggests that the obtained specularity parameter is in a

reasonable range. The specularity parameter $p$ gets smaller progressively for smaller wires, which could be due to the stronger edge effect in the pentagon cross-section. Electrons and phonons tend to be reflected more specularly from a flat surface and the bending of the surface near the edge could render a lower $p$ value. $\alpha_{e\text{-}ph}$, on the other hand increases by almost 10% as the nanowire diameter decreases from 84 to 38 nm. One possible reason is that as suggested by a few publications (Qiu and Tien 1993; Timalsina et al. 2013, 2015), the e-ph coupling factor in nanostructures get enhanced, which could lead to a larger $\alpha_{e\text{-}ph}$. The overall e-ph scattering rate, however, reduces as the nanowire diameter decreases. $\rho_{e\text{-}ph}$ is proportional to the e-ph scattering rate and other than $\alpha_{e\text{-}ph}$, the rest terms in Eq. (3.3) drops as $\Theta_D$ increases, which leads to an overall reduction of $\rho_{e\text{-}ph}$. This is also consistent with the e-ph scattering rate ($1/\tau_{e\text{-}ph}$, where $\tau_{e\text{-}ph}$ is the relaxation time) given by (Yang, Tao, et al. 2019; Ziman 2001)

$$\tau_{e-ph}{}^{-1} = \frac{(m_e E_D)^2 k_B T}{2\pi\rho\hbar^4 v^2}\chi_\omega, \tag{3.7}$$

where $m_e$ and $\rho$ are the effective electron mass and the crystal mass density, $E_D \propto n^{2/3}$ is the deformation potential (here $n$ is the concentration of free charge carriers), $\hbar$ is the reduced Planck's constant, $v$ is the phonon group velocity, and $\chi_\omega = \frac{\hbar\omega}{k_B T}$, $\omega$ is phonon frequency (Asheghi et al. 2002). According to Eq. (3.7) the scattering rate is inversely proportional to the square of the phonon group velocity, which means that as the Young's modulus increases, the e-ph scattering rate reduces.

With the reduced e-ph scattering rate, boundary scattering will play a more significant role in determining the EMFP; and if boundary scattering can effectively limit the electrical and thermal EMFP to the same value, the Lorenz number should be simply the Sommerfeld value. However, as **Figure 3.9(a)** indicates, the Lorenz number for smaller nanowires can be actually higher than the Sommerfeld value, and the difference for the smallest wire is ~6.3% at room temperature, well

beyond the phonon contribution of ~1.7% if we take $\kappa_{ph}$ as the bulk value. This means that for silver nanowires, $\kappa_{ph}$ will be much higher than that of the bulk silver, which can be attributed to several changes induced by elastic stiffening. First, elastic stiffening corresponds to a higher speed of sound, which is directly proportional to $\kappa_{ph}$. In addition, the higher $\Theta_D$ shifts the phonon distribution to lower wave vectors at any given temperature, which should reduce the Umklapp scattering rate. Moreover, as discussed above, the e-ph scattering rate also becomes smaller. The overall effect is significantly enhanced lattice thermal conductivity that renders an effective Lorenz number higher than the Sommerfeld value for small silver nanowires. Actually if we take the room temperature Lorenz number purely due to electron transport as the Sommerfeld value, the lattice thermal conductivity for the 38 nm wire can be derived as 17.5 W/m-K, over three times that of the bulk value of 4.6 W/m-K.

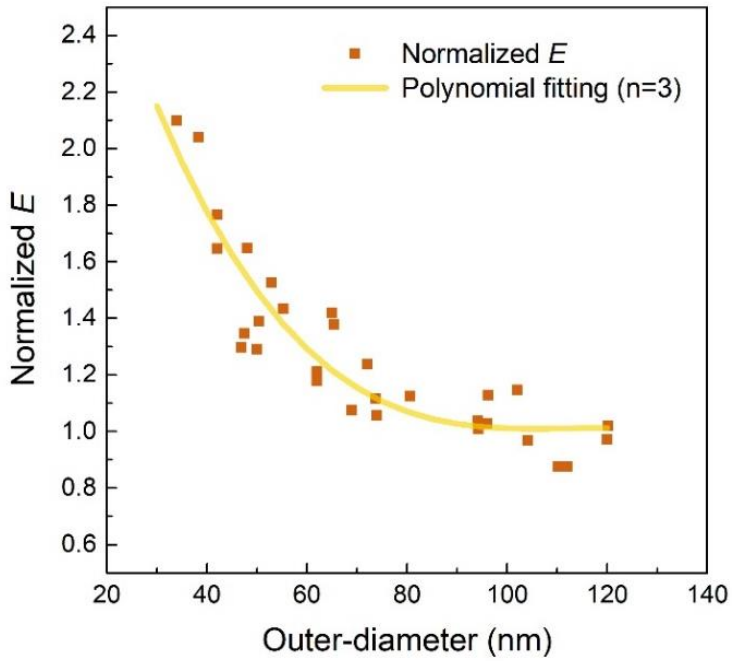


**Figure 3.11** Extracted Young's modulus for the four nanowires with $D_h$ = 84 nm, 65 nm, 52 nm and 38 nm, which corresponds to the outer-diameter of 96 nm, 72 nm, 58 nm and 42 nm, respectively

It is worth noting that the elastic stiffening in penta-twinned silver nanowires is likely originated from both the surface atom reconstruction and compression at the twin boundaries (Chang et al. 2016; Niekiel et al. 2015), which leads to a rather uniform enhancement of Young's modulus across the wire cross-section. As such, we consider the elastic stiffening effects on transport properties based on an effective average value of the Young's modulus for the entire nanowire.

### 3.6 Transport at the Contact between Two Individual Silver Nanowires

As mentioned before, contacts can play an important role in the properties of composites and we seek to extract the electrical and thermal contact resistances between individual nanowires, following the same approach as we took to study the contact thermal resistance between individual multi-wall carbon nanotubes (MWCNTs) (Yang et al. 2014). First, a long silver nanowire with $D_h$ = 65 nm was cut into three segments. Two segments were aligned between the two suspended membranes with a point contact in the middle (**Figure 3.12(a)**). The third segment was placed on an identical device with the suspended length approximately the same as the heat transfer path of the sample with the contact (the suspended length of the single wire ($L_s$) and the wires with a contact ($L_c$) are 38.0 μm and 39.8 μm, respectively, a 4.7% difference). **Figure 3.12(b)** shows an SEM micrograph of the wire-wire junction with the two nanowires etched away taken at a tilt angle of 52° after the EBID Pt/C deposition and FIB cutting. The small hole between the two wires represents the contact between the two wires. Measurements using ImageJ yielded an area of 107 $\pm$17.6 nm$^2$ for the contact. The contact area is nearly 2 times that between two MWCNTs of similar diameters, which could be due to the contact being between two flat edges of the silver nanowires with pentagonal cross-sections. The measured electrical and thermal resistances of the single wire and the sample with the contact are plotted in **Figure 3.12(c)** and **(d)**. The results show 11-27%

higher electrical resistance and 7-16% higher thermal resistance for the sample with the contact than the corresponding values for the single wire sample over the whole temperature range.

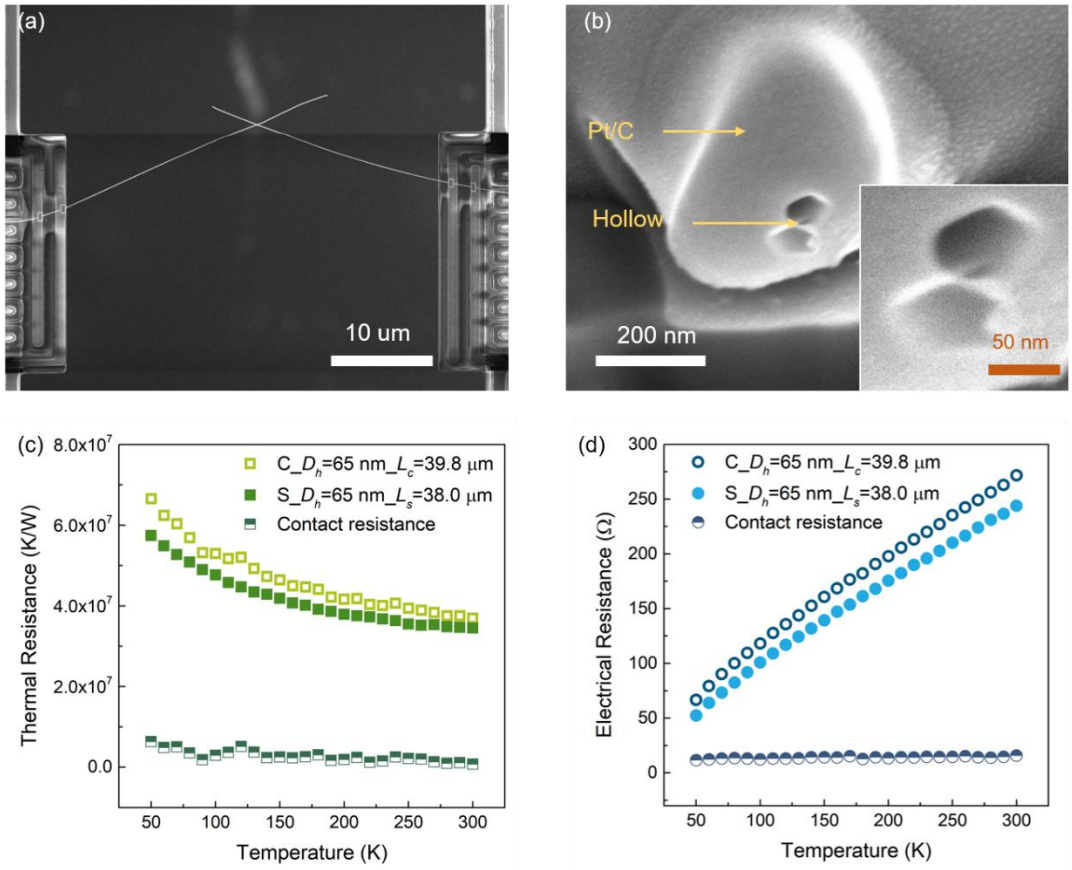


**Figure 3.12** Thermal and electrical properties at an individual contact between two silver nanowires. (a) SEM image of two contacted silver nanowires with $D_h$ = 65 nm. (b) SEM image of cross-sectional cutting of contacted silver nanowires tilted at 52°. The inset is the zoom-in image of the contact configuration. (c) Thermal and (d) electrical resistance of single and contacted nanowires as well as their contact resistances.

The contact resistance, $R_C$, can be derived according to $R_C = R_{t,contact} - R_s/L_s \times L_c$, where $R_{t,contact}$ is the measured total resistance of the contact sample and $R_s$ is the measured resistance of the single nanowire (Yang et al. 2010, 2014). The contact electrical and thermal resistances are also shown in **Figure 3.12(c)** and **(d),** which are about one-tenth of the measured total resistance of the single and contact samples. This relatively low weight of the contact resistance in the measured total

resistance results in quite significant fluctuations in $R_C$, even though the fluctuation in the measured total resistance is relatively small. Although the extracted contact resistance carries quite a large uncertainty, useful information can still be derived. For example, at 300 K, compared to the contact thermal resistance of ~$1.8\times10^7$ K/W between two 63 nm diameter MWCNTs as reported by Yang et al. (Yang et al. 2014), the contact thermal resistance between two 65 nm hydraulic diameter silver wires is only $7.70\times10^5$ K/W, which is ~22 times lower. The much lower contact thermal resistance between silver nanowires suggests that silver nanowires could be much more effective nanofillers to enhance the thermal performance of nanocomposites.

To understand the much lower contact thermal resistance, we solve for the contact thermal conductance per unit area ($G_{CA}$), as a comparison of $G_{CA}$ for the nanowires with that between two MWCNTs could provide more insights into the reduced contact resistance. The calculated $G_{CA}$ is $12.1\times10^9$ W/K-m$^2$, which falls in the range of 4-$14\times10^9$ W/K-m$^2$ for some metal-metal interfaces (Gundrum et al. 2005; Wilson and Cahill 2012), but represents ~10 times that between MWCNTs. Possible reasons for this higher contact conductance are as follows. First, the electron MFP is ~ 36 nm at 300 K, much less than ~200 nm for phonons propagating along the radial direction in MWCNTs. This eliminates reflection of energy carriers back to the emitting tube/wire, which is one important factor for the low $G_{CA}$ at MWCNT contacts (Yang et al. 2014). Furthermore, it has been shown that Joule heating during electrical measurement could help to enhance the bonding between metal nanowires (Song et al. 2014; Vafaei et al. 2014), which could also facilitate transmission of energy carriers through the contact.

### 3.7 Effective Lorenz Number of the Point Contact between Silver Nanowires

With the extracted electrical resistance ($R_{C,E}$) and thermal resistance ($R_{C,T}$) at the contact, we study the effective Lorenz number of the point contact which is calculated as $L = R_{C,E}/(R_{C,T}T)$.

**Figure 3.13(a)** and **3.13(b)** show the contact electrical and thermal resistance derived from three sets of single and contacted silver nanowires with $D_h$ of 92 nm, 91 nm and 43 nm. The contact electrical resistance only shows a marginal temperature dependence, whereas the contact thermal resistance decreases rapidly at low temperatures and then gradually levels off above 100 K. The point contact between nanowires may be modeled as a circular constricted area with a radius of $a$, as schematically illustrated in **Figure 3.13(c)**. Assuming that the contact electrical resistance entirely comes from the geometrical restriction, $a$ can be estimated from the measured $R_{C,E}$. If $\lambda_e$ is smaller than $a$, the diffusive contact resistance can be determined by the Maxwell formula $R_{C,E} = 1/(2\sigma a)$ (Maxwell 1892). While for $\lambda_e > a$, the ballistic contact resistance derived by Sharvin can be expressed as $R_{C,E} = 2h/(ek_F a)^2$, where $h$ is Planck's constant and $k_F$ is the Fermi wave vector (Sharvin 1965). The measured $R_{C,E}$ is nearly temperature independent, indicating that electron transport at the contact is dominated by Sharvin resistance; and $a$ is estimated as 2.4 nm, 2.9 nm, and 1.7 nm for the three sets of samples, respectively. It is worth noting that the obtained $a$ represents the lower bound of the contact size as weak bonding and impurities at the contact could also contribute to the contact electrical resistance. On the other hand, we experimentally measured the contact area between two silver nanowires with a hydraulic diameter of 65 nm, which is 107.0 ± 17.6 $nm^2$, corresponding to a contact radius of 5.3-6.3 nm. This experimentally determined value serves as the upper bound of the contact size.

As shown in **Figure 3.13(d)**, for all three samples, the normalized effective Lorenz number of the point contact ($L/L_0$) increases sharply at low temperatures, reaches a peak value of 3.7-5.2 around 50 K, and then decreases monotonically as temperature further rises. The temperature dependence of $L/L_0$ for the point contact is very different from that for single silver nanowires and bulk silver, but consistent with the trend theoretically predicted for gold and platinum atomic

junctions using first principles calculations (Bürkle and Asai 2018). Interestingly, as shown in **Figure 3.13(d)**, $L/L_0$ of the point contact demonstrates a clear size dependence with a higher value for a smaller contact. It should be noted that the variation of $L/L_0$ among the three samples is well beyond the measurement uncertainty, which is less than 13% above 100 K.

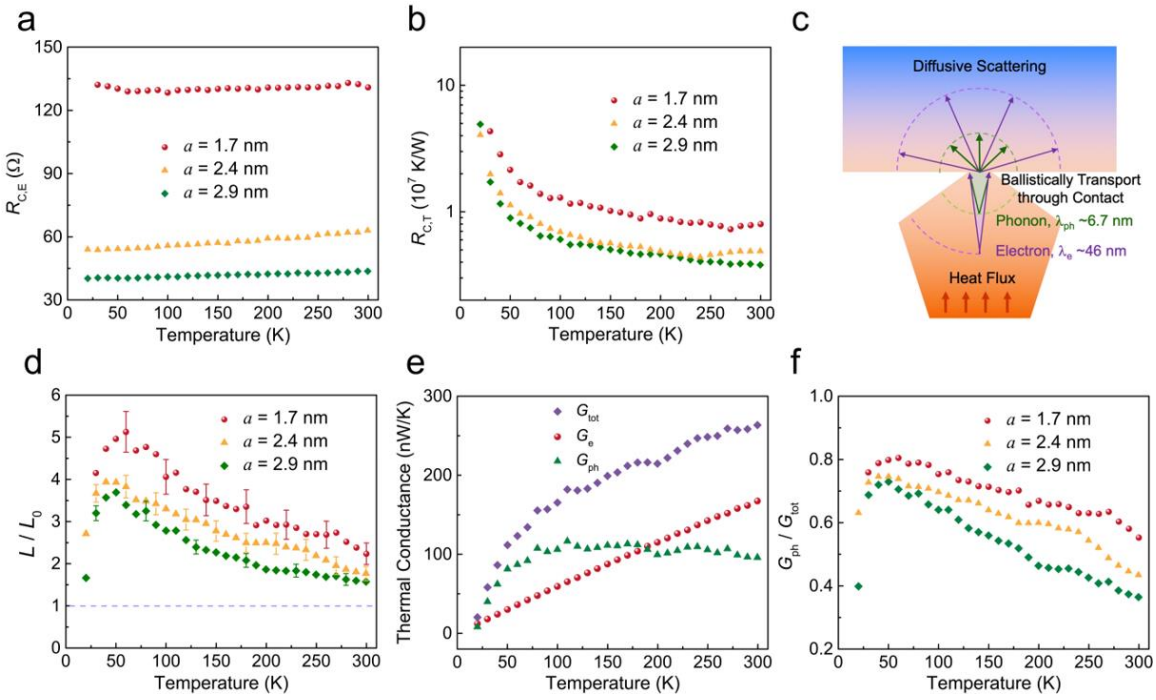


**Figure 3.13** (a) Extracted electrical ($R_{C,E}$) and (b) thermal resistance ($R_{C,T}$) of the point contact between silver nanowires with $D_h$ of 92 nm, 91 nm and 43 nm, respectively. *a* denotes the radius of the contact area. (c) Schematic diagram of electron and phonon transport through the point contact between silver nanowires. (d) $L/L_0$ of the point contact for the three samples. (e) Total thermal conductance ($G_{tot}$), electron thermal conductance ($G_e$), and phonon thermal conductance ($G_{ph}$) of the point contact for the 91 nm wire. (f) $G_{ph}/G_{tot}$ of the point contact for the three samples.

To elucidate the underlying mechanism, we separated the contribution of electrons and phonons to the total thermal conductance of the point contact by assuming that the electronic contribution to thermal conductance and electrical conductance follows the W-F law with the Lorenz number taken as the Sommerfeld value. Based on the measured $R_{C,E}$ and $R_{C,T}$, we can estimate the electron ($G_e$) and phonon thermal conductance ($G_{ph}$) of the point contact as $G_e =$

$L_0T/R_{C,E}$ and $G_{ph} = G_{tot} - G_e = 1/R_{C,T} - G_e$, as shown in **Figure 3.13(e)**. $G_e$ increases linearly with temperature since $R_{C,E}$ is nearly temperature independent. $G_{ph}$ ramps up quickly at low temperatures and then slightly decreases with the further rise of temperature. As a result, a crossover between $G_e$ and $G_{ph}$ occurs at 180 K. Note that the Debye temperature of bulk silver is ~230 K. Based on the model proposed by Prasher (Prasher 2005), $G_{ph} = 2\kappa_{ph}a/(1 + \frac{8\lambda_{ph}}{3\pi a})$, where $\lambda_{ph}$ is the phonon MFP. According to the kinetic theory (Kittel 2004), $\kappa_{ph} = C_{ph}v\,\lambda_{ph}/3$, where $C_{ph}$ is the specific heat. At low temperatures, $G_{ph}$ increases sharply with temperature as $C_{ph}$ escalates following the Debye $T^3$ law (Ashcroft and Mermin 1976). As temperature further increases, $C_{ph}$ gradually levels off while $\lambda_{ph}$ drops due to enhanced scattering at higher temperatures. As such, $G_{ph}$ demonstrates a decreasing trend as temperature increases beyond 100 K. The rapid escalation of $G_{ph}$ with temperature below 50 K as compared to $G_e$ leads to the sharp increase of $G_{ph}/G_e$ in this temperature range. Above 50 K, the escalation rate of $G_{ph}$ is smaller than that of $G_e$, and thus $G_{ph}/G_e$ decreases with temperature. Collectively, the above analyses suggest that the significant phonon contribution to the contact thermal conductance is responsible for the higher $L/L_0$ and the distinct temperature dependence of $G_{ph}$ and $G_e$ leads to the non-monotonic temperature dependence of $L/L_0$ for the point contact.

**Figure 3.13(f)** shows the ratio of $G_{ph}$ to $G_{tot}$ for the three samples, which indicates that the relative contribution of phonons to the contact thermal conductance increases when the contact size decreases, leading to a higher $L/L_0$ as shown in **Figure 3.13(d)**. The size dependence can be explained based on the different MFPs of electrons and phonons in silver. To date, the phonon MFP in silver has not been experimentally determined yet. Recent first principles calculations predicted an average $\lambda_{ph}$ of 6.7 nm for silver at 300 K (Tong et al. 2019). In addition, it has been suggested that electrons with $\lambda_e$ of 10-100 nm and phonons with $\lambda_{ph}$ of 1-10 nm are responsible

for thermal transport in silver at 300 K (Jain and McGaughey 2016). As shown in **Figure 3.13(c)**, at room temperature, $\lambda_e$ is 46 nm for the 92 nm wire, more than 15 times larger than $a$, while $\lambda_{ph}$ is only about 2-4 times of $a$. As such, electrons will be scattered more significantly than phonons at the point contact, giving rise to a larger reduction in $G_e$ than in $G_{ph}$ when reducing $a$. Therefore, it is reasonable to expect that $G_{ph}/G_{tot}$ and thus $L/L_0$ of the point contact will be larger for a smaller contact size.

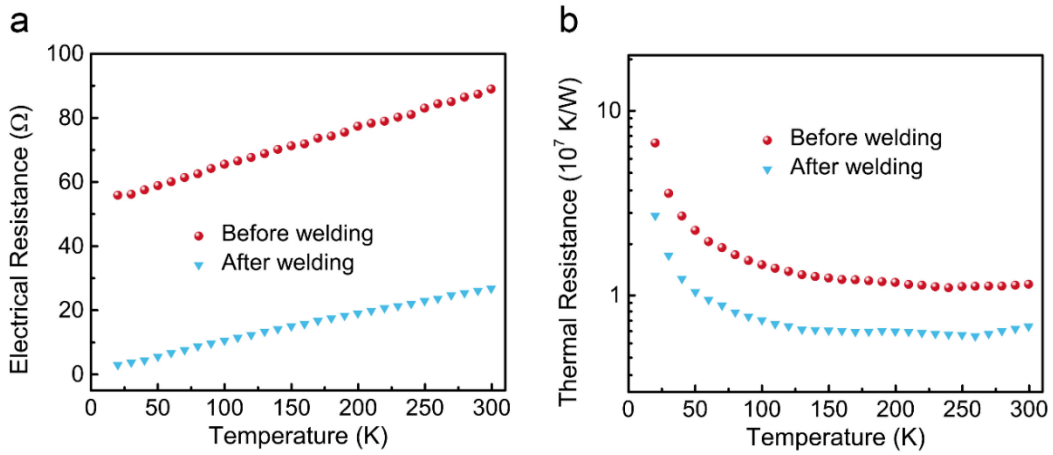


**Figure 3. 14** (a) Measured electrical and (b) thermal resistance of the contact silver nanowires with $D_h$ of 92 nm before and after welding.

To further understand $L/L_0$ of the point contact, we performed current-induced welding of the point contact and compared $L/L_0$ of a contact sample before and after welding. Specifically, after measuring a contact sample, an electrical current of ~100 μA was passed through the point contact, and then the sample was measured again. Results in **Figure 3.14** show that the electrical and thermal resistance of the contact sample decrease dramatically after welding. As an electrical current is driven through the point contact, Joule heating is generated locally at the contact and significantly reduces the contact resistance (Bellew et al. 2015). **Figure 3.15(a) and (b)** show the SEM images of the point contact before and after welding, which indicate that current-induced welding increases the contact area. In addition, the bonding strength between the two silver

nanowires should also be enhanced. The welding treatment drastically reduces the extracted $R_{C,E}$, as shown in **Figure 3.15(c)**, which renders a large uncertainty in the derived $L/L_0$ for the point contact due to the small portion of $R_{C,E}$ in the measured total electrical resistance. Therefore, instead of extracting $L/L_0$ for the point contact, we calculated $L/L_0$ for the contact sample before and after welding. As shown in **Figure 3.15(d)**, before welding, $L/L_0$ of the contact sample shows a temperature dependence similar to that of the point contact but with lower values. After welding, $L/L_0$ of the contact sample nearly overlaps with that of the single silver nanowire, indicating that compared to the nanowire segments, the electrical and thermal resistance of the point contact are marginal.

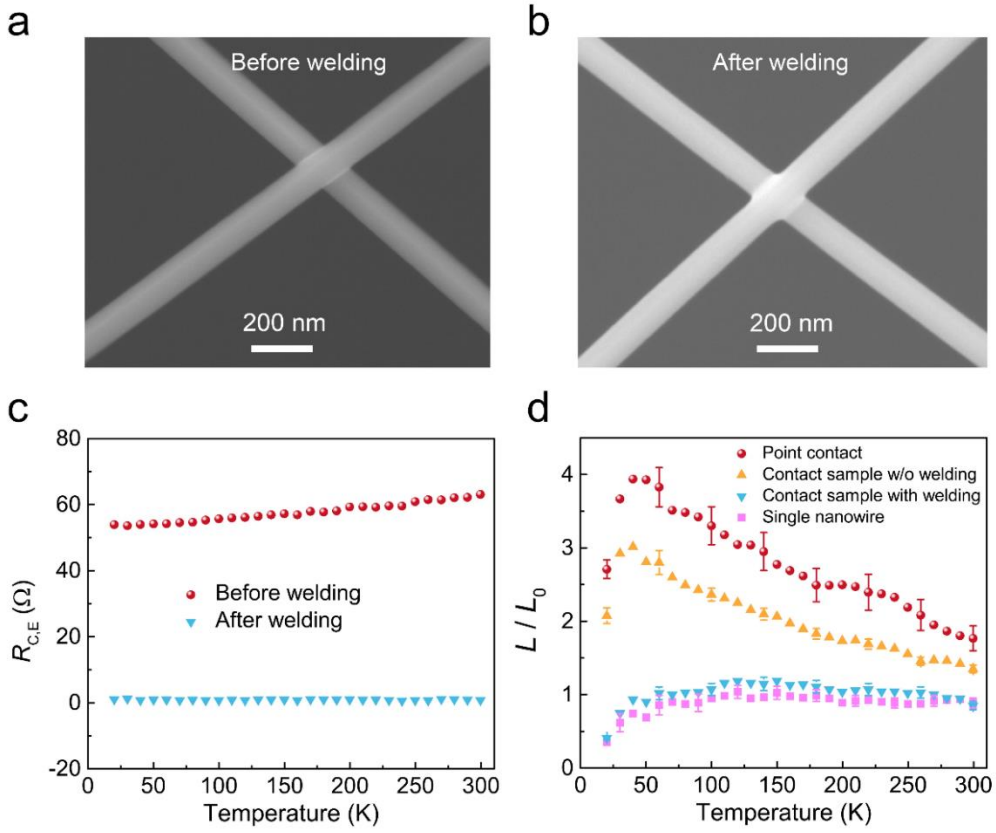


**Figure 3.15** SEM images of the point contact (a) before and (b) after welding for the 92 nm nanowire. (c) Extracted $R_{C,E}$ before and after welding. The $R_{C,E}$ is reduced significantly by current-induced welding at the point contact. (d) $L/L_0$ of the contact sample before and after welding. The $L/L_0$ of the point contact and the single silver nanowire are also shown for comparison.

The difference induced by welding suggests that as long as thermal transport is dominated by electrons, the effective Lorenz number is close to the Sommerfeld value. In fact, the recent reports show that the W-F law even holds at the gold and platinum atomic junctions at room temperature with marginal contribution from phonons (Cui et al. 2017; Mosso et al. 2017, 2019). However, without the welding treatment, the much more significant Sharvin resistance to electron transport at the silver point contact renders a large portion of phonon contribution in the contact thermal conductance. In this case, the effective Lorenz number deviates from the Sommerfeld value. To examine the relative contribution of phonons to thermal transport through metal interfaces/contacts, we plotted the normalized effective Lorenz number measured here together with those reported for various metal interfaces (Gundrum et al. 2005; Wilson and Cahill 2012), metal atomic junctions (Bürkle and Asai 2018; Cui et al 2017; Klöckner et al. 2017; Möhrle et al. 2019; Mosso et al. 2017, 2019), and metal nanostructures (Kojda et al. 2015; Ou et al. 2008; Völklein et al. 2009; Yoneoka et al. 2012) as a function of the characteristic size at 300 K in **Figure 3.16**. Similar to bulk metals, thermal transport through metal interfaces is dominated by electrons, thus giving rise to $L/L_0$ close to unity (Wilson and Cahill 2012). Typically less than 10% phonon contribution is observed for thermal transport in metal nanowires and thin films with a characteristic size on the order of 100 nm (Kojda et al. 2015; Ou et al. 2008; Völklein et al. 2009). Phonons could contribute ~33% of thermal conductance at 300 K for a 7.3 nm thick platinum thin film (Yoneoka et al. 2012). For point contacts, as the characteristic size is below the electron MFP, electrons will undergo stronger scattering at the contact than phonons because of their inherently larger MFP. The significant phonon contribution could result in the size-dependent effective Lorenz number in this regime as we observed for the point contact between silver nanowires. However, when the characteristic size goes down to the atomic level, gold and platinum atomic junctions show marginal phonon

conductance (Bürkle and Asai 2018; Cui et al 2017; Klöckner et al. 2017; Möhrle et al. 2019; Mosso et al. 2017, 2019), whereas up to 40% phonon contribution to the total thermal conductance is predicted for aluminum atomic junctions because of its higher Debye energy (Klöckner et al. 2017). These results indicate that the phonon contribution at metal contacts not only depends on the contact size but also the intrinsic properties of contacting materials.

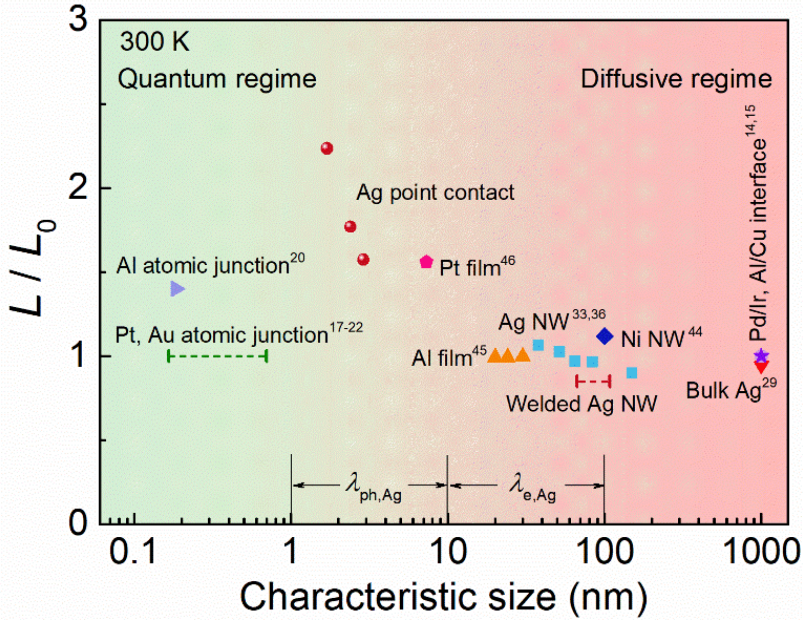


**Figure 3.16** Summary of $L/L_0$ at 300 K as a function of the characteristic size.

### 3.8 Summary

In summary, systematic studies at the individual nanowire and contact level provide direct experimental evidence of altered effective Lorenz numbers in silver nanowires and their contacts. The clear trend of increasing Lorenz numbers for smaller silver nanowires comes mainly from the effects of elastic stiffening, which results in reduced electron-phonon scattering rates and higher Debye temperatures. These changes significantly enhance the phonon contribution to the thermal transport, while the electron contribution is not boosted to the same level because boundary scattering effectively limits the electron MFP in silver nanowires. Importantly, the study provides

experimental data on the contact thermal conductance per unit area, which is ~10 times that between MWCNTs, indicating one factor that renders silver nanowires more effective nanofillers for enhancing the thermal conductivity of nanocomposites. The effective Lorenz number of the point contact between silver nanowires demonstrates a non-monotonic temperature dependence and an increasing trend as the contact size decreases. Analyses suggest that these observations are due to the severe Sharvin resistance to electron transport and the enhanced relative phonon contribution to the thermal conductance at the point contact. We further demonstrate that welding can largely eliminate this deviation as it drastically reduces the resistance to electron transport and thus the weight of phonon contribution. The systematic study discloses interesting transport mechanisms and provides important insights into designing silver nanowire-based composites.

# Chapter 4

## Thermoelectric Properties of Individual Contacts between Multiwall Carbon Nanotubes

Carbon nanotubes (CNTs), owing to their extraordinary physical and chemical properties, have been applied extensively in thermal energy conversion (Huang et al. 2005; Romano et al. 2013; Yu et al. 2014) and thermal management (Li et al. 2011; Mahmoodi et al. 2011). However, in many cases it is not the intrinsic properties of CNTs, but the transport properties at the contacts between CNTs that determine the overall performance of CNT-based materials. For example, tremendous efforts have been made to use CNTs as nanofillers to tune the electrical and thermal properties of polymeric composites and it has been concluded that the contacts between CNTs and interfaces between CNTs and host materials play critical roles in the resulting properties (Fuhrer et al. 2000; Yanagi et al. 2010; Yang et al. 2014). One interesting observation from the CNT-polymer composites is that their thermoelectric properties could be significantly better than the corresponding pure polymers (Du et al. 2012; Hewitt et al. 2011, 2012; Meng, Liu, and Fan 2010; Yao et al. 2010), and it has been suggested that contacts and interfaces could make important contributions to this enhancement. However, detailed mechanisms are still under debate.

To date, most understandings on transport through CNT-CNT contacts are inferred from measurements of CNT bundles, thin films, or bulk materials (bulky papers) involving a large amount of CNT contacts. It is challenging to draw solid conclusions on the transport phenomena at the CNT contacts because complications from the intrinsic properties of CNTs, variations of contact morphologies, and changes in the temperature jump at the contacts could all lead to inconsistent observations. Pioneering studies (Tian et al. 1997; Hone et al 1998) of CNT bundles and ropes assumed that the measured thermoelectric power was a result of the combination of the intrinsic properties of metallic and semiconductor tubes and did not consider any contribution from

the tube contacts. Shortly after, however, it was pointed out that the positive thermoelectric power observed by Tian et al. and Hone et al. might not be the intrinsic properties of the tubes but came from inter-tube electron hopping in randomly aligned CNTs with tube-tube junctions (Baxendale et al. 2000). However, to fit the experimental data, multiple fitting parameters had to be introduced and even different expressions could give equally well fitting results (Baxendale et al. 2000; Choi et al. 2003b; Hewitt et al. 2012). Therefore, more solid evidence for the effects of electron hopping at the tube-tube contact is still needed.

In this chapter, we report on more direct measurements of the thermoelectric properties of the contact between two individual multiwall CNTs, which are realized through establishing a temperature drop along samples composed of two CNTs connected with a point contact. Through comparing with single tubes, we demonstrate that electron hoping at the CNT-CNT contact could convert the negative Seebeck coefficient of an individual CNT to a much larger positive value of the contact sample and further enhance the thermoelectric performance.

### 4.1 Sample Preparation

The thermal measurement was performed following the well-established approach in a high-vacuum cryostat system ($<10^{-6}$ mbar) using a microdevice with pre-patterned platinum electrodes and resistance heaters/thermometers (Yang, Tao, et al. 2019; Zhang et al. 2017; Zheng et al. 2013). The platinum electrodes at the side of the membranes allow to conduct four-point electrical measurement and Seebeck coefficient measurement. A very long multiwall CNT was cut into three segments with two of them being used to form the contact sample and the third part as the corresponding single CNT segment. **Figure 4.1** illustrates two sets of the contact and single CNTs aligned between two suspended membranes of the microdevice with roughly the same suspended length, which are denoted as C#1, S#1, and C#2, S#2. The tube diameter for the #1 and #2 CNTs

are 45 nm and 40 nm, respectively. EBID of Pt/C at the tube-membrane contacts was applied to enhance the electrical and thermal contacts.

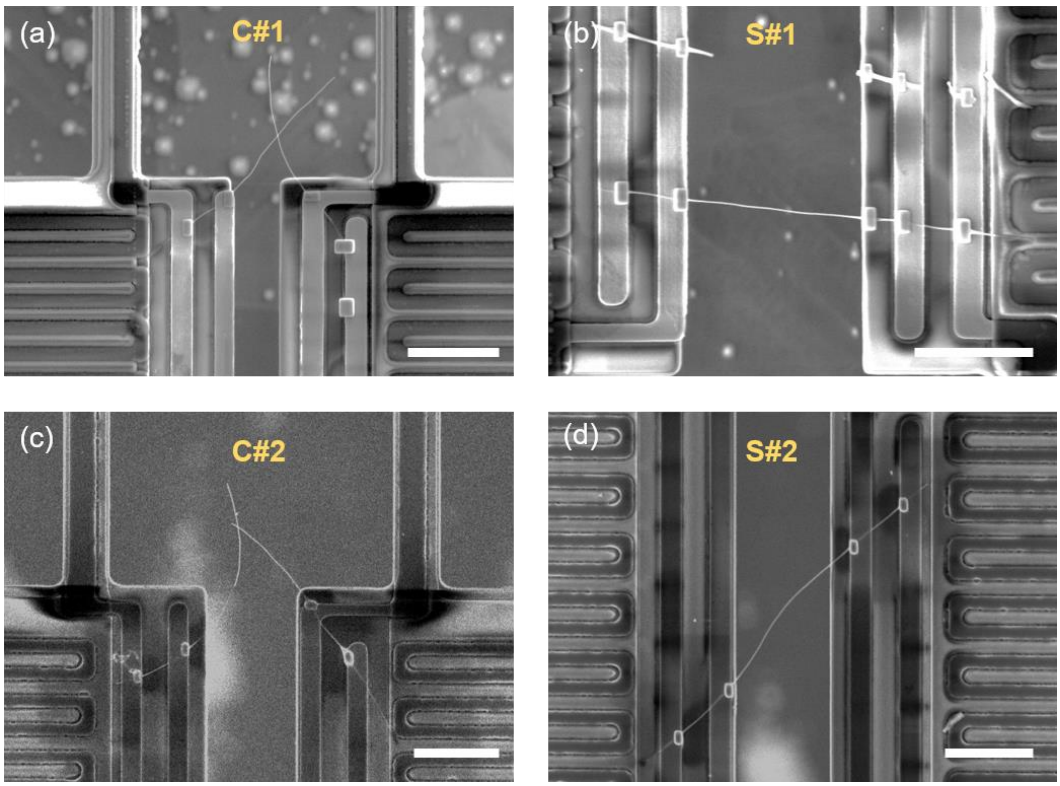


**Figure 4.1** SEM micrographs of the contact and single CNTs on microdevice. The tube diameter is 45 nm for the #1 CNTs and 40 nm for the #2 CNTs. The scale bars are 4 μm.

### 4.2 Thermal and Electrical Transport Properties of the Point Contact

The contact thermal resistance between individual CNTs has been measured previously and it was shown that the thermal conductance of the point contact is proportional to $D^{2.4}$, where $D$ is the diameter of the tube (Yang et al. 2014). As such, we first examine whether the contact thermal conductance of these two sets of samples match this trend. **Figure 4.2(a)** shows the measured thermal resistance ($R_t$) as a function of temperature. The total thermal resistance of the contact CNTs is much larger than that of its corresponding single tube, which indicates that the point contact could pose significant thermal resistance. In fact, the resistance of the C#1 and C#2

samples increases by 1.2 times and 1.9 times that of the corresponding single one at 300 K, respectively. Based on the equation as (Yang et al. 2010)

$$R_{cont} = R_{tot\_c} - R_{tot\_s}\frac{l_{tot\_c}}{l_{tot\_s}}, \tag{4.1}$$

the contact resistance ($R_{cont}$) can be derived from the measured thermal resistance of the contact and single CNTs. Here, $R$ and $l$ denote the resistance and sample length, respectively, and the subscripts *cont*, *tot_c*, *tot_s* represent the point contact, the contact CNTs, and the corresponding single CNT, respectively. **Figure 4.2(b)** shows the calculated thermal conductance of the point contact ($G_{t\_cont} = 1/R_{t\_cont}$) together with the data for the four tubes from our previous work (Yang et al. 2014), which approximately follow $D^{2.4}$ law.

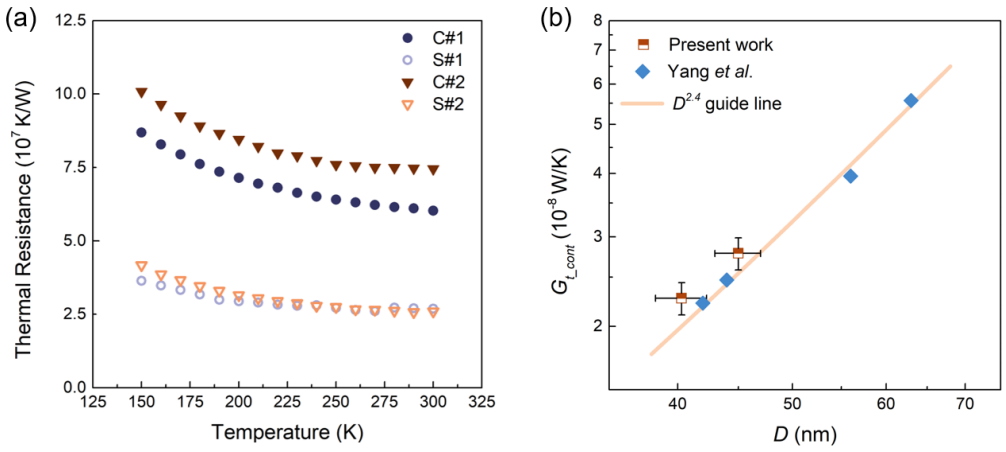


**Figure 4.2** Thermal transport property. (a) Thermal resistance of the contact and single CNTs in the temperature range from 150 K to 300 K. (b) Thermal conductance of the point contact ($G_{t\_cont}$) at room temperature. The contact thermal conductances derived from the two sets of CNTs in our work approximately follow the same size dependence of $D^{2.4}$ with the previous work (Yang et al. 2014).

**Figure 4.3(a)** shows the measured electrical resistance ($R_e$) of the contact and single CNT samples. The room-temperature electrical conductivity of the S#1 and S#2 sample is $8.89\times10^4$ S/m and $1.55\times10^5$ S/m, respectively, consistent with the reported experimental values of $10^4$~$10^7$ S/m for individual CNTs (Ebbesen et al. 1996; Fischer et al. 1997; De Heer et al. 1995; Wei et al. 1999).

The electrical resistance of the point contact between the two tubes was calculated using Eq. (4.1). At 300 K, the contact poses an electrical resistance of 20.4 kΩ for C#1 and 68.3 kΩ for C#2, which are on the same order of the contact resistance between MWCNT and graphite (Paulson et al. 2000). It is worth noting that the point contact electrical resistance takes ~35% and ~60% of the total resistance of the C#1 and C#2 samples, respectively.

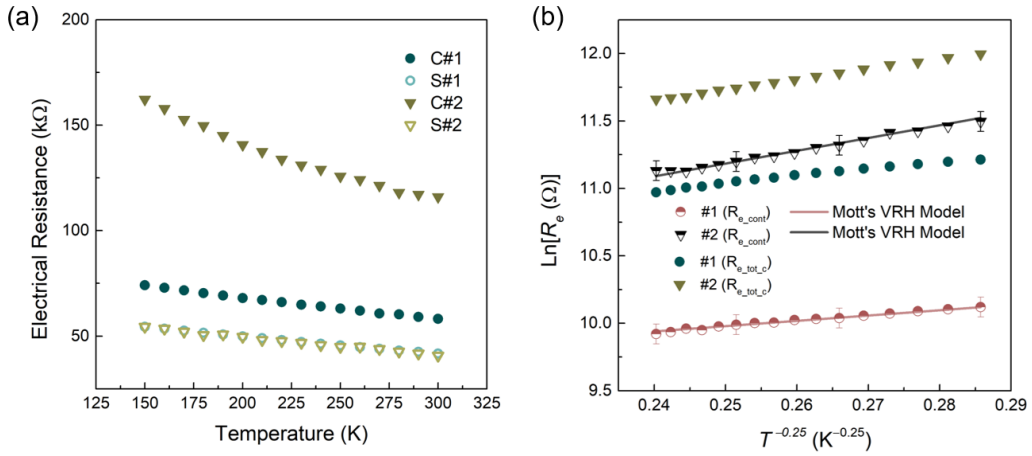


**Figure 4.3** Electrical transport property. (a) Measured electrical resistance of the contact and single CNTs. (b) Natural log of the electrical resistance of the point contact and contact samples as a function of $T^{-1/4}$. The solid lines show the fitting results based on Mott's VRH 3D model.

The mechanism of electron transport in CNT-based assemblies and polymeric composites is frequently explained by Mott's VRH model, which is expressed as (Mott and Davis 1979)

$$R = R_0 \exp\left[(T_0/T)^{\frac{1}{1+d}}\right], \tag{4.2}$$

where $d$ is the dimension, $R_0$ is the constant and $T_0$ is the characteristic temperature (Aggarwal et al. 2007; Bandow et al. 2007; Lee et al. 2000; Yanagi et al. 2010). As shown in **Figure 4.3(b)**, the temperature dependence of contact electrical resistance ($R_{e\_cont}$) for the two sets of CNTs can be fitted well based on the VRH model with $d$ = 3 in the temperature range of 150-300 K, which demonstrates the three-dimensional (3D) hopping conduction at the tube contact. As a comparison, we also plotted the total electrical resistance of the contact CNTs in **Figure 4.3(b)**. Since the

electrical resistance of the C#1 sample mainly comes from the contribution of single segments, the natural log of the total electrical resistance of the contact CNTs ($R_{e\_tot\_c}$) deviates from the $T^{-1/4}$ dependence. However, as the contact electrical resistance is dominating for the C#2 sample, $R_{e\_tot\_c}$ approximately follows the same temperature dependence as its $R_{e\_cont}$. The results indicate that for CNT-based assemblies and composites with numerous tube-tube junctions, as the contacts play a significant role, the overall electrical performance agrees well with the contact electrical properties (Blackburn et al. 2008; Li et al. 2007).

In the VRH model, the parameter $T_0$ can be extracted from the linear fitting for the contact electrical resistance and the expression for $T_0$ can be written as

$$T_0 = \frac{24}{\pi k_B N(E_F) \xi^3}, \tag{4.3}$$

where $k_B$ is the Boltzmann constant, $N(E_F)$ is the electronic density of states at the Fermi level, $\xi$ is the localization length. In the literatures, $N(E_F)$ is estimated to be on the order of $10^{24}$ $eV^{-1}m^{-3}$ for amorphous carbon and carbon films and $10^{27}$ $eV^{-1}m^{-3}$ for one-layer CNTs (Tsebro et al. 1998). As MWCNTs are graphitic materials, we chose $N(E_F)$ for graphite, $4.81 \times 10^{26}$ $eV^{-1}m^{-3}$ (Bandow et al. 2007) to calculate $\xi$. Based on the Eq. (4.3) the calculated $\xi$ is 9.2 nm for the #1 CNTs and 2.8 nm for the #2 CNTs. With $\xi$, the hopping distance ($L_h$) can be derived from the equation of $L_h = \left(\frac{3\xi}{2\pi k_B N(E_F) T}\right)^{1/4}$. At 300 K, the electron hopping distance at the point contact is 4.3 nm and 3.2 nm for the #1 and #2 CNTs, respectively, which is comparable with 5.7 nm for $Fe_{70}Pt_{30}$ catalyzed MWCNTs film (Aggarwal et al. 2007) and much lower than the value of ~160 nm for MWCNT sheets (Yosida 1999). The hopping dimensionality can be determined by the hopping distance and the c-axis size of the contacted CNTs; as the hopping distance is smaller than the c-axis size of the contact CNTs, the electron hopping transport is 3D (Yosida 1999). The far smaller $L_h$ in our work

confirms that the mechanism of electron transport at the CNT-CNT contacts is 3D VRH conduction.

### 4.3 Thermoelectric Properties of the Point Contact

**Figure 4.4(a)** and **(b)** present the measured effective Seebeck coefficient for the #1 and #2 CNTs, respectively. For the #1 samples, the contact converts the Seebeck coefficient from a negative value of the single CNT to a positive one of the contact CNTs. Based on the fibrillar model, the total Seebeck coefficient of the contact CNTs ($S_{tot\_c}$) is the sum of the Seebeck coefficient of the single segment ($S_{tot\_s}$) and the point contact ($S_{cont}$) weighed by the corresponding thermal resistance, which can be expressed as (Kaiser 1989)

$$S_{tot\_c} = S_{tot\_s}\frac{R_{t\_tot\_s}}{R_{t\_tot\_c}} + S_{cont}\frac{R_{t\_cont}}{R_{t\_tot\_c}}. \tag{4.4}$$

Based on Eq. (4.4), the Seebeck coefficient of the point contact for the #1 and #2 CNTs could be derived, which is positive and larger than that of the contact CNTs at 300 K. The results confirm the previous study that the significant positive Seebeck coefficient induced by the contacts is the main reason for the negative-to-positive transition as the form of CNT networks changes from bundles to mats (Baxendale et al. 2000).

The hopping Seebeck coefficient is expressed as (Baxendale et al. 2000; Zvyagin 1973)

$$S_h = \frac{k_B^2}{2e}(T_0 T)^{\frac{d-1}{d+1}}\frac{d\ln\sigma(E)}{dE}\Big|_{E_F}, \tag{4.5}$$

where $e$ is the elementary charge, $\sigma(E)$ is the conductivity-like function of electron of energy $E$, $E_F$ is the Fermi energy. Based on Eq. (4.5), we plotted the derived contact Seebeck coefficient as a function of $T^{1/2}$ in **Figure 4.4(c)** and the linear dependence between $S_{cont}$ and $T^{1/2}$ demonstrates the 3D electron hopping transport at the point contact. In the previous studies, because of the non-negligible thermoelectric contribution from single segments in CNT mats or bundles, the expression that is used to describe the temperature dependence of the Seebeck coefficient has to

include the multiple fitting parameters to account for the contribution from the metallic segments, semiconducting segments, and hopping conduction at contacts (Baxendale et al. 2000; Hewitt et al. 2012). In contrast, our work is the first to provide the experimental evidence for both electrical and thermoelectric responses at an individual contact level in the VRH regime.

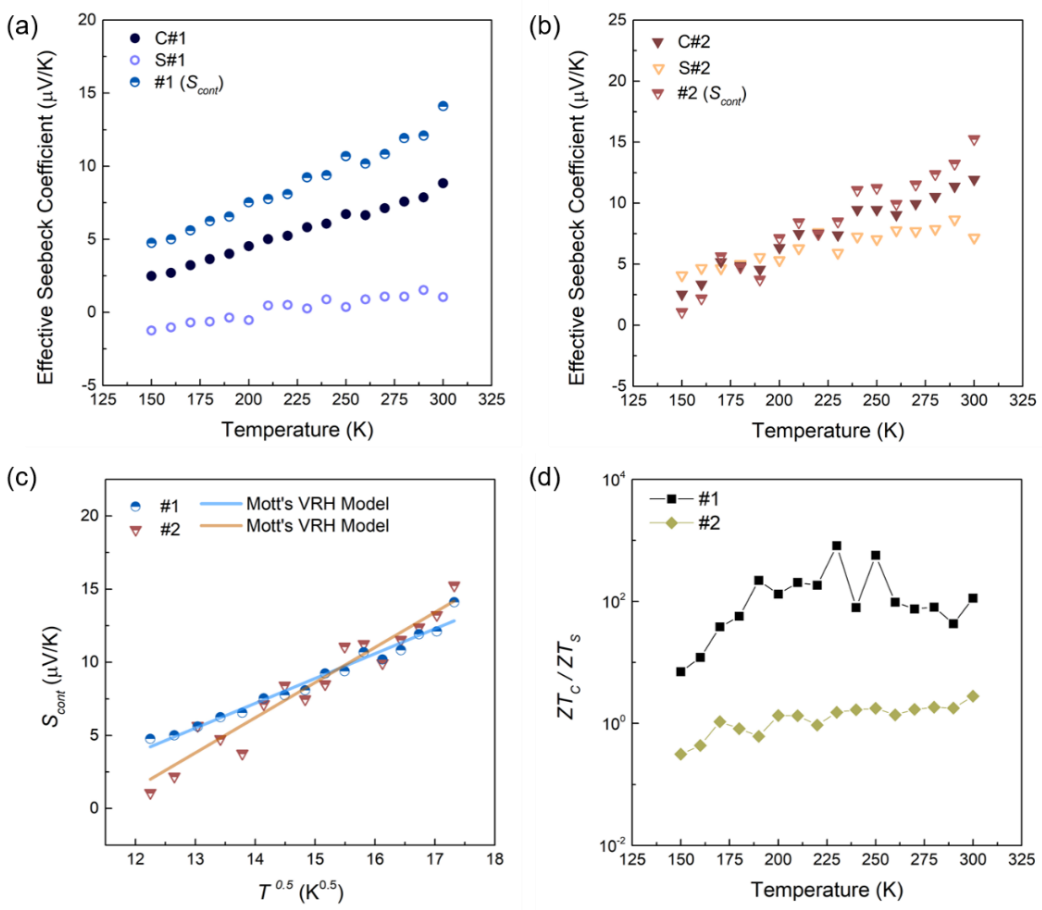


**Figure 4.4** Effective Seebeck coefficient of the contact and single CNTs for (a) the #1 samples and (b) the #2 samples, and their derived contact Seebeck coefficient based on the fibrillar model. (c) Contact Seebeck coefficient as a function of $T^{1/2}$. The linear fitting line is derived based on the Mott's VRH model. (d) Ratio of *ZT* between the contact and single CNTs.

With the measured thermal resistance, electrical resistance and Seebeck coefficient, the thermoelectric efficiency was estimated by the dimensionless *ZT*. **Figure 4.4(d)** shows the ratio of *ZT* between the contact and single CNTs. Although the thermal and electrical conductance can be largely reduced by the tube contact, the *ZT* of the C#1 sample is enhanced by almost two orders of

magnitude at 300 K with the significant contribution from the positive contact Seebeck coefficient. However, because of the comparable Seebeck coefficient of the single CNT and point contact for the C#2 sample, the *ZT* enhancement is only about two times. Taken together, these data suggest that contact could improve the thermoelectric performance of CNT-based materials.

### 4.4 Summary

In summary, the experimental studies disclose the electrical and thermoelectric transport properties at the individual point contact between multiwall CNTs. The unique temperature dependences of the electrical resistance and Seebeck coefficient of the point contact confirm the 3D VRH conduction mechanism at the tube contact. Attractively, the thermoelectric performance of the contact CNTs could be significantly improved with the help of the positive contact Seebeck coefficient. Our findings provide clear evidence for electron hopping conduction at the CNT-CNT contact, and further demonstrate that the electron hopping conduction could help to enhance thermoelectric performance of CNT-based materials.

# Chapter 5

## Kink Effect on Thermal Transport in Silicon Nanowires

Transport mechanisms underlying heat transfer in nanostructures are of fundamental interest and critical for a broad range of applications, such as thermoelectrics (Chowdhury et al. 2009; Hochbaum et al. 2008; Majumdar 2004; Shi 2012; Tian, Lee, and Chen 2013), electronics cooling (Li et al. 2005; Momose et al. 2003; Yang et al. 2017), and data storage (Kim et al. 2000). In the past two decades, intensive efforts have been devoted into understanding nanoscale thermal transport (Cahill et al. 2014; Jauregui et al. 2010; Luo and Chen 2013), and many interesting phonon transport phenomena in low-dimensional nanostructures have been discovered.

Beyond the classical size effect (Boukai et al. 2008; Mingo et al. 2003; Volz and Chen 1999), various interesting observations due to nanoconfinements have been reported. For example, while the measured thermal conductivity of large diameter (>37 nm) silicon nanowires can be explained by phonon-boundary scattering, a 22 nm-diameter wire demonstrates data much lower than the predicted values based on the classical size effect (Li et al. 2003). Later, studies indicate that for silicon nanostructures with a characteristic size <30 nm, the Young's modulus drops dramatically, which alters phonon dispersion and reduces phonon group velocity, resulting in lower thermal conductivity (Wingert et al. 2015; Yang et al. 2016). In addition, it has been shown that surface roughness can also play a significant role in the thermal conductivity of nanowires (Hochbaum et al. 2008).

Complex morphologies have been regarded as a newly recognized degree of freedom to tune the thermal conductivity of nanowires. Using non-equilibrium molecular dynamics (NEMD) simulation, it was shown that a single kink in a 1.1 nm diameter, 19 nm long silicon wire can reduce its thermal conductivity by ~20%, which is attributed to the phonon mode interchanging

and pitching effects (Jiang et al. 2013). More astonishingly, a recent experiment study suggested that a single kink in a ~80 nm diameter, 4.3 μm long boron carbide nanowire could reduce its thermal conductivity by ~36%, which means that the kink poses ~30 times larger thermal resistance than a corresponding straight nanowire segment of equivalent length (Zhang et al. 2017). Interestingly, it was also shown that defects in the kink region, instead of posing resistance, actually facilitated phonons passing through the kink.

In this chapter, we use NEMD to model thermal transport through kinked silicon nanowires. The simulation results clearly demonstrate that back scattering of phonons from the free surface of the kink is the underlying mechanism for the additional kink resistance. By adding heavy isotope atoms into the kink region, we further verify that defects can indeed assist phonon transmission through the kink.

### 5.1 Non-Equilibrium Molecular Dynamics Simulation Method

All simulations were carried out using the LAMMPS package; and the Stillinger-Weber (SW) potential was adopted to describe the interaction between silicon atoms (Stillinger and Weber 1985). The Newton's equations of motion for each atom were numerically solved using the velocity Verlet algorithm with an integration time step of 1 fs. The total simulation time for each case was set in the range of 20 to 26 ns that was chosen based on the simulation system size.

Non-periodic boundary conditions are applied along all three directions. The atoms within the first layer of one unit cell (UC) thickness at the two ends are fixed. Adjacent to these two fixed layers, another two layers are designed as the hot and cold reservoirs whose temperatures are controlled by applying the Langevin thermostat. The temperatures of the two baths are set as $T_0 + \Delta T/2$ and $T_0 - \Delta T/2$, respectively, where $T_0$ is the equilibrium temperature of 300 K and $\Delta T$ is the temperature difference of 60 K between the two reservoirs.

During the simulation, after the steady state is achieved, the heat added into the hot reservoir, $Q_H$, and that subtracted from the cold reservoir, $Q_C$, are collected every 10 ps. The amount of heat transferred from the hot reservoir to cold reservoir is calculated by averaging the absolute value of $Q_H$ and $Q_C$. The linear fitting slope of the heat transfer as a function of time is the average heat transfer rate, $q_{ave}$. Based on the Fourier's Law, the thermal resistance is calculated as

$$R = \frac{\Delta T}{q_{ave}}. \tag{5.1}$$

The phonon DOS is calculated from the Fourier transform of the velocity autocorrelation function as (Sokhan, Nicholson, and Quirke 2000)

$$g(\mathbf{k}, v) = \mathcal{F}\{\langle \boldsymbol{v}(t) \cdot \boldsymbol{v}(0) \rangle\} = \int_0^\infty dt exp(2\pi i v t) \sum_j \exp(i\mathbf{k}\mathbf{r}_j) \frac{\langle \boldsymbol{v}_j(t) \cdot \boldsymbol{v}_j(0) \rangle}{\langle \boldsymbol{v}_j(0)^2 \rangle}, \tag{5.2}$$

where $i$ is imaginary unit, $v_j(t)$ is the velocity of the atom $j$ at the time $t$, $\mathbf{k}$ is the wave vector, and $\mathbf{r_j}$ is the position of the atom $j$. With the velocity of three different directions obtained from the simulation, the phonon DOS can be extracted for longitudinal and transverse modes, respectively.

## 5.2 Simulation Model of Straight and Kinked Silicon Nanowires

**Figure 5.1** depicts the schematic diagrams of both straight and kinked nanowires in our simulations, where the kinked nanowire is divided into the arm and kink segments. All the structures are built on the (100) surface of diamond-like silicon with a square cross section of 4 UC × 4 UC, and the lattice constant is 0.5431 nm. For a meaningful comparison, each pairs of straight and kinked nanowires are of the same total length and have the same number of atoms. We choose a larger cross-section than that of Jiang et al. (Jiang et al. 2013) because recent MD results suggest that too small nanowires, i.e., 2 UC × 2 UC cross-section modeled with SW potential, could be unstable (Yu et al. 2016; Zhou et al. 2017). In our simulation, we vary the arm length ($L_{arm}$) of the kinked nanowire from 6 UC to 12 UC (corresponding to 3.26 nm to 6.52 nm, respectively) to examine its effect on the resulting thermal resistance of the kink.

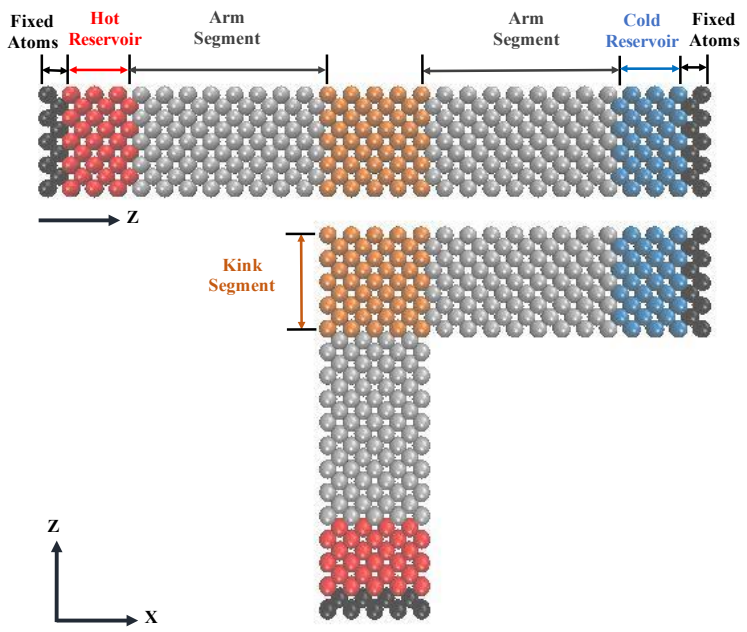


**Figure 5.1** Atomic structures of the straight and kinked silicon nanowires.

### 5.3 Thermal Transport in Straight and Kinked Silicon Nanowires

**Figure 5.2** plots the total thermal resistance for the straight and kinked nanowires, which indicates that for all different arm lengths of 6, 8, 10, and 12 UC, the kinked wire has a higher thermal resistance than the corresponding straight wire. There is also a discernable trend of larger difference in the thermal resistance between the kinked and straight wires as the arm length increases. When the arm length reaches 12 UC, the kinked nanowire poses a thermal resistance that is ~7% more than the straight nanowire of the same length. This level of thermal resistance enhancement corresponds to a thermal conductivity reduction of 6%, which is significantly smaller than the experimental result of up to 36% obtained from kinked boron carbide nanowires (Zhang et al. 2017), and the possible reasons will be discussed later.

Since the total thermal resistance depends on the wire length, a more informative way to measure the kink effect is to solve for the resistance induced by the kink, $R_{kink\_ind}$, and compare

with the resistance of a straight wire segment of equivalent length, $R_{straight\_equ}$, as done by Zhang et al. (Zhang et al. 2017). Here, $R_{kink\_ind}$ and $R_{straight\_equ}$ are defined as

$$R_{kink\_ind} = R_{total\_kinked} - R_{total\_straight}$$
$$R_{straight\_equ} = R_{total\_straight} \times L_{kink}/L_{total}, \quad (5.3)$$

where $R_{total\_kinked}$ and $R_{total\_straight}$ are the total thermal resistance of the kinked and straight nanowires, respectively. $L_{kink}$ is the length of the kink segment, which is 4 UC, and $L_{total}$ is the total length of the straight nanowire. The normalized kink-induced resistance, $R_{kink\_ind}/R_{straight\_equ}$, represents the additional resistance induced by the kink normalized with respect to a straight wire segment of equivalent length, which is also plotted in **Figure 5.2**. It can be seen that as the arm length increases from 6 UC to 12 UC, $R_{kink\_ind}/R_{straight\_equ}$ increases from ~0.2 to ~0.6.

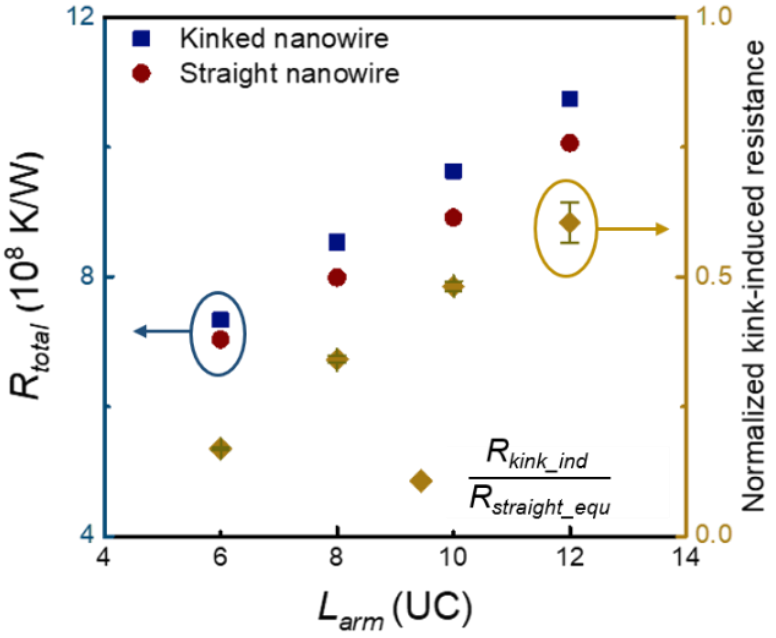


**Figure 5.2** Total thermal resistance and normalized kink-induced resistance

To understand how kinks pose additional thermal resistance, we examine the temperature profile along the heat transfer path. **Figure 5.3(a)** displays the temperature profiles collected during steady-state simulation period for a kinked and corresponding straight wire with an 8-UC

arm length. The temperature profile of the straight nanowire is linear along the entire wire, which is consistent with our expectation. However, the temperature profile for the kinked nanowire demonstrates an unexpected trend – instead of a larger temperature drop at the kink, the temperature drop across the kink is smaller than that across 4 UC wire segment in the corresponding straight wire. The temperature gradient in the two arm regions of the kinked nanowire, on the other hand, is larger than that in the corresponding straight nanowire.

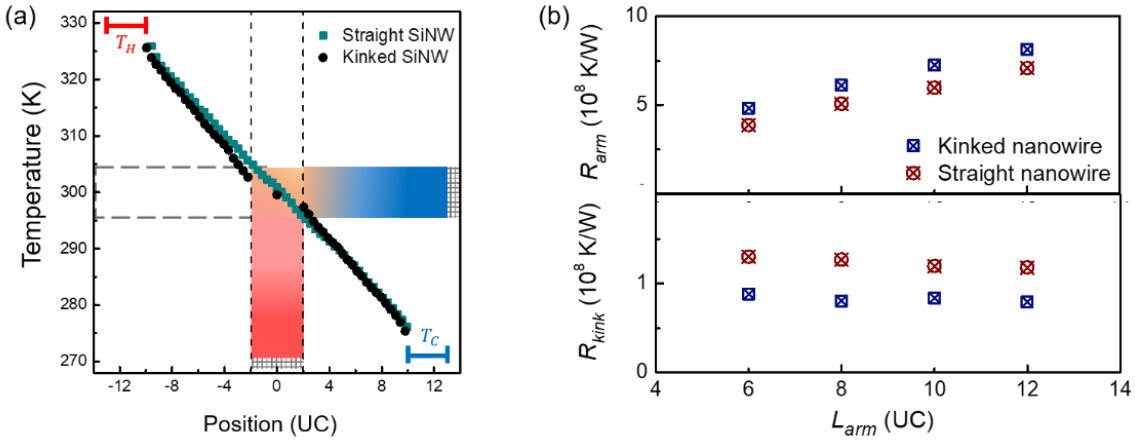


**Figure 5.3** (a) Temperature profiles of the kinked and straight nanowires with the arm length of 8 UC. The center of the nanowires is taken as the original point with the distance from the center to the hot and cold side labelled with negative and positive numbers of UC. (b) The thermal resistance of the arm and kink segment.

Based on the temperature profile, we calculated the thermal resistance of each arm segment, $R_{arm}$, and the kink/equivalent segment, $R_{kink}$ (note that $R_{kink}$ is different from $R_{kink\_ind}$) using Eq. (5.1) for both kinked and straight nanowires, and the results are shown in **Figure 5.3(b)**. Corroborating with the smaller temperature drop, the thermal resistance of the kink segment in kinked wires is smaller than that of a 4 UC segment in straight wires; however, the arm resistance is larger than that in straight wires. The enhanced arm resistance in kinked nanowires suggests that the additional thermal resistance induced by the kink ($R_{kink\_ind}$) can be attributed to the reflection of phonons back into their respective incoming arms by the free surfaces of the kink. The detailed mechanism of

how the kink enhances the arm resistance is related to the underlying mechanism of phonon transport in the out-of-plane direction of a thin film with a thickness much smaller than the phonon MFP.

### 5.4 Theoretical Analysis on Thermal Transport in Kinked Silicon Nanowires

As suggested by Li and McGaughey recently (Li and McGaughey 2015), when phonons transport in the out-of-plane direction of a thin film, they will travel ballistically to the boundary if the film thickness is much smaller than the phonon MFP. Then phonons will be reflected back and, after traveling back and forth, eventually experience a three-phonon scattering event somewhere within the film. To confirm this, we conducted an NEMD simulation of thermal transport through a silicon film of 8 UC thick. The cross-section of the simulation domain is 12 UC × 12 UC with periodic boundary conditions applied on each side of the cross-section. With the temperature of the heat source and sink set as 330 K and 270 K, we obtained a heat flux of $6.36\times10^{10}$ W/m$^2$. If all phonons emitted from the heat source travel ballistically to the heat sink and are absorbed by the heat sink, then the heat flux can be predicted based on the equation of phonon radiative transport (EPRT), expressed as (Majumdar 1993)

$$q''_{EPRT} = \frac{\sigma\left(T_H^4 - T_C^4\right)}{0.75\left(\frac{t}{l_{mfp}}\right)+1}, \tag{5.4}$$

where $T_H$ and $T_C$ are the temperature of the hot and cold reservoir, set as 330 K and 270 K, respectively; $t$ is the film thickness; $L_{mfp}$ is the phonon MFP; and $\sigma$ is the Stefan-Boltzmann constant for phonons, which can be written as

$$\sigma = \frac{\pi^2}{40}\frac{k_B^4}{\hbar^3 v^2}. \tag{5.5}$$

Here $k_B$ is the Boltzmann constant, $\hbar = h/2\pi$ is the reduced Planck's constant, $v$ is the average sound velocity of the three acoustic branches (two transverse and one longitudinal mode) (Chen et

al. 2015). For silicon at room temperature, $L_{mfp}$ = 300 nm (Ju and Goodson 1999), $v$ = 2737 m/s (Chen et al. 2015), and $\sigma$ = 1020.23 W/m$^2$-K$^4$. Therefore, the heat flux obtained from the EPRT is 6.61×10$^{12}$ W/m$^2$, which is >100 times higher than that from NEMD. The remarkably lower heat flux obtained from NEMD indicates the significant impact of boundary reflection, which converts the ballistic phonon transport into a diffuse energy transfer. This boundary refection process increases the thermal resistance of the film, and in our case, the thermal resistance of the arm.

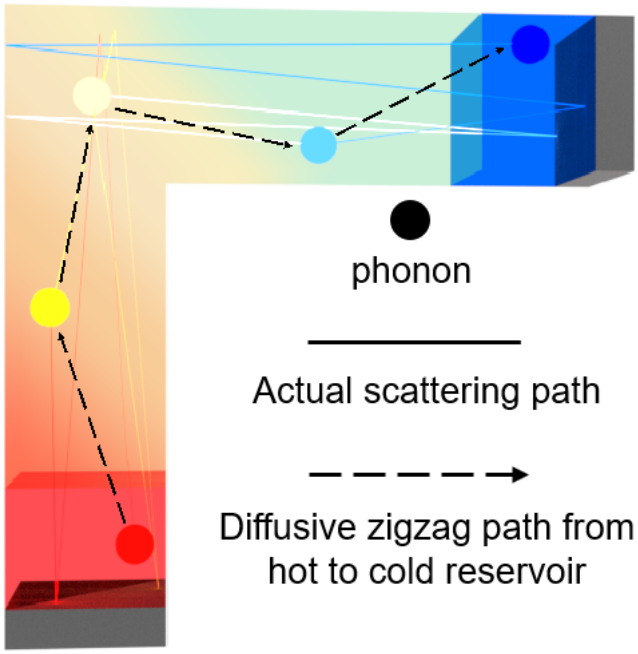


**Figure 5.4** Phonon transport route from the hot reservoir to the cold reservoir.

The dependence of the kink-induced resistance, $R_{kink\_ind}$, on the arm length is also related to phonon scattering in the kink. As schematically shown in **Figure 5.4**, the free boundaries of the kink backscatter the incoming phonons more into the arms that these phonons come from. Only when phonons are scattered in the kink and deflected into the opposite arm, they can carry energy to the opposite thermal reservoir. Therefore, the more often a phonon appears in the kink, the

higher possibility it is for the phonon to get scattered and deflected into the opposite arm. For shorter arm length cases, the chance for phonons travelling in the kink region is higher than that for larger arm length cases. Therefore, there is a higher probability for phonons to be scattered into the opposite arm for shorter arm length cases, which leads to a lower kink-induced resistance. Thus, as the arm length extends, the kink-induced resistance escalates, as shown in **Figure 5.2**.

## 5.5 Defect Effect on Phonon Transport in Kinked Silicon Nanowires

Based on the above analysis, we can expect that the thermal resistance of a kinked nanowire can be reduced via introducing defects in the kink because defects can enhance the probability of phonon scattering, facilitating phonons into the opposite arm. In fact, it has been experimentally demonstrated that for boron carbide nanowires (Zhang et al. 2017), instead of posing resistance to phonon transport, structural defects in the kink can actually reduce the kink resistance. Here we again use NEMD to confirm the above analysis by adding heavy isotopic atoms in the kink.

### 5.5.1 Simulation Model of Straight and Kinked Silicon Nanowires with Defects

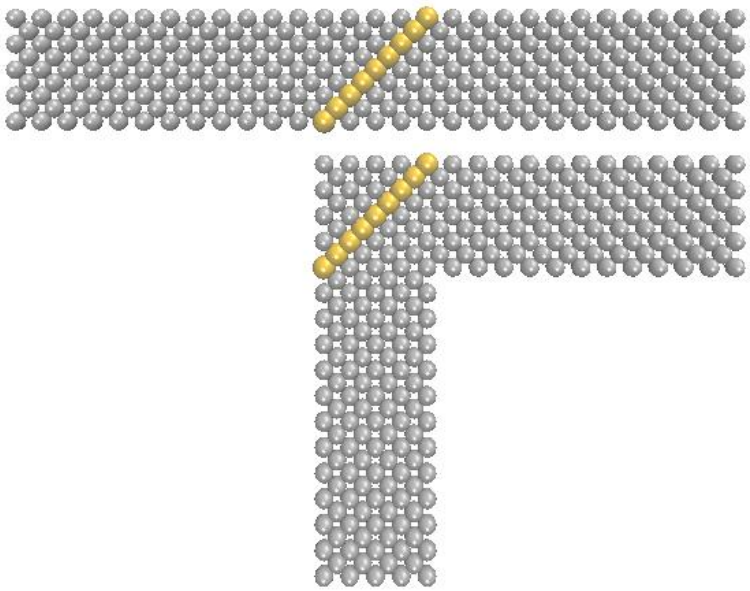

**Figure 5.5** Isotope-straight and isotope-kinked nanowires with the same arm length of 8 UC. The silver color represents $^{28}$Si atoms and the golden color represents $^{42}$Si atoms.

As shown in **Figure 5.5**, we replace the $^{28}$Si atoms with $^{42}$Si atoms at the diagonal plane in the kinked wire or the equivalent segment in the straight wire to introduce impurity defects with a rather large mass difference, while all other simulation parameters are kept the same. Since the number of the $^{42}$Si atoms in each nanowire is fixed, the impurity atom concentration reduces as the wire length increases with the values of 2.19%, 1.88%, 1.64%, and 1.46% for the 6, 8, 10, and 12 UC arm length cases.

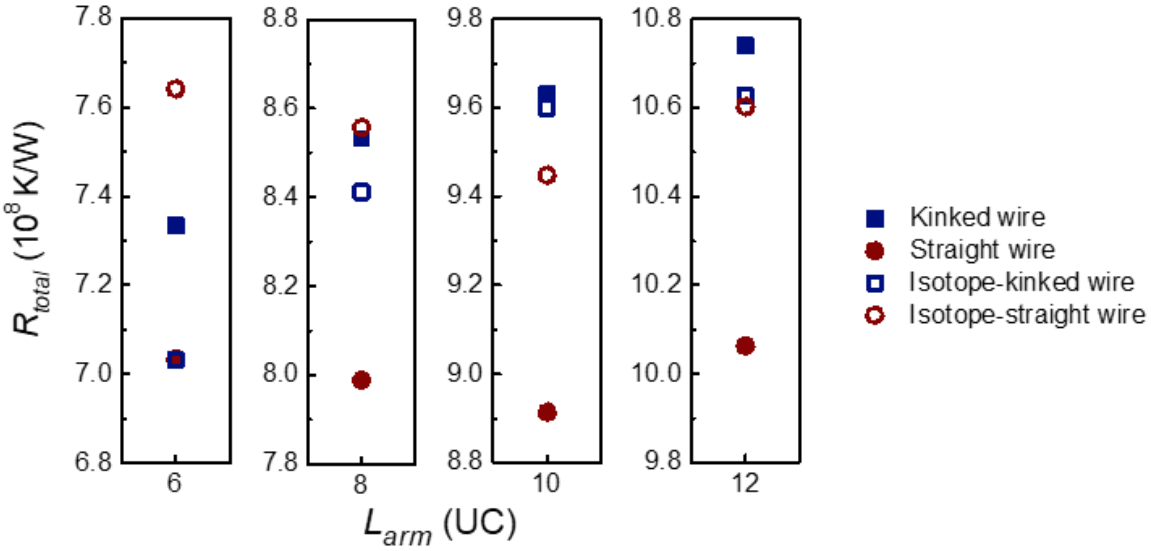


**Figure 5.6** Total thermal resistance of the kinked, straight, isotope-kinked and isotope-straight silicon nanowires.

**Figure 5.6** shows the total thermal resistance of the kinked, isotope-kinked, straight and isotope-straight nanowires with different arm lengths. For all four cases, the thermal resistance of the isotope-straight wire is higher than that of the isotope-free straight wire, consistent with the well-established physical picture that defects pose resistance to phonon transport (Asen-Palmer et al. 1997; Chen et al. 2012; Inyushkin et al. 2018; Ruf et al. 2000; Yang, Zhang, and Li 2008). As the nanowire length increases and the isotope concentration drops from 2.19% to 1.46%, the thermal resistance escalation reduces from 8.6% to 5.3%. Different from the straight-wire cases,

for kinked nanowires, the isotopic atoms in the kink lead to a reduced thermal resistance. This result is consistent with the experimental observation from the boron carbide nanowires (Zhang et al. 2017), again suggesting that phonon-scattering in the kink helps phonons to make the turn and facilitates thermal transport through the kink.

To further verify that the $^{42}$Si atoms behave as effective scattering centers for phonons, we calculated the phonon DOS of the $^{42}$Si atoms and their same-position $^{28}$Si atoms, which are shown in **Figure 5.7**. The results indicate that the phonon DOS of the $^{42}$Si and $^{28}$Si atoms only has marginal difference in the straight and kinked nanowires. However, the phonon DOS of the $^{42}$Si atoms clearly shifts to the lower frequency regime compared to that of $^{28}$Si atoms. This obvious mismatch of DOS gives rise to enhanced scattering when phonons encounter the isotopic atoms.

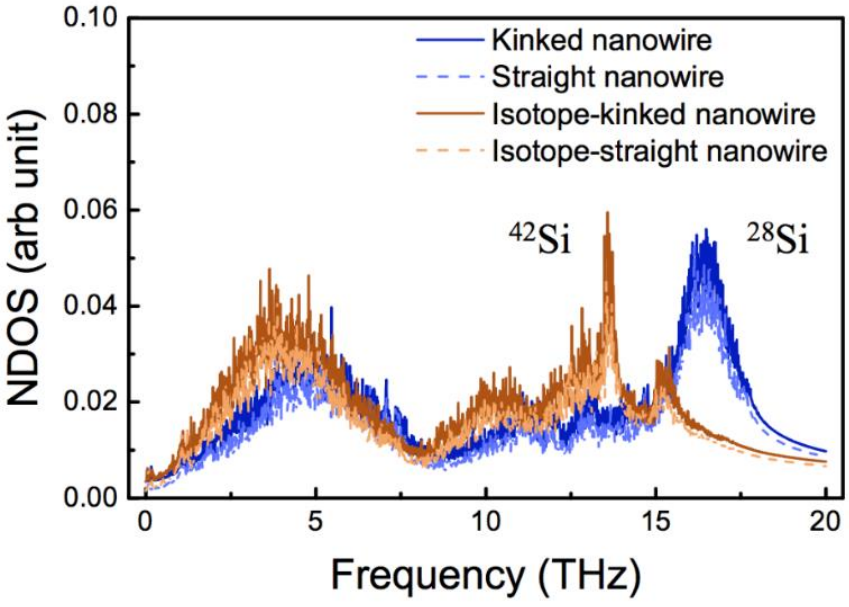


**Figure 5.7** Phonon DOS spectra of the $^{28}$Si and $^{42}$Si atoms.

### 5.5.2 Effect of Elastic Anisotropy on Phonon Transport in Kinked Nanowires

We note that the obtained kink resistance from the NEMD simulation is significantly lower than the experimentally extracted value for kinked boron carbide nanowires (Zhang et al. 2017).

The largest normalized kink-induced resistance for the case with an arm length of 12 UC is only ~0.6 times that of a straight wire segment of equivalent length, while for a ~80 nm diameter kinked boron carbide nanowire, the corresponding value is ~30. To verify that this large difference is indeed due to difference in materials instead of serious artificial effects in the NEMD simulation, we conducted experimental measurements of the thermal conductivity of straight and kinked silicon nanoribbons, which were fabricated using e-beam lithography (Yang et al. 2016). The measurement was done using the well-established micro-thermal bridge approach based on a microdevice with two side-by-side suspended membranes with integrated Pt coil serving as both resistance heaters and thermometers, as detailed in the literature (Shi et al. 2003; Wingert et al. 2012).

As shown in **Figure 5.8**, the thermal conductivity of a kinked silicon nanoribbon with a cross-sectional dimension of 33 nm thick and 138 nm wide is lower than that of a straight nanoribbon with a cross-section of 33 nm thick and 135 nm wide in the whole measurement temperature range of 30 K to 320 K. The difference at 300 K, 4.3% thermal conductivity drop, corresponds to an additional kink-induced resistance that is 1.08 times the resistance of a straight wire segment of equivalent length, if neglecting the tiny difference in the geometric dimensions of the straight and kinked nanoribbons. This value is much smaller than the ~30 times for kinked boron carbide nanowires but on the same order as our NEMD value of 0.6 times. The slightly smaller NEMD value could be attributed to the smaller system size in the simulation as the kink-induced resistance increases with the arm length in our MD results.

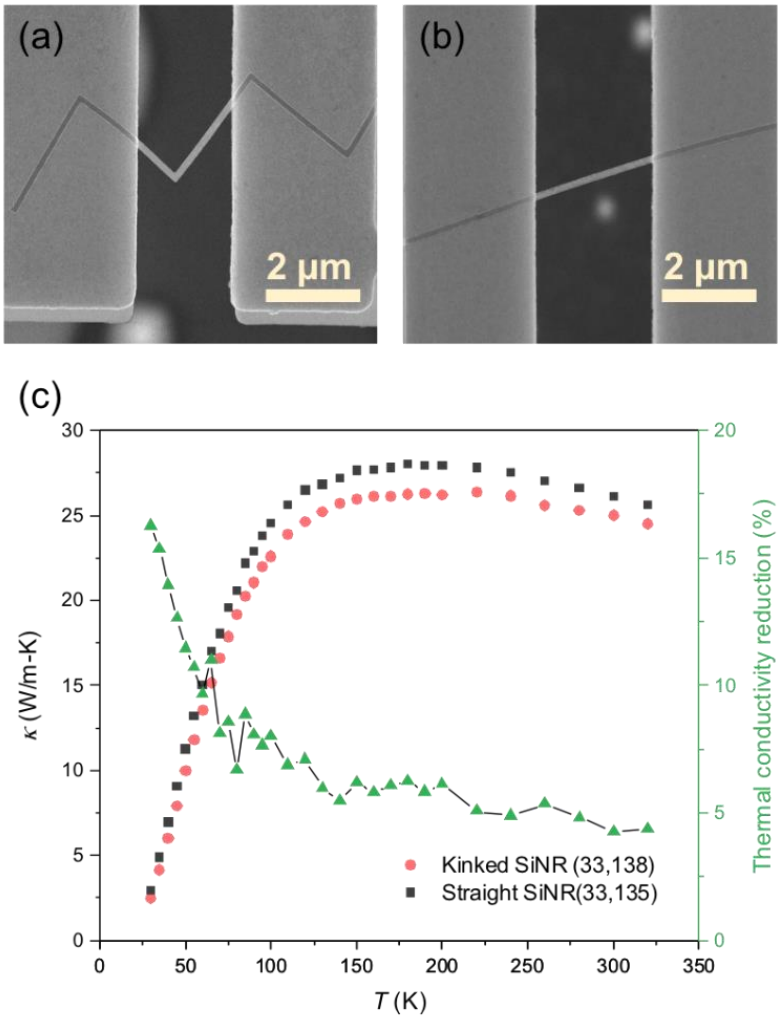


**Figure 5.8** Thermal conductivity of kinked and straight silicon nanoribbons. SEM micrographs of (a) a kinked and (b) a straight silicon nanoribbon with the suspended length as 3.28 μm and 3.25 μm, respectively. (c) Measured thermal conductivity and derived thermal conductivity reduction as a function of temperature.

Another way of measuring the kink-induced resistance is to solve for the kink resistance for unit area, as done for the kinked boron carbide nanowires (Zhang et al. 2017), which makes it convenient to compare with the widely encountered interfacial thermal resistance. The kink resistance for unit area for the NEMD simulation cases ranges from 3.73 to $4.15 \times 10^{-10}$ $m^2$-K/W as the arm length increases from 6 to 12 UC, which is one order of magnitude smaller than the value for the experimentally measured kinked silicon nanoribbon ($8.24 \times 10^{-9}$ $m^2$-K/W). Again, both the

MD simulation and experimental values are much smaller than that for the kinks in boron carbide nanowires, which is in the range of 1.59-5.20 $\times 10^{-7}$ $m^2$-K/W.

The very different kink effect on thermal transport in silicon and boron carbide nanowires can be attributed to the different level of elastic anisotropy for silicon and boron carbides. In silicon the lowest Young's module exists along the <100> direction and the highest value is along the <111> direction, which are 130 GPa and 188 GPa, respectively (Zhang et al. 2011). According to Ledbetter and Migliori (Ledbetter and Migliori 2006), an elastic anisotropy index can be defined as the ratio of the largest Young's modulus over the smallest, which yields a value of 1.45 for silicon. For boron carbide the elastic moduli range from 64 GPa to 522 GPa (Clellan et al. 2001), which corresponds to an elastic anisotropy index of ~8.16. This significant difference in the elastic anisotropy, while not changing the fundamental mechanism of how the kink induces additional thermal resistance, results in large discrepancy in the observed kink resistance. For highly anisotropic boron carbides, the elastic anisotropy leads to strong phonon focusing that aligns phonons along the nanowire axis direction, which helps to reduce the thermal resistance of straight nanowires while boost the kink resistance by back-reflection of highly aligned incoming phonons. On the other hand, silicon only has a low level of elastic anisotropy, and hence rather weak phonon focusing effects (Karamitaheri et al. 2013), which corresponds to a rather weak kink effect on thermal transport in kink nanowires, as demonstrated both numerically and experimentally.

**5.6 Summary**

In summary, we conducted NEMD simulations to study the thermal transport properties in kinked silicon nanowires. The results show that the kink can pose 1.6 times thermal resistance compared to a corresponding wire segment of equivalent length for an arm length of 12 UC. The detailed temperature profile suggests that kinks induce additional thermal resistance through

reflecting phonons back into their incoming arms. Our simulations also recapture the interesting observation that defects in the kink, instead of posing additional resistance, actually facilitate phonon transmission through the kink. Given that the kink morphology is a common wire configuration in electronic devices, the detailed physical picture presented here should help to improve the thermal design of nanoelectronic devices.

# Chapter 6

## Summary

Compared to the extensive studies on individual nanostructures, relatively few research efforts have been devoted into the contacts between nanostructures due to the tremendous challenges involved in experiments. With the thermal-bridge platform and MD simulation approach, we could provide understandings on thermal and electrical transport mechanisms at contacts and kinks of nanowires. Our findings are summarized in this chapter.

Through systematic measurements of silver nanowires of different sizes and their contacts, we show that the effective Lorenz number increases with decreasing wire diameter and has a higher value at wire contacts. Examination of the corresponding electrical and thermal conductivities of silver nanowires indicates that the escalating Lorenz number in smaller wires are due to contributions of phonons that become more important as a result of elastic stiffening. The derived contact thermal conductance per unit area between two silver nanowires is ~10 times that between carbon nanotubes, indicating that silver nanowires could be more effective nanofillers to enhance thermal performance of nanocomposites. The effective Lorenz number of the point contact between silver nanowires significantly deviates from the Sommerfeld value and exhibits non-monotonic variation with temperature. Analyses show that these observations are due to the more important phonon contribution to the thermal conductance at the contact as Sharvin resistance greatly hinders electron transport, which is further confirmed by the size dependence of contact Lorenz number with a higher value for a smaller contact size.

The contact effect on electrical transport is of great importance for CNT-based devices. Through conducting measurements on the contact and single CNTs, we study the electrical and thermoelectric transport properties at an individual contact level. The temperature dependence of

the derived electrical resistance and Seebeck coefficient of the point contact can be well fitted with Mott's 3D VRH model, providing experimental evidence for the electron hopping conduction mechanism at contacts between CNTs. More importantly, the electron hopping conduction at contacts could induce significantly enhanced positive Seebeck coefficient and lead to the higher overall thermoelectric figure of merit.

To disclose the details of phonon transport in kinked nanowires, we apply NEMD simulations to study thermal transport through kinked and straight silicon nanowires. Results show that kinks can induce additional resistance and lead to lower thermal conductivity for kinked nanowires than that of corresponding straight wires. Detailed analysis indicates that kinks produce additional resistance through reflecting phonons back into the arm where they come from. Moreover, through introducing heavier isotope atoms in the kink region, the simulation replicates the experimental observation that defects in the kink regime, instead of posing additional resistance, can actually facilitate thermal transport through the kink by deflecting phonons into the opposite arm.

## Reference


Aggarwal, M., S. Khan, M. Husain, T. C. Ming, M. Y. Tsai, T. P. Perng, and Z. H. Khan. 2007. "Variable-Range Hopping in $Fe_{70}Pt_{30}$ Catalyzed Multi-Walled Carbon Nanotubes Film." *European Physical Journal B* 60(3):319–324.

Alaie, Seyedhamidreza, Drew F. Goettler, Mehmet Su, Zayd C. Leseman, Charles M. Reinke, and Ihab El-Kady. 2015. "Thermal Transport in Phononic Crystals and the Observation of Coherent Phonon Scattering at Room Temperature." *Nature Communications* 6(1):7228.

Anufriev, Roman, and Masahiro Nomura. 2015. "Thermal Conductance Boost in Phononic Crystal Nanostructures." *Physical Review B - Condensed Matter and Materials Physics* 91(24):2–5.

Asen-Palmer, M., K. Bartkowski, E. Gmelin, M. Cardona, A. Zhernov, A. Inyushkin, A. Taldenkov, and V. Ozhogin. 1997. "Thermal Conductivity of Germanium Crystals with Different Isotopic Compositions." *Physical Review B - Condensed Matter and Materials Physics* 56(15):9431–9447.

Ashcroft, Neil W., and N.David Mermin. 1976. *Solid State Physics*. Harcourt College Publishers: Fort Worth, TX.

Asheghi, M., K. Kurabayashi, R. Kasnavi, and K. E. Goodson. 2002. "Thermal Conduction in Doped Single-Crystal Silicon Films." *Journal of Applied Physics* 91(8):5079–5088.

Bandow, Shunji, Shigenori Numao, and Sumio Iijima. 2007. "Variable-Range Hopping Conduction in the Assembly of Boron-Doped Multiwalled Carbon Nanotubes." *The Journal of Physical Chemistry C* 111(32):11763–11766.

Baxendale, M., K. G. Lim, and G. A. J. Amaratunga. 2000. "Thermoelectric Power of Aligned and Randomly Oriented Carbon Nanotubes." *Physical Review B* 61(19):12705–12708.

Bellew, Allen T., Hugh G. Manning, Claudia Gomes da Rocha, Mauro S. Ferreira, and John J. Boland. 2015. "Resistance of Single Ag Nanowire Junctions and Their Role in the Conductivity of Nanowire Networks." *ACS Nano* 9(11):11422–11429.

Benoit, J. M., B. Corraze, and O. Chauvet. 2002. "Localization, Coulomb Interactions, and Electrical Heating in Single-Wall Carbon Nanotubes/polymer Composites." *Physical Review B - Condensed Matter and Materials Physics* 65(24):241405.

Bifano, Michael F. P., Jungkyu Park, Pankaj B. Kaul, Ajit K. Roy, and Vikas Prakash. 2012. "Effects of Heat Treatment and Contact Resistance on the Thermal Conductivity of Individual Multiwalled Carbon Nanotubes Using a Wollaston Wire Thermal Probe." *Journal of Applied Physics* 111(5):54321.

Blackburn, Jeffrey L., Teresa M. Barnes, Matthew C. Beard, Yong Hyun Kim, Robert C. Tenent, Timothy J. McDonald, Bobby To, Timothy J. Coutts, and Michael J. Heben. 2008. "Transparent Conductive Single-Walled Carbon Nanotube Networks with Precisely Tunable Ratios of Semiconducting and Metallic Nanotubes." *ACS Nano* 2(6):1266–1274.

Boukai, Akram I., Yuri Bunimovich, Jamil Tahir-Kheli, Jen Kan Yu, William A. Goddard, and James R. Heath. 2008. "Silicon Nanowires as Efficient Thermoelectric Materials." *Nature* 451(7175):168–171.

Bürkle, Marius, and Yoshihiro Asai. 2018. "How to Probe the Limits of the Wiedemann-Franz Law at Nanoscale." *Nano Letters* 18(11):7358–7361.

Cahill, David G., Paul V. Braun, Gang Chen, David R. Clarke, Shanhui Fan, Kenneth E. Goodson, Pawel Keblinski, William P. King, Gerald D. Mahan, Arun Majumdar, Humphrey J. Maris, Simon R. Phillpot, Eric Pop, and Li Shi. 2014. "Nanoscale Thermal Transport. II. 2003-2012." *Applied Physics Reviews* 1(1):011305.

Chang, Tzu-Hsuan, Guangming Cheng, Chengjun Li, and Yong Zhu. 2016. "On the Size-Dependent Elasticity of Penta-Twinned Silver Nanowires." *Extreme Mechanics Letters* 8:177–183.

Chen, Renkun, Allon I. Hochbaum, Padraig Murphy, Joel Moore, Peidong Yang, and Arun Majumdar. 2008. "Thermal Conductance of Thin Silicon Nanowires." *Physical Review Letters* 101(10):105501.

Chen, Renkun, Jaeho Lee, Woochul Lee, and Deyu Li. 2019. "Thermoelectrics of Nanowires." *Chemical Reviews*119(15):9260-9302

Chen, Shanshan, Qingzhi Wu, Columbia Mishra, Junyong Kang, Hengji Zhang, Kyeongjae Cho, Weiwei Cai, Alexander A. Balandin, and Rodney S. Ruoff. 2012. "Thermal Conductivity of Isotopically Modified Graphene." *Nature Materials* 11(3):203–207.

Chen, Weiyu, Juekuan Yang, Zhiyong Wei, Chenhan Liu, Kedong Bi, Dongyan Xu, Deyu Li, and Yunfei Chen. 2015. "Effects of Interfacial Roughness on Phonon Transport in Bilayer Silicon Thin Films." *Physical Review B - Condensed Matter and Materials Physics* 92(13):134113.

Cheng, Zhe, Longju Liu, Shen Xu, Meng Lu, and Xinwei Wang. 2015. "Temperature Dependence of Electrical and Thermal Conduction in Single Silver Nanowire." *Scientific Reports* 5(1):10718.

Cho, Seungse, Saewon Kang, Ashish Pandya, Ravi Shanker, Ziyauddin Khan, Youngsu Lee, Jonghwa Park, Stephen L. Craig, and Hyunhyub Ko. 2017. "Large-Area Cross-Aligned Silver Nanowire Electrodes for Flexible, Transparent, and Force-Sensitive Mechanochromic Touch Screens." *ACS Nano* 11(4):4346–4357.

Choi, Y. M., D. S. Lee, R. Czerw, P. W. Chiu, N. Grobert, M. Terrones, M. Reyes-Reyes, H. Terrones, J. C. Charlier, P. M. Ajayan, S. Roth, D. L. Carroll, and Y. W. Park. 2003a. "Nonlinear Behavior in the Thermopower of Doped Carbon Nanotubes Due to Strong, Localized States." *Nano Letters* 3(6):839–842.

Chowdhury, Ihtesham, Ravi Prasher, Kelly Lofgreen, Gregory Chrysler, Sridhar Narasimhan, Ravi Mahajan, David Koester, Randall Alley, and Rama Venkatasubramanian. 2009. "On-Chip Cooling by Superlattice-Based Thin-Film Thermoelectrics." *Nature Nanotechnology* 4(4):235–238.

Clellan, K. J. M. C., F. Chu, and J. M. Roper. 2001. "Room Temperature Single Crystal Elastic Constants of Boron Carbide." *Journal of Materials Science* 6(8 mm):3403–3407.

Cuenot, Stéphane, Christian Frétigny, Sophie Demoustier-Champagne, and Bernard Nysten. 2004. "Surface Tension Effect on the Mechanical Properties of Nanomaterials Measured by Atomic Force Microscopy." *Physical Review B* 69(16):165410.

Cuffe, John, Emigdio Chávez, Andrey Shchepetov, Pierre Olivier Chapuis, El Houssaine El Boudouti, Francesc Alzina, Timothy Kehoe, Jordi Gomis-Bresco, Damian Dudek, Yan Pennec, Bahram Djafari-Rouhani, Mika Prunnila, Jouni Ahopelto, and Clivia M. Sotomayor Torres. 2012. "Phonons in Slow Motion: Dispersion Relations in Ultrathin Si Membranes." *Nano Letters* 12(7):3569–3573.

Cui, Longji, Wonho Jeong, Sunghoon Hur, Manuel Matt, Jan C. Klöckner, Fabian Pauly, Peter Nielaba, Juan Carlos Cuevas, Edgar Meyhofer, and Pramod Reddy. 2017. "Quantized Thermal Transport in Single-Atom Junctions." *Science* 355(6330):1192–1195.

Dechaumphai, Edward, and Renkun Chen. 2012. "Thermal Transport in Phononic Crystals: The Role of Zone Folding Effect." *Journal of Applied Physics* 111(7):073508.

Doerk, Gregory S., Carlo Carraro, and Roya Maboudian. 2010. "Single Nanowire Thermal Conductivity Measurements by Raman Thermography." *ACS Nano* 4(8):4908–4914.

Du, Yong, Shirley Z. Shen, Weidong Yang, Richard Donelson, Kefeng Cai, and Philip S. Casey. 2012. “Simultaneous Increase in Conductivity and Seebeck Coefficient in a Polyaniline/graphene Nanosheets Thermoelectric Nanocomposite.” *Synthetic Metals* 161(23–24):2688–2692.

Ebbesen, T. W., H. J. Lezec, H. Hiura, J. W. Bennett, H. F. Ghaemi, and T. Thio. 1996. “Electrical Conductivity of Individual Carbon Nanotubes.” *Nature* 382(6586):54–56.

Efros, A. L., and B. I. Shklovskii. 1975. “Coulomb Gap and Low Temperature Conductivity of Disordered Systems.” *Journal of Physics C: Solid State Physics* 8(4):L49-L51.

Estrada, David, and Eric Pop. 2011. “Imaging Dissipation and Hot Spots in Carbon Nanotube Network Transistors.” *Applied Physics Letters* 98(7):8–11.

Feng, Tianli, and Xiulin Ruan. 2016. “Ultra-Low Thermal Conductivity in Graphene Nanomesh.” *Carbon* 101:107–113.

Fischer, J. E., H. Dai, A. Thess, R. Lee, N. M. Hanjani, D. L. Dehaas, and R. E. Smalley. 1997. “Metallic Resistivity in Crystalline Ropes of Single-Wall Carbon Nanotubes.” *Physical Review B* 55(8):4921–4924.

Fu, Qiang, Juekuan Yang, Yunfei Chen, Deyu Li, and Dongyan Xu. 2015. “Experimental Evidence of Very Long Intrinsic Phonon Mean Free Path along the c -Axis of Graphite.” *Applied Physics Letters* 106(3):031905.

Fuhrer, M. S., W. Holmes, P. L. Richards, P. Delaney, S. G. Louie, and A. Zettl. 1999. “Nonlinear Transport and Localization in Single-Walled Carbon Nanotubes.” *Synthetic Metals* 103(1–3):2529–2532.

Fuhrer, M. S., J. Nygård, L. Shih, M. Forero, Young-Gui Yoon, M. S. C. Mazzoni, Hyoung Joon Choi, Jisoon Ihm, Steven G. Louie, A. Zettl, and Paul L. McEuen1. 2000. “Crossed Nanotube Junctions.” *Science* 288(5465):494–497.

Gaál, R., J. Salvetat, and L. Forró. 2000. “Pressure Dependence of the Resistivity of Single-Wall Carbon Nanotube Ropes.” *Physical Review B - Condensed Matter and Materials Physics* 61(11):7320–7323.

Guan, Zhe, Timothy Gutu, Juekuan Yang, Yang Yang, Alfred A. Zinn, Deyu Li, and Terry T. Xu. 2012. “Boron Carbide Nanowires: Low Temperature Synthesis and Structural and Thermal Conductivity Characterization.” *Journal of Materials Chemistry* 22(19):9853-9860.

Gundrum, Bryan C., David G. Cahill, and Robert S. Averback. 2005. “Thermal Conductance of Metal-Metal Interfaces.” *Physical Review B* 72(24):245426.

Hasegawa, Yasuhiro, Masayuki Murata, Fumiaki Tsunemi, Yusuke Saito, Katsuhito Shirota, Takashi Komine, Chris Dames, and Javier E. Garay. 2013. “Thermal Conductivity of an Individual Bismuth Nanowire Covered with a Quartz Template Using a 3-Omega Technique.” *Journal of Electronic Materials* 42(7):2048–2055.

He, Gui-Cang, Xian-Zi Dong, Jie Liu, Heng Lu, and Zhen-Sheng Zhao. 2018. “Investigate the Electrical and Thermal Properties of the Low Temperature Resistant Silver Nanowire Fabricated by Two-Beam Laser Technique.” *Applied Surface Science* 439:96–100.

He, Gui-Cang, Heng Lu, Xian-Zi Dong, Yong-Liang Zhang, Jie Liu, Chang-Qing Xie, and Zhen-Sheng Zhao. 2018. “Electrical and Thermal Properties of Silver Nanowire Fabricated on a Flexible Substrate by Two-Beam Laser Direct Writing for Designing a Thermometer.” *RSC Advances* 8(44):24893–24899.

De Heer, Walt A., W. S. Bacsa, A. Châtelain, T. Gerfin, R. Humphrey-Baker, L. Forro, and D. Ugarte. 1995. “Aligned Carbon Nanotube Films: Production and Optical and Electronic Properties.” *Science* 268(5212):845–847.

Hewitt, C. A., A. B. Kaiser, S. Roth, M. Craps, R. Czerw, and D. L. Carroll. 2011. "Varying the Concentration of Single Walled Carbon Nanotubes in Thin Film Polymer Composites, and Its Effect on Thermoelectric Power." *Applied Physics Letters* 98(18):183110.

Hewitt, Corey A., Alan B. Kaiser, Siegmar Roth, Matt Craps, Richard Czerw, and David L. Carroll. 2012. "Multilayered Carbon Nanotube/polymer Composite Based Thermoelectric Fabrics." *Nano Letters* 12(3):1307–1310.

Ho, C. Y., R. W. Powell, and P. E. Liley. 1972. "Thermal Conductivity of the Elements." *Journal of Physical and Chemical Reference Data* 1(2):279–421.

Hochbaum, Allon I., Renkun Chen, Raul Diaz Delgado, Wenjie Liang, Erik C. Garnett, Mark Najarian, Arun Majumdar, and Peidong Yang. 2008. "Enhanced Thermoelectric Performance of Rough Silicon Nanowires." *Nature* 451(7175):163–167.

Hopkins, Patrick E., Charles M. Reinke, Mehmet F. Su, Roy H. Olsson, Eric A. Shaner, Zayd C. Leseman, Justin R. Serrano, Leslie M. Phinney, and Ihab El-Kady. 2011. "Reduction in the Thermal Conductivity of Single Crystalline Silicon by Phononic Crystal Patterning." *Nano Letters* 11(1):107–112.

Hsu, Po-Chun, Xiaoge Liu, Chong Liu, Xing Xie, Hye Ryoung Lee, Alex J. Welch, Tom Zhao, and Yi Cui. 2015. "Personal Thermal Management by Metallic Nanowire-Coated Textile." *Nano Letters* 15(1):365–371.

Huang, By Hua, Changhong Liu, Yang Wu, and Shoushan Fan. 2005. "Aligned Carbon Nanotube Composite Films for Thermal Management." *Advanced Materials* 17(13):1652–1656.

Huxtable, Scott T., David G. Cahill, Sergei Shenogin, Liping Xue, Rahmi Ozisik, Paul Barone, Monica Usrey, Michael S. Strano, Giles Siddons, Moonsub Shim, and Pawel Keblinski. 2003. "Interfacial Heat Flow in Carbon Nanotube Suspensions." *Nature Materials* 2(11):731–734.

Inyushkin, Alexander V., Alexander N. Taldenkov, Joel W. Ager, Eugene E. Haller, Helge Riemann, Nikolay V. Abrosimov, Hans-Joachim Pohl, and Peter Becker. 2018. "Ultrahigh Thermal Conductivity of Isotopically Enriched Silicon." *Journal of Applied Physics* 123(9):95112.

Jain, Ankit, and Alan J. H. McGaughey. 2016. "Thermal Transport by Phonons and Electrons in Aluminum, Silver, and Gold from First Principles." *Physical Review B* 93(8):81206.

Jain, Ankit, Ying Ju Yu, and Alan J. H. McGaughey. 2013. "Phonon Transport in Periodic Silicon Nanoporous Films with Feature Sizes Greater than 100 nm." *Physical Review B - Condensed Matter and Materials Physics* 87(19):195301.

Jauregui, Luis A., Yanan Yue, Anton N. Sidorov, Jiuning Hu, Qingkai Yu, Gabriel Lopez, Romaneh Jalilian, Daniel K. Benjamin, Derek A. Delkd, Wei Wu, Zhihong Liu, Xinwei Wang, Zhigang Jiang, Xiulin Ruan, Jiming Bao, Steven S. Pei, and Yong P. Chen. 2010. "Thermal Transport in Graphene Nanostructures: Experiments and Simulations." *ECS Transactions* 28(5):73–83.

Jiang, Jin Wu, Nuo Yang, Bing Shen Wang, and Timon Rabczuk. 2013. "Modulation of Thermal Conductivity in Kinked Silicon Nanowires: Phonon Interchanging and Pinching Effects." *Nano Letters* 13(4):1670–1674.

Jing, G. Y., H. L. Duan, X. M. Sun, Z. S. Zhang, J. Xu, Y. D. Li, J. X. Wang, and D. P. Yu. 2006. "Surface Effects on Elastic Properties of Silver Nanowires: Contact Atomic-Force Microscopy." *Physical Review B* 73(23):235409.

Jouni, Mohammad, David Djurado, Valérie Massardier, and Gisèle Boiteux. 2017. "A Representative and Comprehensive Review of the Electrical and Thermal Properties of Polymer Composites with Carbon Nanotube and Other Nanoparticle Fillers." *Polymer*

*International* 66(9):1237–1251.
Ju, Y. S., and K. E. Goodson. 1999. "Phonon Scattering in Silicon Films with Thickness of Order 100 Nm." *Applied Physics Letters* 74(20):3005–3007.
Kaiser, A. B. 1989. "Thermoelectric Power and Conductivity of Heterogeneous Conducting Polymers." *Physical Review B* 40(5):2806–2813.
Kaiser, A. B., Y. W. Park, G. T. Kim, E. S. Choi, G. Düsberg, and S. Roth. 1999. "Electronic Transport in Carbon Nanotube Ropes and Mats." *Synthetic Metals* 103(1–3):2547–2550.
Kang, Saewon, Taehyo Kim, Seungse Cho, Youngoh Lee, Ayoung Choe, Bright Walker, Seo-Jin Ko, Jin Young Kim, and Hyunhyub Ko. 2015. "Capillary Printing of Highly Aligned Silver Nanowire Transparent Electrodes for High-Performance Optoelectronic Devices." *Nano Letters* 15(12):7933–7942.
Karamitaheri, Hossein, Neophytos Neophytou, and Hans Kosina. 2013. "Ballistic Phonon Transport in Ultra-Thin Silicon Layers: Effects of Confinement and Orientation." *Journal of Applied Physics* 113(20):204305.
Kilbride, B. E., J. N. Coleman, J. Fraysse, P. Fournet, M. Cadek, A. Drury, S. Hutzler, S. Roth, and W. J. Blau. 2002. "Experimental Observation of Scaling Laws for Alternating Current and Direct Current Conductivity in Polymer-Carbon Nanotube Composite Thin Films." *Journal of Applied Physics* 92(7):4024–4030.
Kim, E. K., S. I. Kwun, S. M. Lee, H. Seo, and J. G. Yoon. 2000. "Thermal Boundary Resistance at Ge2Sb2Te5/ZnS:SiO2 Interface." *Applied Physics Letters* 76(26):3864–3866.
Kim, P., L. Shi, A. Majumdar, and P. L. McEuen. 2001. "Thermal Transport Measurements of Individual Multiwalled Nanotubes." *Physical Review Letters* 87(21):215502.
Kirkpatrick, Scott. 1973. "Percolation and Conduction." *Reviews of Modern Physics* 45(4):574–588.
Kittel, Charles. 2004. *Introduction to Solid State Physics*. 8th editio. Wiley, New York.
Klöckner, J. C., M. Matt, P. Nielaba, F. Pauly, and J. C. Cuevas. 2017. "Thermal Conductance of Metallic Atomic-Size Contacts: Phonon Transport and Wiedemann-Franz Law." *Physical Review B* 96(20):205405.
Kojda, D., R. Mitdank, M. Handwerg, A. Mogilatenko, M. Albrecht, Z. Wang, J. Ruhhammer, M. Kroener, P. Woias, and S. F. Fischer. 2015. "Temperature-Dependent Thermoelectric Properties of Individual Silver Nanowires." *Physical Review B* 91(2):024302.
Ledbetter, Hassel, and Albert Migliori. 2006. "A General Elastic-Anisotropy Measure." *Journal of Applied Physics* 100(6):63516.
Lee, Jaeho, Woochul Lee, Jongwoo Lim, Yi Yu, Qiao Kong, Jeffrey J. Urban, and Peidong Yang. 2016. "Thermal Transport in Silicon Nanowires at High Temperature up to 700 K." *Nano Letters* 16(7):4133–4140.
Lee, Jaeho, Woochul Lee, Geoff Wehmeyer, Scott Dhuey, Deirdre L. Olynick, Stefano Cabrini, Chris Dames, Jeffrey J. Urban, and Peidong Yang. 2017. "Investigation of Phonon Coherence and Backscattering Using Silicon Nanomeshes." *Nature Communications* 8(1):14054.
Lee, Seung Yong, Mi Ri Lee, No Won Park, Gil Sung Kim, Heon Jin Choi, Tae Youl Choi, and Sang Kwon Lee. 2013. "Temperature-Dependent Thermal Conductivities of 1D Semiconducting Nanowires via Four-Point-Probe 3-ω Method." *Nanotechnology* 24(49):495202.
Lee, Yun Hi, Dong Ho Kim, Hoon Kim, and Byeong Kwon Ju. 2000. "Carrier Transport and Electron Field-Emission Properties of a Nonaligned Carbon Nanotube Thick Film Mixed with Conductive Epoxy." *Journal of Applied Physics* 88(7):4181–4185.

Li, Chunyu, Erik T. Thostenson, and Tsu Wei Chou. 2007. “Dominant Role of Tunneling Resistance in the Electrical Conductivity of Carbon Nanotube-Based Composites.” *Applied Physics Letters* 91(22):223114.

Li, Deyu, Scott T. Huxtable, Alexis R. Abramson, and Arun Majumdar. 2005. “Thermal Transport in Nanostructured Solid-State Cooling Devices.” *Journal of Heat Transfer* 127(1):108-114.

Li, Deyu, and Alan J. H. McGaughey. 2015. “Phonon Dynamics at Surfaces and Interfaces and Its Implications in Energy Transport in Nanostructured Materials – An Opinion Paper.” *Nanoscale and Microscale Thermophysical Engineering* 19(2):166-182.

Li, Deyu, Yiying Wu, Philip Kim, Li Shi, Peidong Yang, and Arun Majumdar. 2003. “Thermal Conductivity of Individual Silicon Nanowires.” *Applied Physics Letters* 83(14):2934–2936.

Li, Li, Zhibin Yang, Hongjian Gao, Hui Zhang, Jin Ren, Xuemei Sun, Tao Chen, Hamid G. Kia, and Huisheng Peng. 2011. “Vertically Aligned and Penetrated Carbon Nanotube / Polymer Composite Film and Promising Electronic Applications.” *Advanced Materials* 23(32):3730–3735.

Lim, Jongwoo, Kedar Hippalgaonkar, Sean C. Andrews, Arun Majumdar, and Peidong Yang. 2012. “Quantifying Surface Roughness Effects on Phonon Transport in Silicon Nanowires.” *Nano Letters* 12(5):2475–2482.

Lim, Jongwoo, Hung Ta Wang, Jinyao Tang, Sean C. Andrews, Hongyun So, Jaeho Lee, Dong Hyun Lee, Thomas P. Russell, and Peidong Yang. 2016. “Simultaneous Thermoelectric Property Measurement and Incoherent Phonon Transport in Holey Silicon.” *ACS Nano* 10(1):124–132.

Logakis, E., Ch Pandis, V. Peoglos, P. Pissis, J. Pionteck, P. Pötschke, M. Mičušík, and M. Omastová. 2009. “Electrical/dielectric Properties and Conduction Mechanism in Melt Processed Polyamide/multi-Walled Carbon Nanotubes Composites.” *Polymer* 50(21):5103–5111.

Long, Yunze, Jean Luc Duvail, MengMeng Li, Changzhi Gu, Zongwen Liu, and Simon P. Ringer. 2010. “Electrical Conductivity Studies on Individual Conjugated Polymer Nanowires : Two-Probe and Four-Probe Results.” *Nanoscale Research Letters* 5(1:)237–242.

Ruf, T., R.W. Henna, M. Asen-Palmera, E. Gmelina, M. Cardonaa, H.-J. Pohlb, G. G. Devyatychc, P.G. Sennikov. 2000. “Thermal Conductivity of Isotopically Enriched Silicon.” *Solid State Commun* 115(5):243–247.

Luo, Tengfei, and Gang Chen. 2013. “Nanoscale Heat Transfer – from Computation to Experiment.” *Physical Chemistry Chemical Physics* 15(10):3389-3412.

Mahmoodi, Mehdi, Mohammad Arjmand, Uttandaraman Sundararaj, and Simon Park. 2011. “The Electrical Conductivity and Electromagnetic Interference Shielding of Injection Molded Multi-Walled Carbon Nanotube / Polystyrene Composites.” *Carbon* 50(4):1455–1464.

Maire, Jeremie, Roman Anufriev, Takuma Hori, Junichiro Shiomi, Sebastian Volz, and Masahiro Nomura. 2018. “Thermal Conductivity Reduction in Silicon Fishbone Nanowires.” *Scientific Reports* 8(1):4452.

Maire, Jeremie, and Masahiro Nomura. 2014. “Reduced Thermal Conductivities of Si One-Dimensional Periodic Structure and Nanowire.” *Japanese Journal of Applied Physics* 53(6S):06JE09.

Majumdar, A. 1993. “Microscale Heat Conduction in Dielectric Thin Films.” *Journal of Heat Transfer* 115(1):7-16.

Majumdar, Arun. 2004. “Thermoelectricity in Semiconductor Nanostructures.” *Science* 303(5659):777–778.

Matula, R. A. 1979. “Electrical Resistivity of Copper, Gold, Palladium, and Silver.” *Journal of Physical and Chemical Reference Data* 8(4):1147–1298.

Mavrokefalos, Anastassios, Michael T. Pettes, Feng Zhou, and Li Shi. 2007. “Four-Probe Measurements of the in-Plane Thermoelectric Properties of Nanofilms.” *Review of Scientific Instruments* 78(3):034901.

Maxwell, James Clerk. 1892. *A Treatise on Electricity and Magnetism*. Vol. 7. Cambridge: Cambridge University Press.

Meng, Chuizhou, Changhong Liu, and Shoushan Fan. 2010. “A Promising Approach to Enhanced Thermoelectric Properties Using Carbon Nanotube Networks.” *Advanced Materials* 22(4):535–539.

Menon, Reghu, and Vijayamohanan K. Pillai. 2012. “Charge Transport in Functionalized Multi-Wall Carbon Nanotube-Nafion Composite.” *Journal of Applied Physics* 112(5):53706.

Mingo, N. 2003. “Calculation of Si Nanowire Thermal Conductivity Using Complete Phonon Dispersion Relations.” *Physical Review B - Condensed Matter and Materials Physics* 68(11): 113308.

Mingo, Natalio, Liu Yang, Deyu Li, and Arun Majumdar. 2003. “Predicting the Thermal Conductivity of Si and Ge Nanowires.” *Nano Letters* 3(12):1713–1716.

Möhrle, D. O., F. Müller, M. Matt, P. Nielaba, and F. Pauly. 2019. “Statistical Analysis of Electronic and Phononic Transport Simulations of Metallic Atomic Contacts.” *Physical Review B* 100(12):125433.

Momose, Hisayo Sasaki, Tatsuya Ohguro, Kenji Kojima, Shin Ichi Nakamura, and Yoshiaki Toyoshima. 2003. “1.5-Nm Gate Oxide CMOS on (110) Surface-Oriented Si Substrate.” *IEEE Transactions on Electron Devices* 50(4):1001–1008.

Moore, Arden L., and Li Shi. 2011. “On Errors in Thermal Conductivity Measurements of Suspended and Supported Nanowires Using Micro-Thermometer Devices from Low to High Temperatures.” *Measurement Science and Technology* 22(1):015103.

Mosso, Nico, Ute Drechsler, Fabian Menges, Peter Nirmalraj, Siegfried Karg, Heike Riel, and Bernd Gotsmann. 2017. “Heat Transport through Atomic Contacts.” *Nature Nanotechnology* 12(5):430–433.

Mosso, Nico, Alyssa Prasmusinto, Andrea Gemma, Ute Drechsler, Lukas Novotny, and Bernd Gotsmann. 2019. “Quantized Thermal Conductance in Metallic Heterojunctions.” *Applied Physics letters* 114(12):123102.

Mott, N. F., and E. A. Davis. 1979. *Electronic Processes in Non-Crystalline Materials*. second edi. Oxford: Clarendon.

Niekiel, F.; Spiecker, E.; Bitzek, E. 2015. “Influence of Anisotropic Elasticity on the Mechanical Properties of Fivefold Twinned Nanowires. ” *Journal of the Mechanics and Physics of Solids* 84: 358−379.

Nomura, M., and J. Maire. 2015. “Mechanism of the Reduced Thermal Conductivity of Fishbone-Type Si Phononic Crystal Nanostructures.” *Journal of Electronic Materials* 44(6):1426–1431.

Ou, M. N., T. J. Yang, S. R. Harutyunyan, Y. Y. Chen, C. D. Chen, and S. J. Lai. 2008. “Electrical and Thermal Transport in Single Nickel Nanowire.” *Applied Physics Letters* 92(6):63101.

Paulson, S., A. Helser, M.Buongiorno Nardelli, R. M.Taylor II, M. Falvo, R. Superfine, and S. Washburn. 2000. “Tunable Resistance of a Carbon Nanotube-Graphite Interface.” *Science* 290(5497):1742–1744.

Pop, Eric, David Mann, Qian Wang, Kenneth Goodson, and Hongjie Dai. 2006. “Thermal Conductance of an Individual Single-Wall Carbon Nanotube above Room Temperature.”

*Nano Letters* 6(1):96–100.
Postma, Henk W.Ch., Mark de Jonge, Zhen Yao, and Cees Dekker. 2000. "Electrical Transport through Carbon Nanotube Junctions Created by Mechanical Manipulation." *Physical Review B* 62(16):R10653–R10656.
Prasher, Ravi. 2005. "Predicting the Thermal Resistance of Nanosized Constrictions." 5(11):2155–2159.
Prasher, Ravi S., X. J. Hu, Y. Chalopin, Natalio Mingo, K. Lofgreen, S. Volz, F. Cleri, and Pawel Keblinski. 2009. "Turning Carbon Nanotubes from Exceptional Heat Conductors into Insulators." *Physical Review Letters* 102(10):105901.
Qiu, T. Q., and C. L. Tien. 1993. "Size Effects on Nonequilibrium Laser Heating of Metal Films." *Journal of Heat Transfer* 115(4):842–847.
R. G. Chambers. 1950. "The Conductivity of Thin Wires in a Magnetic Field." *Proceedings of the Royal Society of London. Series A. Mathematical and Physical Sciences* 202(1070):378–94.
Ravichandran, Navaneetha K., and Austin J. Minnich. 2014. "Coherent and Incoherent Thermal Transport in Nanomeshes." *Physical Review B - Condensed Matter and Materials Physics* 89(20):205432.
Romano, Mark S., Na Li, Dennis Antiohos, Joselito M. Razal, Andrew Nattestad, Stephen Beirne, Shaoli Fang, Yongsheng Chen, Rouhollah Jalili, Gordon G. Wallace, Ray Baughman, and Jun Chen. 2013. "Carbon Nanotube – Reduced Graphene Oxide Composites for Thermal Energy Harvesting Applications." *Advanced Materials* 25(45):6602–6606.
Sadeghian, Hamed, Hans Goosen, Andre Bossche, Barend Thijsse, and Fred Van Keulen. 2011. "On the Size-Dependent Elasticity of Silicon Nanocantilevers: Impact of Defects." *Journal of Physics D: Applied Physics* 44(7):072001.
Sadeghian, Hamed, Chung Kai Yang, Johannes F. L. Goosen, Andre Bossche, Urs Staufer, Paddy J. French, and Fred Van Keulen. 2010. "Effects of Size and Defects on the Elasticity of Silicon Nanocantilevers." *Journal of Micromechanics and Microengineering* 20(6):064012.
Sawtelle, S. D., and M. A. Reed. 2019. "Temperature-Dependent Thermal Conductivity and Suppressed Lorenz Number in Ultrathin Gold Nanowires." *Physical Review B* 99(5):54304.
Sharvin, Yu. V. 1965. "A Possible Method for Studying Fermi Surfaces." *Sov. Phys. JETP* 21:655.
Shi, Li. 2012. "Thermal and Thermoelectric Transport in Nanostructures and Low-Dimensional Systems." *Nanoscale and Microscale Thermophysical Engineering* 16(2):79–116.
Shi, Li, Deyu Li, Choongho Yu, Wanyoung Jang, Dohyung Kim, Zhen Yao, Philip Kim, and Arunava Majumdar. 2003. "Measuring Thermal and Thermoelectric Properties of One-Dimensional Nanostructures Using a Microfabricated Device." *Journal of Heat Transfer* 125(5):881-888.
Skákalová, V., A. B. Kaiser, Y. S. Woo, and S. Roth. 2006. "Electronic Transport in Carbon Nanotubes: From Individual Nanotubes to Thin and Thick Networks." *Physical Review B* 74(8):085403.
Sokhan, V. P., D. Nicholson, and N. Quirke. 2000. "Phonon Spectra in Model Carbon Nanotubes." *Journal of Chemical Physics* 113(5):2007–2015.
Song, Tze-Bin, Yu Chen, Choong-Heui Chung, Yang (Michael) Yang, Brion Bob, Hsin-Sheng Duan, Gang Li, King-Ning Tu, Yu Huang, and Yang Yang. 2014. "Nanoscale Joule Heating and Electromigration Enhanced Ripening of Silver Nanowire Contacts." *ACS Nano* 8(3):2804–2811.
Steinhögl, Werner, Günther Schindler, Gernot Steinlesberger, and Manfred Engelhardt. 2002. "Size-Dependent Resistivity of Metallic Wires in the Mesoscopic Range." *Physical Review*

*B* 66(7):75414.
Stillinger, Frank H., and Thomas A. Weber. 1985. "Computer Simulation of Local Order in Condensed Phases of Silicon." *Physical Review B* 31(8):5262–5271.
Stojanovic, N., D. H. S. Maithripala, J. M. Berg, and M. Holtz. 2010. "Thermal Conductivity in Metallic Nanostructures at High Temperature: Electrons, Phonons, and the Wiedemann-Franz Law." *Physical Review B* 82(7):75418.
Sundaray, Bibekananda, Ajeong Choi, and Yung Woo Park. 2010. "Highly Conducting Electrospun Polyaniline-Polyethylene Oxide Nanofibrous Membranes Filled with Single-Walled Carbon Nanotubes." *Synthetic Metals* 160(9–10):984–988.
Tian, Mingliang, Lin Chen, Fanqing Li, Ruiping Wang, Zhiqiang Mao, Yuheng Zhang, and Hisashi Sekine. 1997. "Thermoelectric Power Properties of Graphitic Nanotubule Bundles." *Journal of Applied Physics* 82(6):3164–3166.
Tian, Zhiting, Sangyeop Lee, and Gang Chen. 2013. "Heat Transfer in Thermoelectric Materials and Devices." *Journal of Heat Transfer* 135(6):61605.
Timalsina, Yukta P., Andrew Horning, Robert F. Spivey, Kim M. Lewis, Tung-Sheng Kuan, Gwo-Ching Wang, and Toh-Ming Lu. 2015. "Effects of Nanoscale Surface Roughness on the Resistivity of Ultrathin Epitaxial Copper Films." *Nanotechnology* 26(7):75704.
Timalsina, Yukta P., Xiaohan Shen, Grant Boruchowitz, Zhengping Fu, Guoguang Qian, Masashi Yamaguchi, Gwo-Ching Wang, Kim M. Lewis, and Toh-Ming Lu. 2013. "Evidence of Enhanced Electron-Phonon Coupling in Ultrathin Epitaxial Copper Films." *Applied Physics Letters* 103(19):191602.
Tong, Zhen, Shouhang Li, Xiulin Ruan, and Hua Bao. 2019. "Comprehensive First-Principles Analysis of Phonon Thermal Conductivity and Electron-Phonon Coupling in Different Metals." *Physical Review B* 100(14):144306.
Tritt, Terry M., ed. 2004. *Thermal Conductivity*. New york: Springer US.
Tsebro, V. I., O. E. Omel'yanovskii, E. F. Kukovitskiĭ, N. A. Sainov, N. A. Kiselev, and D. N. Zakharov. 1998. "Temperature Dependence of Electric Resistance and Magnetoresistance of Pressed Nanocomposites of Multilayer Nanotubes with the Structure of Nested Cones." *Journal of Experimental and Theoretical Physics* 86(6):1216–1219.
Vafaei, Arash, Anming Hu, and Irene A. Goldthorpe. 2014. "Joining of Individual Silver Nanowires via Electrical Current." *Nano-Micro Letters* 6(4):293–300.
Völklein, F., H. Reith, T. W. Cornelius, M. Rauber, and R. Neumann. 2009. "The Experimental Investigation of Thermal Conductivity and the Wiedemann–Franz Law for Single Metallic Nanowires." *Nanotechnology* 20(32):325706.
Volz, Sebastian G., and Gang Chen. 1999. "Molecular Dynamics Simulation of Thermal Conductivity of Silicon Nanowires." *Applied Physics Letters* 75(14):2056–2058.
Wang, Jianfeng, James K. Carson, Mike F. North, and Donald J. Cleland. 2008. "A New Structural Model of Effective Thermal Conductivity for Heterogeneous Materials with Co-Continuous Phases." *International Journal of Heat and Mass Transfer* 51(9–10):2389–2397.
Wang, Jianli, Zhizheng Wu, Chengkun Mao, Yunfeng Zhao, Juekuan Yang, and Yunfei Chen. 2018. "Effect of Electrical Contact Resistance on Measurement of Thermal Conductivity and Wiedemann-Franz Law for Individual Metallic Nanowires." *Scientific Reports* 8(1):4862.
Weathers, Annie, and Li Shi. 2013. "Thermal Transport Measurement Techniques for Nanowires and Nanotubes." *Annual Review of Heat Transfer* 16(1):101–134.
Wei, Bingqing, Ralph Spolenak, Philipp Kohler-Redlich, Manfred Rühle, and Eduard Arzt. 1999. "Electrical Transport in Pure and Boron-Doped Carbon Nanotubes." *Applied Physics Letters*

74(21):3149–3151.
Werheit, Helmut, Udo Kuhlmann, Bernhard Herstell, and Walter Winkelbauer. 2009. “Reliable Measurement of Seebeck Coefficient in Semiconductors.” *Journal of Physics: Conference Series* 176:12037.
Wilson, R. B., and David G. Cahill. 2012. “Experimental Validation of the Interfacial Form of the Wiedemann-Franz Law.” *Physical Review Letters* 108(25):255901.
Wingert, Matthew C., Zack C. Y. Chen, Edward Dechaumphai, Jaeyun Moon, Ji Hun Kim, Jie Xiang, and Renkun Chen. 2011. “Thermal Conductivity of Ge and Ge-Si Core-Shell Nanowires in the Phonon Confinement Regime.” *Nano Letters* 11(12):5507–5513.
Wingert, Matthew C., Zack C. Y. Chen, Shooshin Kwon, Jie Xiang, and Renkun Chen. 2012. “Ultra-Sensitive Thermal Conductance Measurement of One-Dimensional Nanostructures Enhanced by Differential Bridge.” *Review of Scientific Instruments* 83(2):24901.
Wingert, Matthew C., Soonshin Kwon, Ming Hu, Dimos Poulikakos, Jie Xiang, and Renkun Chen. 2015. “Sub-Amorphous Thermal Conductivity in Ultrathin Crystalline Silicon Nanotubes.” *Nano Letters* 15(4):2605–2611.
Xiong, Shiyun, Yuriy a. Kosevich, K. S ääskilahti, Yuxiang Ni, and Sebastian Volz. 2014. “Tunable Thermal Conductivity in Silicon Twinning Superlattice Nanowires.” *Physical Review B* 90(19):195439.
Yanagi, Kazuhiro, Hiroki Udoguchi, Satoshi Sagitani, Yugo Oshima, Taishi Takenobu, Hiromichi Kataura, Takao Ishida, Kazuyuki Matsuda, and Yutaka Maniwa. 2010. “Transport Mechanisms in Metallic and Semiconducting Single-Wall Carbon Nanotube Networks.” *ACS Nano* 4(7):4027–4032.
Yang, Juekuan, Meng Shen, Yang Yang, William J. Evans, Zhiyong Wei, Weiyu Chen, Alfred A. Zinn, Yunfei Chen, Ravi Prasher, Terry T. Xu, Pawel Keblinski, and Deyu Li. 2014. “Phonon Transport through Point Contacts between Graphitic Nanomaterials.” *Physical Review Letters* 112(20):205901.
Yang, Juekuan, Scott Waltermire, Yunfei Chen, Alfred A. Zinn, Terry T. Xu, and Deyu Li. 2010. “Contact Thermal Resistance between Individual Multiwall Carbon Nanotubes.” *Applied Physics Letters* 96(2):23109.
Yang, Juekuan, Yang Yang, Scott W. Waltermire, Timothy Gutu, Alfred A. Zinn, Terry T. Xu, Yunfei Chen, and Deyu Li. 2011. “Measurement of the Intrinsic Thermal Conductivity of a Multiwalled Carbon Nanotube and Its Contact Thermal Resistance with the Substrate.” *Small* 7(16):2334–2340.
Yang, Juekuan, Yang Yang, Scott W. Waltermire, Xiaoxia Wu, Haitao Zhang, Timothy Gutu, Youfei Jiang, Yunfei Chen, Alfred a Zinn, Ravi Prasher, Terry T. Xu, and Deyu Li. 2012. “Enhanced and Switchable Nanoscale Thermal Conduction due to van Der Waals Interfaces.” *Nature Nanotechnology* 7(2):91–95.
Yang, Lin. 2019. “Phonon Transport in Nanowires – Beyond Classical Size Effects.” (Doctoral dissertation, Vanderbilt University).
Yang, Lin, Yi Tao, Jinyu Liu, Chenhan Liu, Qian Zhan, Manira Akter, Yang Zhao, Terry T. Xu, Yaqiong Xu, Zhiqiang Mao, Yunfei Chen, and Deyu Li. 2019. “Distinct Signatures of Electron–Phonon Coupling Observed in the Lattice Thermal Conductivity of NbSe3 Nanowires.” *Nano Letters* 19(1):415–441.
Yang, Lin, Yang Yang, Qian Zhang, Yin Zhang, Youfei Jiang, Zhe Guan, Matthew Gerboth, Juekuan Yang, Yunfei Chen, D. Greg Walker, Terry T. Xu, and Deyu Li. 2016. “Thermal Conductivity of Individual Silicon Nanoribbons.” *Nanoscale* 8(41):17895–17901.

Yang, Lin, Qian Zhang, Zhiguang Cui, Matthew Gerboth, Yang Zhao, Terry T. Xu, D.Greg Walker, and Deyu Li. 2017. “Ballistic Phonon Penetration Depth in Amorphous Silicon Dioxide.” *Nano Letters* 17(12):7218–7225.

Yang, Lin, Qian Zhang, Zhiyong Wei, Zhiguang Cui, Yang Zhao, Terry T. Xu, Juekuan Yang, and Deyu Li. 2019. “Kink as a New Degree of Freedom to Tune the Thermal Conductivity of Si Nanoribbons.” *Journal of Applied Physics* 126(15):155103.

Yang, Lin, Yang Zhao, Qian Zhang, Juekuan Yang, and Deyu Li. 2019. “Thermal Transport through Fishbone Silicon Nanoribbons: Unraveling the Role of Sharvin Resistance.” *Nanoscale* 11(17):8196–8203.

Yang, Nuo, Gang Zhang, and Baowen Li. 2008. “Ultralow Thermal Conductivity of Isotope-Doped Silicon Nanowires.” *Nano Letters* 8(1):276–280.

Yao, Qin, Lidong Chen, Wenqing Zhang, Shengcong Liufu, and Xihong Chen. 2010. “Enhanced Thermoelectric Performance of Single-Walled Carbon Nanotubes/polyaniline Hybrid Nanocomposites.” *ACS Nano* 4(4):2445–2451.

Yoneoka, Shingo, Jaeho Lee, Matthieu Liger, Gary Yama, Takashi Kodama, Marika Gunji, J. Provine, Roger T. Howe, Kenneth E. Goodson, and Thomas W. Kenny. 2012. “Electrical and Thermal Conduction in Atomic Layer Deposition Nanobridges Down to 7 Nm Thickness.” *Nano Letters* 12(2):683–686.

Yosida, Y., and I. Oguro. 1999. “Variable Range Hopping Conduction in Bulk Samples Composed of Single-Walled Carbon Nanotubes.” *Journal of Applied Physics* 86(2):999–1003.

Yosida, Yositaka. 1999. “Electrical Resistance in Sheets Composed of Multiwalled Carbon Nanotubes.” *Journal of Physics and Chemistry of Solids* 60(1):1–4.

Yu, Dingshan, Kunli Goh, Hong Wang, Li Wei, Wenchao Jiang, Qiang Zhang, Liming Dai, and Yuan Chen. 2014. “Scalable Synthesis of Hierarchically Structured Carbon Nanotube–graphene Fibres for Capacitive Energy Storage.” *Nature Nanotechnology* 9(7):555–562.

Yu, Jen Kan, Slobodan Mitrovic, Douglas Tham, Joseph Varghese, and James R. Heath. 2010. “Reduction of Thermal Conductivity in Phononic Nanomesh Structures.” *Nature Nanotechnology* 5(10):718–721.

Yu, Yi, Fan Cui, Jianwei Sun, and Peidong Yang. 2016. “Atomic Structure of Ultrathin Gold Nanowires.” *Nano Letters* 16(5):3078–3084.

Yu, Zhibin, Lu Li, Qingwu Zhang, Weili Hu, and Qibing Pei. 2011. “Silver Nanowire-Polymer Composite Electrodes for Efficient Polymer Solar Cells.” *Advanced Materials* 23(38):4453–4457.

Zhang, Qian. 2017. “Thermal Transport in Individual Nanowires of Fine Structures.” (Doctoral dissertation, Vanderbilt University).

Zhang, Qian, Zhiguang Cui, Zhiyong Wei, Siang Yee Chang, Lin Yang, Yang Zhao, Yang Yang, Zhe Guan, Youfei Jiang, Jason Fowlkes, Juekuan Yang, Dongyan Xu, Yunfei Chen, Terry T. Xu, and Deyu Li. 2017. “Defect Facilitated Phonon Transport through Kinks in Boron Carbide Nanowires.” *Nano Letters* 17(6):3550–3555.

Zhang, Qian, Chenhan Liu, Xue Liu, Jinyu Liu, Zhiguang Cui, Yin Zhang, Lin Yang, Yang Zhao, Terry T. Xu, Yunfei Chen, Jiang Wei, Zhiqiang Mao, and Deyu Li. 2018. “Thermal Transport in Quasi-1D van Der Waals Crystal Ta2Pd3Se8 Nanowires: Size and Length Dependence.” *ACS Nano* 12(3):2634–2642.

Zhang, Wei Wei, Hong Yu, Shuang Ying Lei, and Qing An Huang. 2011. “Modelling of the Elastic Properties of Crystalline Silicon Using Lattice Dynamics.” *Journal of Physics D: Applied Physics* 44(33):335401.

Zhang, Yin, Xin Zhang, Lin Yang, Qian Zhang, Matthew L. Fitzgerald, Akira Ueda, Yunfei Chen, Richard Mu, Deyu Li, and Leon M. Bellan. 2018. “Thermal Transport in Electrospun Vinyl Polymer Nanofibers: Effects of Molecular Weight and Side Groups.” *Soft Matter* 14(47):9534–9541.

Zheng, Jianlin, Matthew C. Wingert, Edward Dechaumphai, and Renkun Chen. 2013. “Sub-Picowatt/kelvin Resistive Thermometry for Probing Nanoscale Thermal Transport.” *Review of Scientific Instruments* 84(11):114901.

Zhou, Yanguang, Xiaoliang Zhang, and Ming Hu. 2017. “Nonmonotonic Diameter Dependence of Thermal Conductivity of Extremely Thin Si Nanowires: Competition between Hydrodynamic Phonon Flow and Boundary Scattering.” *Nano Letters* 17(2):1269–1276.

Ziman, J. M. 2001. *Electrons and Phonons: The Theory of Transport Phenomena in Solid*. Oxford University Press.

Zvyagin, I. P. 1973. “On the Theory of Hopping Transport in Disordered Semiconductors.” *Physica Status Solidi (B)* 58(2):443–449.